TOWARDS LARGE-SCALE SIMULATIONS OF TWO-PHASE FLOWS WITH MOVING CONTACT LINES IN COMPLEX GEOMETRIES

A Dissertation

Presented to the Faculty of the Graduate School

of Cornell University

in Partial Fulfillment of the Requirements for the Degree of

Doctor of Philosophy

by

Sheng Wang

December 2018

TOWARDS LARGE-SCALE SIMULATIONS OF TWO-PHASE FLOWS WITH MOVING CONTACT LINES IN COMPLEX GEOMETRIES

Sheng Wang, Ph.D.

Cornell University 2018

Two-phase flows with moving contact lines are ubiquitous in many natural phenomena and industrial applications such as internal combustion engines, micro-fluidic devices, fuel cells, etc. Accurate modeling of contact line dynamics can provide insights about the underlying physics and aid in optimizing the performance of these engineering devices.

Predictive simulation of these flows is challenging, due to their inherent multi-physics and multi-scale nature. The disparate scales at the contact line prevent fully-resolved simulations due to the enormous computational cost. Moreover, the viscous stress diverges at the contact line while using the no-slip boundary condition, resulting in mesh-dependent simulations of flows dominated by the viscous force.

This dissertation intends to address the above simulation issues and builds a numerical framework to enable large-scale 3D simulations of two-phase flows in complex geometries. In the first part of the work, a numerical approach is developed to simulate two-phase flows with contact lines. This approach combines a conservative level set method to capture the interface, a conservative cut-cell immersed boundary method to handle complex geometry, and the uncompensated Young's force to treat the contact lines. Detailed verifications are performed to confirm this approach to be discretely conservative, accurate, and robust. Second, by writing the weak form of the Navier-Stokes equations for two-phase flows with

moving contact lines, two unclosed terms are identified: a sub-grid scale (SGS) surface tension force and an SGS viscous force. The SGS surface tension force is closed by the uncompensated Young's force model, and a new physics-based closure is derived for the SGS viscous force. Simulations using both SGS models are verified to be mesh-independent and physically accurate across a number of examples, including drop spreading on a horizontal plane and drop sliding down an inclined plane. Finally, the proposed approach is applied in the study of drop-fiber interactions and jet-plane interactions. Several new insights models are extracted from the simulation results for future reduced-order modeling.

BIOGRAPHICAL SKETCH

Born and raised in Nantong, China, Sheng Wang developed an early interest in mathematics and physics during his middle and high school years at Qidong. After high school, he went to Shanghai Jiao Tong University (SJTU) to pursue a bachelor's degree in engineering. He joined the dual-degree program at SJTU and transferred to the University of Michigan (Umich) at Ann Arbor for his junior year. During his course of study at Umich, he developed an interest in fluid mechanics and physics-based simulations under the supervision of Prof. Eric Johnsen. He continued his pursuit of a Ph.D. degree at Cornell after graduating from Umich in 2013. At Cornell, under the guidance of Prof. Olivier Desjardins, his research focused on developing numerical methods for large-scale computations of liquid-gas flows and particle-laden flows in complex geometries.

This document is dedicated to my parents.

ACKNOWLEDGEMENTS

First and foremost, I would like to express my sincere gratitude to my advisor Professor Olivier Desjardins, His support and guidance throughout my stay at Cornell has had a profound influence on my academic and personal development. For example, I became addicted to Gimme Americano after he bought me one for the first time. His patience, enthusiasm and immense knowledge helped me throughout of research. I appreciate the freedom and independence he gave me to pursue my own ideas as well as many valuable suggestions.

I thank Professors Paul Steen and David Bindel, who, in addition to forming my thesis committee, have contributed many useful comments on this dissertation. I appreciated their insightful suggestions for my research, which played a key role in the successful completion of my Ph.D. work.

I would also like to thank Professor Michel Louge for his availability and interest in my work. His curiosity and deep understanding of the fundamental nature of fluid mechanics have led to many useful insights.

I wish to acknowledge former and current members of the Desjardins Research Group. I would like to thank Jesse Capecelatro for his help and encouragement at the beginning of my Ph.D. program. Stephanie Firehammer carefully proofread my first manuscript and hosted many interesting activities. Houssem Kasbaoui, John Palmore, Robert Chiodi, and Ravi Patel have offered me all sorts of invaluable help, insightful discussion of various research topics, and constructive critiques of my practice talks.

Finally, I want to thank my Mom and Dad, who have unconditionally supported me while I have chased my dreams on the other side of the globe. Without their support, I would not have been able to make my way to Cornell.

Funding by the Pall Corporation and the Office of Naval Research is gratefully

acknowledged.

TABLE OF CONTENTS

LIST OF TABLES

LIST OF FIGURES

CHAPTER 1

INTRODUCTION

1.1 Background and motivation

Two-phase flows with moving contact lines play an essential role in nature and human life every day. For example, Namib desert beetles (see Figure 1.1, a) collect drinking water from fog-laden wind on their bumpy backs by alternating hydrophobic and hydrophilic regions [71]; cacti (see Figure 1.1, b) use conical spines to harvest fog in highly arid deserts [43]; and basilisks (see Figure 1.1, c) can run across water, using only their feet as a source of both lift and thrust [40]. Rich contact-line-related physics also affect our daily beverages. For instance, the surface tension gradient, caused by evaporation leads to coffee stains (see Figure 1.2, a) from dried coffee drops [28], and beautiful wine tears (see Figure 1.2, b) are caused by the surface tension gradient and Rayleigh-Taylor instability [91]. Better understanding of the dynamics of flow with contact lines is likely to provide us with better understanding of nature, a better way to wash away coffee stains, and a short-cut towards becoming wine-tasting masters.

Understanding the dynamics of two-phase flows with moving contact lines is highly important in science and engineering. In the energy sector, oil extraction, transportation, conversion, and eventually burning are all closely related to the study of two-phase flow with moving contact lines. Recent studies [105] have shown that changes in wettability can increase the efficiency of oil extraction. Inside an internal combustion engine, liquid-anchoring at the inlet nozzle affects downstream atomization, affecting evaporation rates and burning efficiency. Thus, a detailed understanding of contact-line physics can enable engineers to extract,

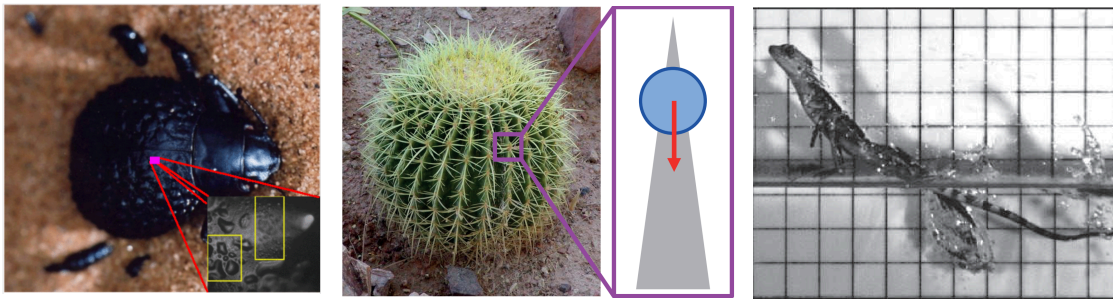

Figure 1.1: a) The backs of a Namib desert beetle. The bumps attract water, while the flat areas repel water. From Parker and Lawrence [71], courtesy of Nature Publishing Group. b) Spines of a cactus. Water drops move toward the thick end spontaneously. From Parker and Lawrence [71], courtesy of Nature Publishing Group. c) A Jesus lizard runs on a water surface. From Hsieh and Lauder [40], courtesy of the National Academy of Science.

transport, convert, and burn oil in a cost-effective manner. Droplet motion in microfluidics [23], fuel evaporation and advection in fuel cells [38], and many other multiphase flow problems are closely related to the dynamics of two-phase flows with moving contact lines.

Figure 1.2: (a) Coffee stain on a table. (b) Wine tears in a glass of ice wine.

Despite their ubiquity and importance, there are few effective predictive tools for application to two-phase flows with moving contact lines. Experimental studies of two-phase flows with moving contact lines are not easy to perform, because the

length and time scales are extremely short for many flows of practical interest. Moreover, surface heterogeneity caused by surface roughness, surfactants, or the electrostatic force are difficult to measure accurately in an experimental framework. These difficulties in experimental studies suggest the use of a numerical approach as an alternative, assisted by increasingly powerful computing resources and improved numerical algorithms. In this dissertation, I aim to develop a numerical framework for 3D large-scale simulations of two-phase flows with moving contact lines in complex geometries, and then demonstrate its predictive capability using two flow scenarios: drop-fiber and jet-plane interactions.

1.2 Previous studies

As this research focuses on two-phase flows with moving contact lines with an emphasis on contact-line modeling, it is appropriate to start with the basic concepts of the static contact angle and the dynamic contact angle. We then review relevant experimental, modeling, and numerical studies.

Static contact angle

A static water drop on a solid surface exhibits all three phases, i.e., the liquid phase, the gas phase, and the solid phase, around the contact line. The angle between the liquid-gas interface and the liquid-solid interface is defined as the static contact angle θ_s, which represents the wettability of the solid surface. Thermodynamically, minimization of Gibbs free energy makes it possible to calculate θ_s, which is a balance of solid-gas surface energy γ_{SG}, solid-liquid surface energy γ_{SL}, and liquid-

gas surface energy σ:

$$\gamma_{\mathrm{SG}} - \gamma_{\mathrm{SL}} - \sigma \cos\theta_s = 0, \tag{1.1}$$

which is known as the Young-Laplace equation. On a hydrophilic surface, θ_s is smaller than 90°; on a hydrophobic surface, θ_s is larger than 90°. Static contact angles can be measured via optical or force-balance methods [102].

Dynamic contact angle

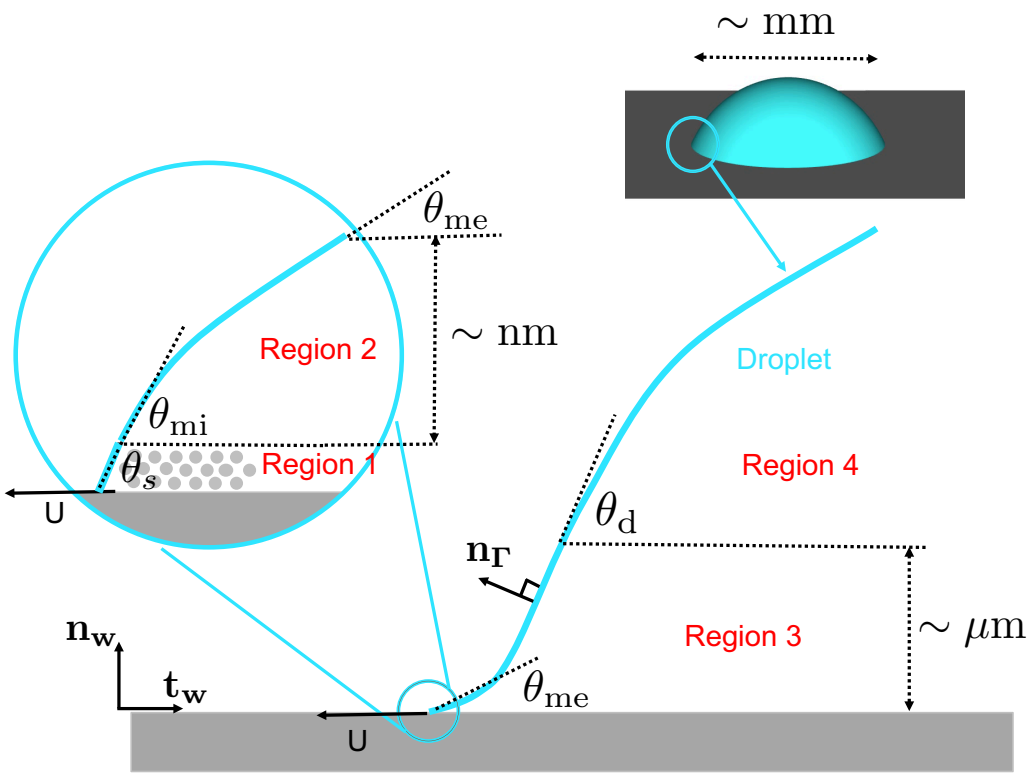

Figure 1.3: Schematic diagram of a partially wetting drop spreading on a flat surface. θ_{mi} is the microscopic contact angle, θ_{me} is the mesoscopic contact angle, and θ_{d} is the macroscopic contact angle or the dynamic contact angle. This figure is adapted from Chen et al. [15].

The situation changes substantially when the contact line starts to move along

the solid interface. This difference is caused by the viscous force and the inertial force, which are absent from the static contact angle problem. Accurate measurement of the viscous force is challenging [97], due to disparate scales, as shown in Figure 1.3. Based on the dominant effective force, we divide the contact line region into four representative regions. In Region 1, the flow is dominated by intermolecular forces [37]. The characteristic length of Region 1 is about $a = 1\,\mathrm{nm}$. The flow in Region 2 is dominated by the Van der Waals force [37]. Because of the Van der Waals force, the surface tension coefficient varies as a function of the distance to the wall, resulting in concave bending of the two-phase interface in this region. The characteristic length of Region 2 is about $a/(2\theta_{\mathrm{mi}}^2)$ and the characteristic height is $a/(2\theta_{\mathrm{mi}})$, where θ_{mi} is defined in Figure 1.3. Region 3 is dominated by the viscous force and the surface tension force, and the corresponding length scale is the viscous length scale $l_\mu = \mu_l^2/(\sigma\rho_l)$, where μ_l is the liquid dynamic viscosity, σ is the surface tension coefficient, and ρ_l is the liquid density. The length scale of this region is affected by the viscosity ratio between the two fluids and the contact angle. Region 4 is dominated by liquid inertia and the gravitational force. The characteristic length is the capillary length, $l_c = \sqrt{\sigma/(\rho_l g)}$. The disparate scales around the contact-line region make the cost of a slip-length resolved simulation prohibitive.

1.2.1 Experimental study

Two-phase flows with moving contact lines have been studied extensively using experimental techniques. Drop spreading [88, 6, 96, 15], drop impact [76, 75], thin film motions [22], and many other capillary driven flows, are closely related to this subject. Here we use drop spreading and drop impact on a solid surface as

examples to review some of the previous experimental studies.

Drop spreading starts immediately after a drop comes into contact with a flat surface. Tanner [88] began a study by measuring the spreading rate of high-viscosity drops, because the corresponding characteristic length-scale (about 1 mm) and time-scale (more than 1 min for a high-viscosity drop) can be resolved even without sophisticated equipment. With the development of high-speed cameras, Bird et al. [6] and Winkels et al. [96] were able to provide accurate measurements of the inertial spreading of water drops, whose characteristic time-scale is about 10 seconds. Precise measurement of such small length scales (about 1 nm) was not possible until the advent of atomic force microscopy (AFM) and surface force apparatuses. The AFM experiment conducted by Chen et al. [15] suggested that the dynamic contact angle at length scales on the order of a nanometer depends on the contact line speed. Studies of drop spreading on porous surfaces [42] and curved surfaces [106], have interesting applications as well.

When a drop impacts a surface, it first spreads over the surface until it reaches its maximum radius [76]. Then, the drop recedes or remains close to this maximum spread, depending on the surface properties. The dynamics are controlled by the balance between inertial, viscous, and capillary forces. When the surface is hydrophobic, the consequence of the drop's retraction can be a partial or complete rebound [75]. Experimental studies of drop impact on both porous surfaces and curved surfaces [106, 54, 47] have begun to emerge, because they are building blocks for many industrial applications.

1.2.2 Modeling study

As described earlier when we defined the dynamic contact angle, a reasonable strategy for contact-line modeling is to combine models for each region, but such an approach would be unprecedented, due partially to the difficulties of characterizing contact-line motion with disparate scales. There are primarily two types of modeling strategies: the Cox-Voinov hydrodynamic model [20, 92] and the molecular-kinetic model [7]. Both of these models aim to relate the dynamic contact angle θ_d to the static contact angle θ_s by taking a single dominant force into account. Here we provide a brief overview of both models.

Hydrodynamic model

The hydrodynamic model attributes the difference between the dynamic contact angle θ_d and the static contact angel θ_s to the enhanced viscous force in the liquid phase. The theory was first developed by Voinov [92], and then extended by Cox [20]:

$$\theta_d^3 = \theta_s^3 + 9\frac{\mu_l u_0}{\sigma} \ln\left(\frac{l_m}{l_s}\right), \tag{1.2}$$

where μ_l is the dynamic viscosity of the liquid phase, u_0 is the contact-line speed, l_m is the macroscopic length, and l_s is the slip length. The Cox-Voinov hydrodynamic model is valid for flow with a capillary number that satisfies $\mathrm{Ca} = \frac{\mu_l u_0}{\sigma} < 0.1$.

Molecular-kinetic model

Instead of using the viscous force in the hydrodynamic model, Yarnold and Mason [100] suggested that the contact-line speed could be determined by reference

to the molecular statistical dynamics near the contact line. Blake and Haynes [7] used this idea to develop a mathematical relationship given by

$$\cos(\theta_d) = \cos(\theta_s) - \frac{2k_B T}{\sigma \lambda^2} \sinh^{-1}\left(\frac{u_0}{2k_w \lambda}\right), \tag{1.3}$$

where k_B is the Boltzmann constant and T is the absolute temperature, k_w is the equilibrium frequency of the random molecular displacements at the contact line, and λ is the average distance between adsorption sites on the substrate on which the random molecular displacements occur. As pointed out by Snoeijer and Andreotti [81], we should treat the MKT as a model for molecular-scale motions rather than as an alternative for the hydrodynamic theory. This statement is further supported by our scaling analysis [93].

1.2.3 Numerical study

Simulating two-phase flows with moving contact lines in complex geometries is a challenging task, because modeling such a process combines several difficult numerical problems—simulating two-phase flows and fluid-solid interactions, imposing contact angles, and modeling dynamic contact angles. Moreover, extending the methods developed for 2D to 3D is a non-trivial numerical exercise. Reviews of the numerical challenges involved in simulating two-phase flows [89], simulating fluid-solid interactions [63], imposing contact angles [85], and modeling dynamic contact angles [85] are available in the literature. Despite the challenges, there have been some noteworthy recent developments in modeling two-phase flows with moving contact lines in complex geometries. These studies, each of which attempts to solve all the problems within a single numerical frameworks, are collected in Table 1.1.

Maglio and Legendre [58] simulated a drop sliding on an inclined solid surface

Numerical problems	Two-phase flows	Fluid-solid interaction	Imposing contact angles	Modeling dynamic contact angles	2D or 3D?
Maglio and Legendre [58]	VOF	None	CSF	Cox-Voinov	3D
Das et al. [24]	VOF	IB	CSF	Cox-Voinov	3D
Lepilliez et al. [51]	DLS	IB	LS extrapolation	None	3D
Solomenko et al. [82]	DLS	None	LS extrapolation	Cox-Voinov	3D
Liu and Ding [53]	DI	IB	Characteristic MCL	Cox-Voinov	2D

Table 1.1: List of numerical works on simulating two-phase flows with moving contact lines in complex geometries.

in 3D. They used the volume-of-fluid (VOF) method to capture the two-phase interface. The modified continuum surface force (CSF) method [9] was employed to impose the contact angle. The Cox-Voinov model was used to model the dynamic contact angle. Their approach was able to accurately predict the onset motion of a drop on an inclined plane as well as the corresponding drop shape. They did not, however, consider drop sliding on a complex shape.

Das et al. [24] proposed a numerical framework that also employed a VOF method for interface capture, the CSF method to impose the contact angle, and the Cox-Voinov model to model the dynamic contact angle. In addition, they built an immersed boundary method to represent walls, enabling them to simulate two-phase flows in more complex structures. Moreover, they demonstrated their ability to simulate a moving sphere interacting with two-phase flows, but the viscous force on the object is likely to be underestimated using the Cox-Voinov model [58].

Lepilliez et al. [51] proposed a numerical framework for simulating two-phase flows in irregular domains with contact lines. In their framework, a distance level-set (DLS) method was used to capture the two-phase interface, an immersed boundary method was used to represent the solid wall, and the static contact angle was imposed in the ghost cell. Their approach was capable of simulating flows with complex boundaries, but no strict convergence with mesh refinement was shown.

No dynamic contact angle modeling was utilized in the study.

Solomenko et al. [82] presented a DLS method for large-scale simulations of 3D flows with moving contact lines. Although rendered in 3D, they considered only a flat plate as the solid phase. As neither the DLS method nor the reinitialization equation was written in conservative form, a significant increase in the interface area led to a loss of mass in their simulations [82].

Liu and Ding [53] use a diffuse-interface method to capture interfaces, while an IB method was used to model the moving solid boundaries. In addition, a characteristic moving-contact-line (MCL) model was developed to simulate moving contact lines on curved boundaries. Careful evaluations of the conservation and convergence properties of the proposed method were presented, but the researchers did not extend the work to 3D.

We note that a systematic evaluation of the conservation, convergence, and accuracy of a numerical framework is necessary for predictive large-scale simulations. Such an evaluation is not a common practice yet in the literature but will be conducted in this dissertation.

1.3 Dissertation outline

In this dissertation, a numerical framework is first presented for large-scale simulations of two-phase flows with moving contact lines in complex geometries, and then demonstrate its predictive capability in problems such as drop-fiber and jet-plane interactions. In Chapter 2, we first present the numerical framework with which we simulate static contact-angle problems. The proposed method is then extended

to simulate moving contact angles with the aid of the sub-grid-scale viscous force in Chapter 3. The proposed method is used in Chapter 4 to study drop-fiber interactions, and in Chapter 5 to study jet-plane interactions . Finally, concluding remarks are given in Chapter 6.

1.4 Achievements

Towards large-scale simulation of two-phase flows with moving contact lines in complex geometries, this dissertation's contributions to numerical methods, contact-line modeling, and large-scale simulation are summarized as follows:

Numerical method

- A conservative, accurate, and robust numerical framework for two-phase flows with moving contact lines in complex geometries has been developed. This framework utilizes a conservative level-set method to capture the liquid-gas interface, a conservative immersed boundary method to represent the solid phase, and the uncompensated Young's force method to impose a contact angle. (Chapter 2, Section 3-5)
- To provide a continuous distance level-set field for curvature calculation, a 3D PDE-based extension method has been developed to extrapolate the distance level-set field into the wall. As a result of this extension method, spurious current, which is caused by numerical errors in the curvature calculation, has been reduced by a factor of 10. (Chapter 2)

Contact line modeling

- We first demonstrate that simulations of two-phase flows with moving contact lines can be accurate and mesh-independent in the inertio-capillary if only a static contact angle model is applied, because the viscous force is negligible in this regime. (Chapter 3, Section 3)
- We also demonstrate that the resolved viscous force is related to mesh size. Therefore the simulations of two-phase flows with moving contact lines are mesh-dependent. (Chapter 3, Section 3)
- To perform simulations of viscous-force-dominated two-phase flows with moving contact lines accurately, a sub-grid-scale (SGS) viscous force model has been developed. (Chapter 3, Section 4)

Large-scale simulation

- The proposed numerical framework has been used to simulate drop-fiber interactions, which includes drop impact on a fiber and drop detachment from a fiber. Reduced-order models, for estimating the critical drop size on a thin fiber under gravity or cross-flow, have been developed based on the simulations results. These models have been further developed to account for the influence of fiber shape and wettability effects. (Chapter 4)
- A numerical study of jet-plane interaction has been performed and has been validated against a microgravity experiment. In addition to the impact Weber number and the Reynolds number, the simulation results also suggest that both gravity and wettability play important roles in predicting flow patterns of jet-plane interaction. (Chapter 5)

CHAPTER 2

MATHEMATICAL DESCRIPTION AND NUMERICAL METHOD

2.1 Introduction

Simulating two-phase flows with moving contact lines is challenging. First, a wide range of length scales is involved. The smallest length in the flow is around the effective slip length (about 1 nanometer), whereas the characteristic length of the two-phase interface is on the order of 1 millimeter. If all the length scales are resolved, a 3D simulation on a uniform mesh requires more than $\left(\frac{1\,\mathrm{mm}}{1\,\mathrm{nm}}\right)^3 = 10^{18}$ computational cells, and therefore is unfeasible considering the limits of current computational resources. Adaptive mesh refinement in the contact line region or sub-grid models of moving contact lines are required in large-scale simulations. Second, the solution of the Navier-Stokes equation with a no-slip boundary condition leads to an infinite viscous force at the contact point [41]. As reported by Afkhami et al. [3], the viscous stress diverges at the contact line with mesh refinement. Third, the spurious velocity caused by the error in curvature calculation deminishes the robustness of the simulation at low capillary numbers.

In this chapter, we use the Conservative Level-Set method to capture the two-phase interface and a conservative immersed boundary method to represent the solid surface. The combination of the CLS method and the conservative immersed boundary method ensures excellent mass conservation. The uncompensated Young's force method is used to indirectly impose the contact angle. Finally, we assess the proposed numerical approach in some benchmark tests.

2.2 Mathematical description

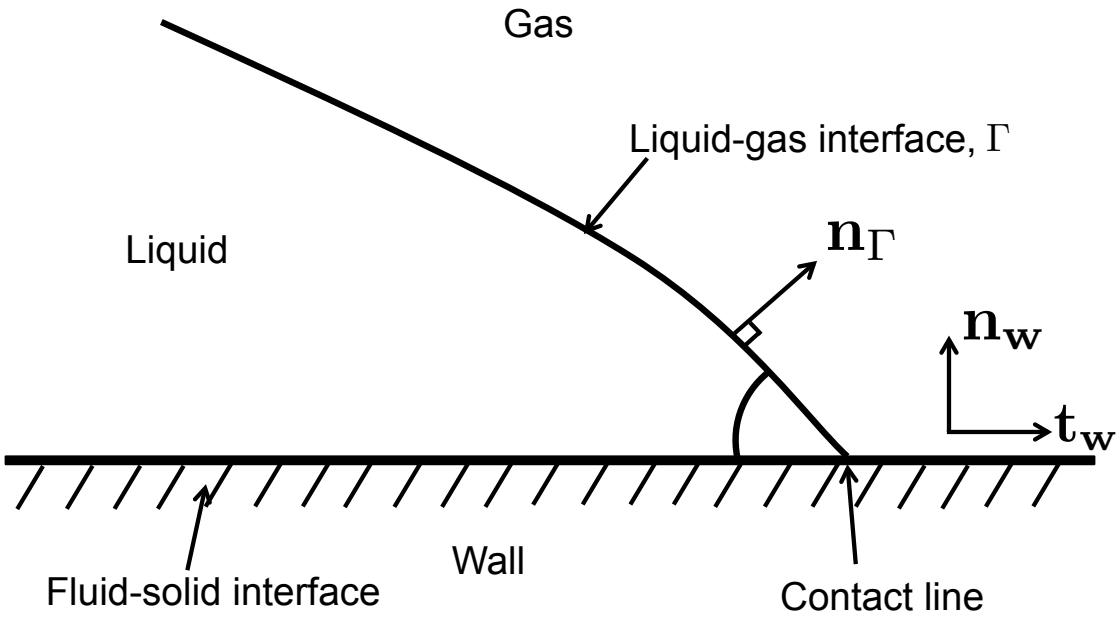

Figure 2.1: Schematic of the triple-phase area near the contact line.

As shown in Figure 2.1, the problem of interest includes three phases, i.e., a liquid phase, a gas phase, and a solid phase, and three interfaces, i.e., a liquid-gas interface, a liquid-solid interface, and a gas-solid interface, all three converging at the contact line. For liquid and gas phases, the governing equations considered are the incompressible Navier-Stokes equations. The solid phase neither move nor deform in the scope of this study, thus there is no need to represent its dynamics. The mathematical description for the fluid and the interfaces is provided below.

2.2.1 Liquid and gas phases - incompressible Navier-Stokes equations

The multiphase flow of interest in this work occurs at low Mach numbers, and therefore we use the incompressible form of the Navier-Stokes equations, which is written as

$$\frac{\partial \rho \mathbf{u}}{\partial t} + \nabla \cdot (\rho \mathbf{u} \otimes \mathbf{u}) = -\nabla p + \nabla \cdot \left(\mu \left[\nabla \mathbf{u} + \nabla \mathbf{u}^{\mathsf{T}} \right] \right) + \rho \mathbf{g}, \tag{2.1}$$

where $\mathbf{u}$ is the velocity field, p is the pressure, ρ is the density, μ is the dynamic viscosity, and $\mathbf{g}$ is the gravitational acceleration. The continuity equation with the incompressible constraint is written as

$$\frac{\partial \rho}{\partial t} + \nabla \cdot (\rho \mathbf{u}) = \frac{\partial \rho}{\partial t} + \mathbf{u} \cdot \nabla \rho = 0. \tag{2.2}$$

Note that the material properties of both phases are taken to be constant, and thus in the liquid phase, $\rho = \rho_l$ and $\mu = \mu_l$, while in the gas phase, $\rho = \rho_g$ and $\mu = \mu_g$.

2.2.2 Liquid-gas interface

There is an interface Γ between the liquid and gas phases, and we use $[\rho]_\Gamma = \rho_l - \rho_g$ and $[\mu]_\Gamma = \mu_l - \mu_g$ to represent the jump in density and viscosity. The velocity field is continuous across the interface, so $[\mathbf{u}]_\Gamma = 0$. The surface tension and the jump in viscous stresses combine to cause a pressure jump across the interface,

$$[p]_\Gamma = \sigma \kappa + 2 [\mu]_\Gamma \, \mathbf{n}_\Gamma^{\mathsf{T}} \cdot \nabla \mathbf{u} \cdot \mathbf{n}_\Gamma, \tag{2.3}$$

where σ is the surface tension coefficient, κ is the interface curvature, and $\mathbf{n}_\Gamma$ is the liquid-gas interface normal.

2.2.3 Fluid-solid interface

At the fluid-solid interface the no-slip and impermeable boundary conditions are applied in this study. Thus, the normal velocity $\mathbf{u}_\perp = (\mathbf{u} \cdot \mathbf{n_w})\,\mathbf{n_w}$ and the tangential velocity $\mathbf{u}_\parallel = \mathbf{u} - \mathbf{u}_\perp$ are zero at the wall.

2.2.4 Contact line

The Young-Laplace equation determines the shape of a liquid-gas interface. The static contact angle (or equilibrium contact angle) θ_s is derived from the solid-gas interfacial energy, σ, the solid-liquid interfacial energy, γ_{SL}, and the liquid-gas interfacial energy, γ_{LG}, by Young's equation,

$$\gamma_\mathrm{SG} - \gamma_\mathrm{SL} - \sigma \cos\theta_\mathrm{s} = 0. \tag{2.4}$$

Instead of solving the Young-Laplace equation to obtain a static contact angle, in this study we directly provide a static contact angle in all the simulations. There is an issue with the boundary condition because the interface moves and thus no-slip is not appropriate. The singularity at the contact line caused by the use of a no-slip boundary condition has been addressed by many previous numerical studies [57, 101, 83, 34]. Similar to [3], the finite-volume approach we use in this study partially alleviates this problem because we solve the weak form of the incompressible Navier-Stokes equations, and never explicitly impose zero tangential velocity at the fluid-solid interface.

The jumps in pressure and thermodynamic quantities at the contact line call for numerical tools capable of handling each of these discontinuities. Therefore, numerical methods need to be developed to treat each of these discontinuities.

2.3 Liquid-gas interface: Conservative Level-Set method

The distance level-set method [18] has been widely used in modeling two-phase flows with contact lines [82, 57, 77]. In this method, a signed distance function is defined as

$$\phi\left(\mathbf{x},t\right)=\pm\left\|\mathbf{x}-\mathbf{x}_{\Gamma}\right\|, \tag{2.5}$$

where $\mathbf{x}_{\Gamma}$ corresponds to the closest point on the interface from $\mathbf{x}$. $\phi(\mathbf{x},t)>0$ is in the liquid phase, and $\phi(\mathbf{x},t)<0$ is in the gas phase. The liquid-gas interface is implicitly defined at iso-surface $\phi\left(\mathbf{x},t\right)=0$.

The interface is transported by solving

$$\frac{\partial\phi}{\partial t}+\mathbf{u}\cdot\nabla\phi=0. \tag{2.6}$$

After transporting, the distance level set is altered, resulting in $|\nabla\phi|\neq 1$. An additional re-initialization step should be performed to restore the smoothness of the distance level-set field. One of the most commonly used re-initialization equation is the Hamilton-Jacobi equation,

$$\frac{\partial\phi}{\partial\tau}+\mathrm{sign}(\phi)\left(|\nabla\phi|-1\right)=0, \tag{2.7}$$

where τ is a pseudo-time. The distance level-set approach leads to mass error in both phases [31, 82], because neither the level-set transport, Eq. 2.6, nor the re-initialization, Eq. 2.7, conserves the volume enclosed by $\phi\left(\mathbf{x},t\right)=0$.

To alleviate the conservation issue, Olsson et al. [68] proposed a conservative level-set approach, later improved by Desjardins et al. [31], for simulating turbulent jet atomization. In this approach, the level-set function is defined as a hyperbolic tangent profile,

$$\psi(\mathbf{x},t) = \frac{1}{2}\left(\tanh\left(\frac{\phi(\mathbf{x},t)}{2\varepsilon}\right)+1\right), \tag{2.8}$$

where ε controls the thickness of the profile, which is set at half of the grid size in this study. $\phi(\mathbf{x},t)$ is the standard signed distance function defined by Eq 2.5. By assuming a solenoidal velocity field, the advection equation becomes

$$\frac{\partial\psi}{\partial t} + \nabla\cdot(\mathbf{u}\psi) = 0. \tag{2.9}$$

As is the case with the distance level-set approach, the hyperbolic tangent profile is distorted after transporting, requiring a re-initialization step. Here we use a strategy introduced by Chiodi and Desjardins [17]:

$$\frac{\partial\psi}{\partial\tau} = \nabla\cdot\left[\frac{1}{4\cosh^2\left(\frac{\phi}{2\varepsilon}\right)}\left(|\nabla\phi\cdot\mathbf{n}_\Gamma|-1\right)\mathbf{n}_\Gamma\right], \tag{2.10}$$

where $\mathbf{n}_\Gamma$ is computed from the signed distance function ϕ using

$$\mathbf{n}_\Gamma = \frac{\nabla\phi}{|\nabla\phi|}. \tag{2.11}$$

Compared with the re-initialization strategy in Olsson et al. [68], this approach avoids calculating the gradient of a stiff function, i.e. $\nabla\psi$. In this approach, the conservative level-set field ψ first maps back to the smoother distance level-set field ϕ, by

$$\phi = \epsilon\ln\left(\frac{\psi}{1-\psi}\right), \tag{2.12}$$

then calculats the gradient. We refer for the details of the implementation of the re-initialization strategy to Chiodi and Desjardins [17]. Since both the transport equation, Eq 2.9, and the re-initialization equation, Eq 2.10, are written in conservative form, the conservative level-set ψ is conserved, the evidence for which will be provided in Section 2.7.

2.4 Fluid-solid interface: Immersed Boundary method

An immersed boundary method based on the cut-cell approach of Meyer et al. [62] is used in this work. This method guarantees discrete conservation of mass and momentum, and provides a sharp representation of the solid boundary.

Considering a general conservative transport equation for a quantity ω, we consider the following transport equation,

$$\frac{\partial \omega}{\partial t} + \nabla \cdot \mathbf{F}(\omega) = 0, \tag{2.13}$$

where $\mathbf{F}(\omega)$ is the flux of ω. By using second-order finite volume discretization, Eq. 2.13 can be written as

$$\omega_c^{n+1} = \omega_c^n - \frac{\Delta t}{V} \sum_{f=1}^{N_f} \left(A_f \mathbf{F}_f^{n+1/2} \cdot \mathbf{n}_f \right) \tag{2.14}$$

where ω_c^n is the cell-mean value of ω at time t^n; Δt is the size of the time step, V is the cell volume, N_f is the number of cell faces, A_f is the area of the cell face, $\mathbf{F}_f$ is the face-mean flux, and $\mathbf{n}_f$ is the outward normal to the cell face.

For computational cells cut by the immersed boundary, Eq. 2.14 becomes

$$\omega_c^{n+1} = \omega_c^n - \frac{\Delta t}{\alpha_w^v V} \left(\sum_{f=1}^{N_f} \left(A_f \mathbf{F}_f^{n+1/2} \cdot \mathbf{n}_f \right) + A_{IB} \mathbf{F}_{IB}^{n+1/2} \cdot \mathbf{n_W} \right), \tag{2.15}$$

where $\alpha_w^v = V_w/V$ is the cell wetted volume V_w divided by the cell volume V, $\alpha_w^s = A_w/A_f$ is the cell face wetted area A_w divided by the cell face area A_f, A_{IB} is the area of immersed boundary, $\mathbf{n_W}$ is the outward normal to the immersed boundary, and $\mathbf{F}_{IB}$ is the mean flux of ω through the immersed boundary surface.

To obtain the wetted volume V_w, the wetted area A_w, and the area of the immersed boundary A_{IB}, the location of the immersed boundary, $\mathbf{x}_{IB}$ is required,

which is specified implicitly through the use of the signed distance level-set

$$B(\mathbf{x}) = \pm \left\| \mathbf{x} - \mathbf{x}_{IB} \right\| . \tag{2.16}$$

Further details on this immersed boundary method can be found in Desjardins et al. [30].

2.5 Contact angle

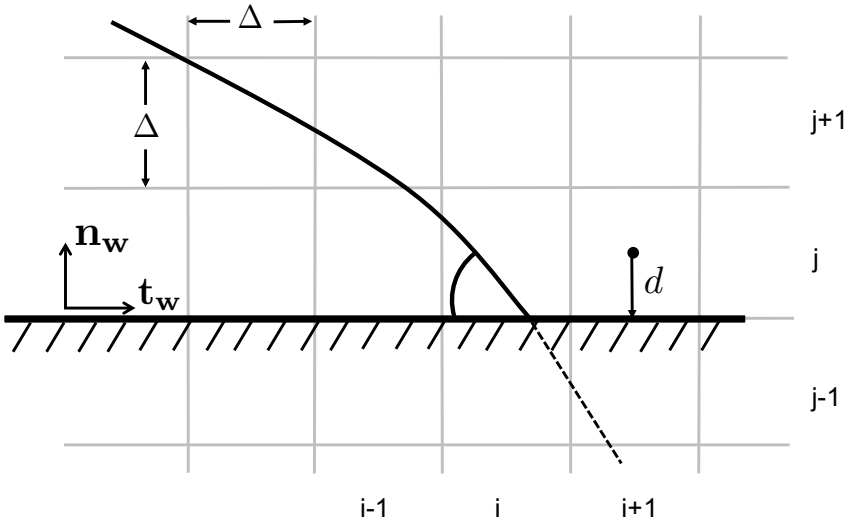

Figure 2.2: Numerical grid around the contact point.

Dynamic contact angle models are often built on the equilibrium contact angle, and therefore we first describe our strategy for imposing the equilibrium contact angle, which we then extend to dynamic contact angle models. We categorize the numerical methods to impose the equilibrium contact angle into two groups. In the first group, the level-set field is modified to inform the curvature calculation.

Both the accuracy of the modification method and the accuracy of the curvature calculation have an impact on the overall accuracy of the numerical approach. Explicitly,

- In [2], the contact angle is directly imposed in cells with contact lines, as

$$\frac{\partial \phi}{\partial \tau} + \mathbf{n}_{\mathrm{w}} \cdot \nabla \phi = \cos(\theta_{\mathrm{e}}), \text{ for } 0 < d < \Delta, \tag{2.17}$$

  where Δ is the local mesh size. In this approach, the equilibrium contact angle is actually imposed at the center of the cell above the wall, i.e., cell (i, j) in Figure 2.2. This approach will be referred to as Method One.

- In [82, 51], the distance level set is first extrapolated into the wall, such as

$$\frac{\partial \phi}{\partial \tau} + \mathbf{n}_{\mathrm{w}} \cdot \nabla \phi = \cos(\theta_{\mathrm{e}}), \text{ for } d < 0; \tag{2.18}$$

  the extrapolated distance field is then employed for curvature calculation. In this approach, the equilibrium contact angle is actually imposed at the center of the cell below the wall, i.e., cell (i, j-1) in Figure 2.2. This approach is named as Method Two for reference.

Note that the curvature of the liquid-gas interface around the contact point is non-zero, as a result of which the calculated contact angle at the contact point differs from the imposed equilibrium contact angle. In the second group, the curvature (or surface tension force) in the contact line cell is directly modified, which is called the surface tension force method.

- In [94, 57], the curvature in the cells with contact lines is directly modified to account for the contact angle, as

$$\kappa = \kappa_{\mathrm{res}} + \frac{\mathbf{n}_{\mathbf{\Gamma}} \cdot \mathbf{n}_{\mathbf{w}} - \cos(\theta_{\mathrm{e}})}{d}, \tag{2.19}$$

where $\mathbf{n_\Gamma}$ is the normal of the liquid-gas interface, and κ_{res} is the curvature of the resolved liquid-gas interface, which written as

$$\kappa_{\text{res}} = \nabla \cdot \mathbf{n}_\Gamma. \tag{2.20}$$

The contact angle at the wall is considered to be the equilibrium contact angle, and no error from modifying the level-set field is introduced in this approach. The surface tension force method is verified to be more accurate than the second modification method in 2.9. Thus the surface tension force method is applied in this study.

Accurate evaluation of the liquid-gas interface normal, Eq 2.11, and the resolved curvature, Eq 2.20, require the distance field inside the wall. Therefore, we introduce a 3D PDE-based extrapolation method, a weighted least-square method for curvature calculation, and the uncompensated Young's force method to implicitly impose the contact angle. Details are listed below.

2.5.1 PDE-based extrapolation

We use the multidimensional extrapolation method proposed by Aslam [4] to extend the distance field into the wall. This is realized by solving the Hamilton-Jacobi equation in the extrapolated region twice. We first extrapolate the dot-product of the liquid-gas interface normal and the wall normal, $\phi_1 = \mathbf{n}_{\text{w}} \cdot \mathbf{n}_\Gamma$, by solving

$$\frac{\partial \phi_1}{\partial \tau} + H_1(d) \nabla \phi_1 \cdot \mathbf{n}_{\text{w}} = 0, \tag{2.21}$$

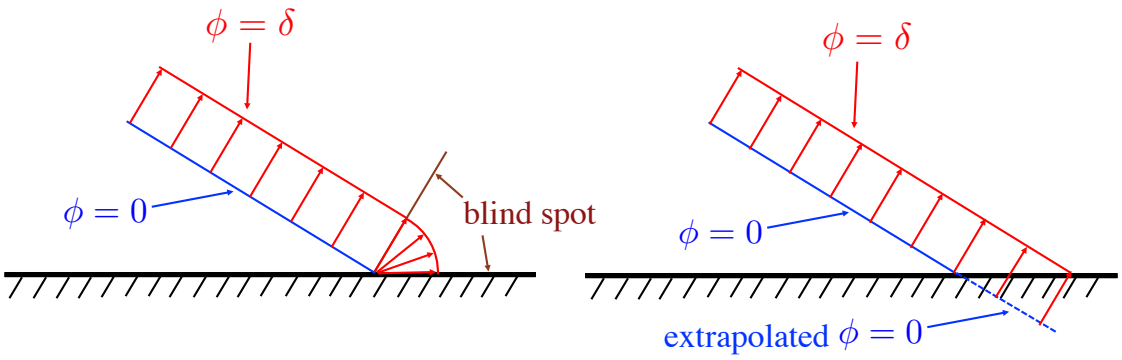

Figure 2.3: Distance level set around the contact point. The right figure shows the blind spot around the contact point. The left figure shows our solution.

where τ is a pseudo-time, and $H_1(d)$ is a Heaviside function, defined as

$$H_1(d) = \begin{cases} 1, & \text{if } d < \Delta \\ 0, & \text{else.} \end{cases} \tag{2.22}$$

The distance field is then extrapolated using ϕ_1 as a source term:

$$\frac{\partial \phi}{\partial \tau} + H_2(d) \nabla \phi \cdot \mathbf{n}_{\text{w}} = \phi_1, \tag{2.23}$$

where $H_2(d)$ is defined as

$$H_2(d) = \begin{cases} 1, & \text{if } d < 0 \\ 0, & \text{else.} \end{cases} \tag{2.24}$$

The spatial discretization is a second-order upwind finite difference. The temporal integration is a second-order Runge-Kutta method [61]. Note that the two-step extrapolation provides a distance field in the wall, but does not remove the blind spot in the right figure in Figure 2.3. Based on the prescribed zero level set $\phi = 0$, we create a level set, $\phi = \delta$. Without the extrapolated $\phi = 0$, $\phi = \delta$ is

bent between the normal of $\phi = 0$ and the wall. The region between the normal of the contact point and the wall is the blind spot [98, 77]. The technique we use to remove the blind spot has two steps:

1. Extrapolate the distance field into the wall by solving Eq 2.21, and Eq 2.23.
2. Reconstruct the distance field by solving a static Eikonal equation for the combined distance field, $\phi_c = \phi \cup \phi_e$:

$$|\nabla \phi_c| = 1, \tag{2.25}$$

   where ϕ is the distance field outside the wall, and ϕ_e is the extrapolated distance field.

The second step is crucial to eliminating the blind spot. In the implementation, we use a fast marching method (FMM) [90] to solve Eq 2.25. Note that all the distance field discussed in the following section is the combined distance field after reconstruction, so we use ϕ instead.

2.5.2 Curvature calculation

For curvature calculation, we build a localized 3D paraboloid to approximate the 3D iso-surface. This idea is realized by the least squares approach introduced by Marchandise et al. [60]. Briefly, a quadratic approximation of the distance field $\phi(\mathbf{x}_i)$ is written as

$$\phi(\mathbf{x}_i + \delta\mathbf{x}) = \phi(\mathbf{x}_i) + d\mathbf{x}^{\mathrm{T}} \nabla \phi_+ \frac{1}{2} d\mathbf{x}^{\mathrm{T}} \mathrm{H} d\mathbf{x}, \tag{2.26}$$

where $\delta\mathbf{x} = (\delta x\mathbf{i}, \delta y\mathbf{j}, \delta z\mathbf{k})$ is the distance to point $\mathbf{x}$ in 3D, and H is the Hessian matrix, calculated as $\mathbf{H} = \nabla\nabla\phi$. Using N cells around $\mathbf{x}_i$, we write Eq 2.26 in the matrix form, as

$$\underbrace{\begin{pmatrix} \phi\left(\mathbf{x}_i + \delta\mathbf{x}_1\right) \\ \vdots \\ \phi\left(\mathbf{x}_i + \delta\mathbf{x}_N\right) \end{pmatrix}}_{\mathbf{b}} = \underbrace{\begin{pmatrix} 1 & \delta x_1 & \delta y_1 & \delta z_1 & \frac{1}{2}\delta x_1^2 & \frac{1}{2}\delta y_1^2 & \frac{1}{2}\delta z_1^2 & \delta x_1\delta y_1 & \delta x_1\delta z_1 & \delta y_1\delta z_1 \\ \vdots & \vdots & \vdots & \vdots & \vdots & \vdots & \vdots & \vdots & \vdots & \vdots \\ 1 & \delta x_N & \delta y_N & \delta z_N & \frac{1}{2}\delta x_N^2 & \frac{1}{2}\delta y_N^2 & \frac{1}{2}\delta z_N^2 & \delta x_N\delta y_N & \delta x_N\delta z_N & \delta y_N\delta z_N \end{pmatrix}}_{\mathbf{A}} \underbrace{\begin{pmatrix} \phi(\mathbf{x}_i) \\ \partial_x\phi(\mathbf{x}_i) \\ \partial_y\phi(\mathbf{x}_i) \\ \partial_z\phi(\mathbf{x}_i) \\ \partial_{xx}\phi(\mathbf{x}_i) \\ \partial_{yy}\phi(\mathbf{x}_i) \\ \partial_{zz}\phi(\mathbf{x}_i) \\ \partial_{xy}\phi(\mathbf{x}_i) \\ \partial_{xz}\phi(\mathbf{x}_i) \\ \partial_{yz}\phi(\mathbf{x}_i) \end{pmatrix}}_{\mathbf{y}}, \tag{2.27}$$

where $\mathbf{y}$ is the unknown, $\mathbf{A}$ and $\mathbf{b}$ are built using the distance and grid information. In the implementation, one extra step is taken to concentrate the error around the calculated cell, by solving the the weighted equation,

$$\mathbf{wAy} = \mathbf{wb}. \tag{2.28}$$

where $\mathbf{w} = \text{diag}(w_{11}, w_{22}, ..., w_{NN})$, and $w_{ii} = \exp(-\frac{\|\delta\mathbf{x}_i\|_2}{1.5h})$ for $i = 1...N$. The over-determined system of linear equations can then be solved in a least squares sense, that is

$$(\mathbf{wA})^{\mathrm{T}}\mathbf{wAy} = (\mathbf{wA})^{\mathrm{T}}\mathbf{wb}. \tag{2.29}$$

The corresponding curvature is computed as

$$\kappa(\mathbf{x}_i) = \frac{\text{tr}(\mathbf{H}) - \mathbf{n}\cdot\mathbf{H}\cdot\mathbf{n}}{|\nabla\phi|}, \tag{2.30}$$

where $\mathbf{n} = (\partial_x\phi\mathbf{i}, \partial_y\phi\mathbf{j}, \partial_z\phi\mathbf{k})$ at $\mathbf{x}_i$. The weighted least square method delivers second-order converging curvatures [17] and works on complex 3D interfaces.

2.5.3 Uncompensated Young's force

Because of the disparate scale separation of the flow around the contact point, direct numerical simulation of contact line motion is computationally expensive. To alleviate this problem, we provide a sub-grid surface tension force model to implicitly impose the contact angle. The surface tension force in the contact cell is expressed as

$$F = F_{\text{res}} + F_{\text{SGS}} = \sigma(\kappa_{\text{res}} + \kappa_{\text{SGS}}), \tag{2.31}$$

where κ_{res} is the curvature of the resolved liquid-gas interface, and κ_{SGS} is the sub-grid scale curvature correction, written as

$$\kappa_{\text{SGS}} = \frac{\mathbf{n_\Gamma} \cdot \mathbf{n_w} - \cos(\theta_e)}{d} f(d), \tag{2.32}$$

where $f(d)$ is a numerical delta function implemented as

$$f(d) = \begin{cases} 1 & \text{if } d < \Delta \\ 0 & \text{else} \end{cases} \tag{2.33}$$

Here we define $\cos(\theta) = \mathbf{n_\Gamma} \cdot \mathbf{n_w}$, enabling us to view the model can be viewed as a kinetic correction to bring θ to θ_e. The force caused by the mismatch between the actual contact angle an the equilibrium contact angle is called the uncompensated Young's Force [27]. Thus we refer to this method as the uncompensated Young's force method.

Note that the sub-grid curvature correction is conceptually the same as the wall adhesion boundary method in the Continuum Surface Force [58, 9] framework.

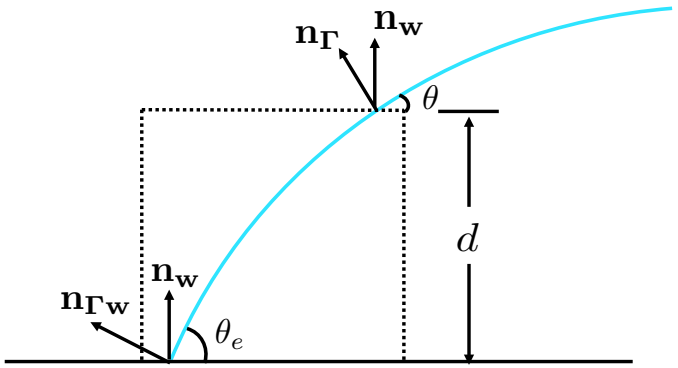

Figure 2.4: Control volume around a contact point.

We provide the derivation here. Consider the magnitude of the averaged surface tension force in the control volume shown in Figure 2.4:

$$\bar{F} = \frac{1}{V}\iiint \sigma \nabla \cdot \mathbf{n_\Gamma} dV = \frac{1}{V}\iiint \sigma \kappa dV. \tag{2.34}$$

The surface tension coefficient σ and the curvature κ are usually considered constant, and we get $\bar{F} = \sigma\kappa$. Then we use the divergence theorem,

$$\bar{F} = \frac{1}{V}\iiint \sigma \nabla \cdot \mathbf{n_\Gamma} dV = \frac{\sigma d}{d^2}\left(\mathbf{n_\Gamma}\cdot\mathbf{n_w} - \mathbf{n_{\Gamma w}}\cdot\mathbf{n_w}\right) = \frac{\sigma}{d}\left(\mathbf{n_\Gamma}\cdot\mathbf{n_w} - \mathbf{n_{\Gamma w}}\cdot\mathbf{n_w}\right) \tag{2.35}$$

where V is the volume, which is d^2 in 2D. The length of the intersection side width is d. $\mathbf{n}$ is the surface normal, which is $\mathbf{n_w}$ on the upper side, and is $-\mathbf{n_w}$ on the lower side. $\mathbf{n_{\Gamma w}}$ is the interface orientation at the contact point, and it is related to the equilibrium contact angle $\cos(\theta_e) = \mathbf{n_{\Gamma w}}\cdot\mathbf{n_w}$. Therefore, the sub-grid curvature correction is the same as the wall adhesion boundary method.

2.6 Solution procedure

With the graphical aid of Figure 2.5, here we summarize the solution procedure:

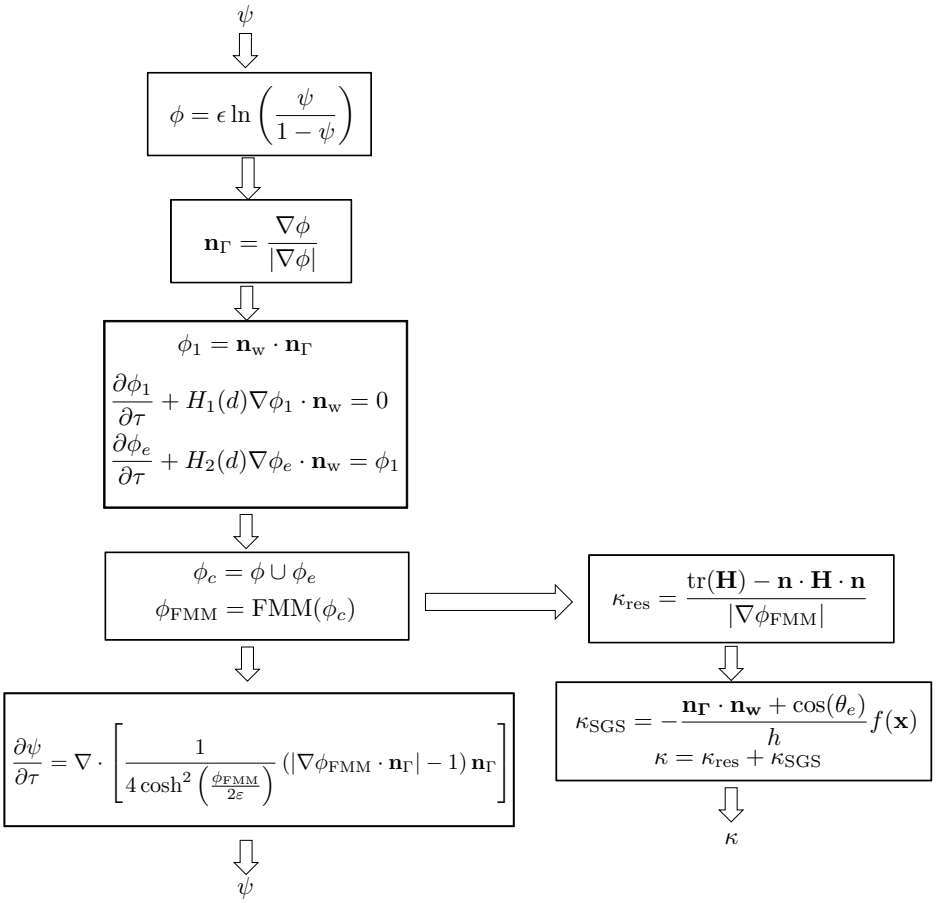

Figure 2.5: Flow chart of the solution procedure.

1. Map the conservative level-set field ψ to the distance level-set field ϕ using Eq 2.12.

2. Use a second-order finite difference method to estimate the normal of the liquid-gas interface $\mathbf{n}_\Gamma$ by calculating Eq 2.11.

3. Evaluate the extended quantity ϕ_1, $\phi_1 = \mathbf{n}_\mathrm{w} \cdot \mathbf{n}_\Gamma$. Perform the first extrapolation, Eq 2.21, then the second extrapolation, Eq 2.23.

4. Reconstruct the combined distance field using an FMM to solve the static Eikonal equation, Eq 2.25.

5. Calculate the resolved curvature using Eq 2.29 and Eq 2.30.
6. Add back the sub-grid surface tension force using the uncompensated Young's force, Eq 2.31.
7. Update ψ using the reinitialization equation Eq 2.10.

The mathematical description presented above is implemented in the framework of the NGA code [29]. The Navier-Stokes equations are solved on a staggered grid with second-order spatial accuracy for both convective and viscous terms, and by the semi-implicit Crank-Nicolson scheme with second-order accuracy for time advancement. The discontinuous density and the surface tension force is treated by the Ghost Fluid Method [36], and the Continuum Surface Force method [9] is used in response to the jump in the viscous stresses within a semi-implicit formulation.

2.7 Verification

2.7.1 Stability: spurious current

Considering a static spherical drop, if the calculated curvature does not remain constant over the whole drop, the resulting gradient in curvature would serve as a source of spurious currents through the surface tension force. A spurious current deminishes the robustness of simulations, especially for simulations with low capillary numbers. In this section, we present our approach to measuring spurious currents, and then show that a spurious current is convergent and weakened after removing the blind spot.

For simulations with unit density and viscosity ratios [72], the intensity of the

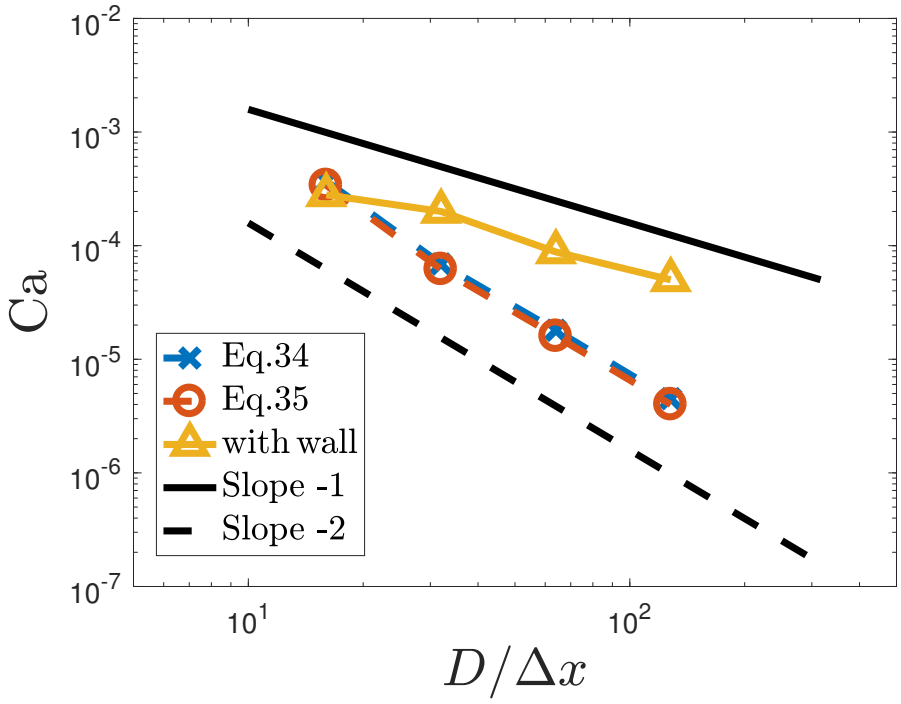

Figure 2.6: Convergence study of the steady state Ca for a 1 mm water drop in air: calculating Ca using Eq 2.36 ($-\times$); calculating Ca using Eq 2.37 ($-\circ$); drop on wall with the blind spot($-\Diamond$); drop on wall without the blind spot($-\triangle$); first order ($-$); second order ($--$).

spurious current is conventionally quantified by

$$\mathrm{Ca} = \frac{\mu_g |v_{\max}|}{\sigma}, \tag{2.36}$$

where μ_g is the dynamic viscosity of the gas phase, $v_{\max}$ is the maximum velocity in the domain, and σ is the surface tension coefficient. It is unclear, however, whether Eq 2.36 is still valid or not with large density and viscosity ratios. Thus, we propose

$$\mathrm{Ca} = \frac{|\mu v|_{max}}{\sigma}, \tag{2.37}$$

which is the maximum capillary number in the domain. Comparing Eq 2.36 and Eq 2.37, we first conduct a test case using a water drop in 3D without a wall. The

physical parameters are collected here: the liquid density $\rho_L = 1000\,\mathrm{kg/m^3}$, the liquid viscosity $\mu_L = 0.001\,\mathrm{Pa \cdot s}$, the gas density $\rho_g = 1\,\mathrm{kg/m^3}$, the gas viscosity $\mu_g = 1 \times 10^{-5}\,\mathrm{Pa \cdot s}$, the surface tension coefficient $\sigma = 0.072\,\mathrm{Nm^{-1}}$, and the drop diameter $D = 1\,\mathrm{mm}$. The corresponding density ratio is 1000, the viscosity ratio is 1000, and the Laplace number is $\mathrm{La} = \sigma\rho_l D/\mu_l^2 = 72000$. A study was performed using drop-size to cell-size ratios $D/\Delta = 8$, 16, 24, and 48. As shown in Figure 2.6, Eq 2.36 systematically over-predicts the spurious current intensity, although the difference is very small. The convergence rate is second order for a single water drop. In the following section, Eq 2.37 is used to quantify the spurious current.

We then conducted a test of spurious currents with the same size drop on a wall. The results for $\theta_e = 60^\circ$ are reported here. Before removing the blind spot, the spurious current does not converge. After removing the blind spot, the spurious current has a first-order convergence rate. The capillary number is at the order of 10^{-4} even on the coarsest tested mesh. The drop in the convergence rate is caused by the fast marching reconstruction of the distance field, i.e., step 4 in the solution procedure, because the distance field after the fast marching reconstruction has less than second-order accuracy, as reported in Chiodi and Desjardins [17].

2.7.2 Accuracy: equilibrium shape of a 2D drop on a plane

We test the accuracy of our numerical approach by testing a 2D drop on a plane without gravity. The equilibrium shape of the drop is controlled by the equilibrium contact angle. The shape can be obtained due to geometrical considerations and mass conservation. As shown in the sketch, the drop radius R, the spreading length L, and the height of the cap, e, are written as functions of the initial radius of the

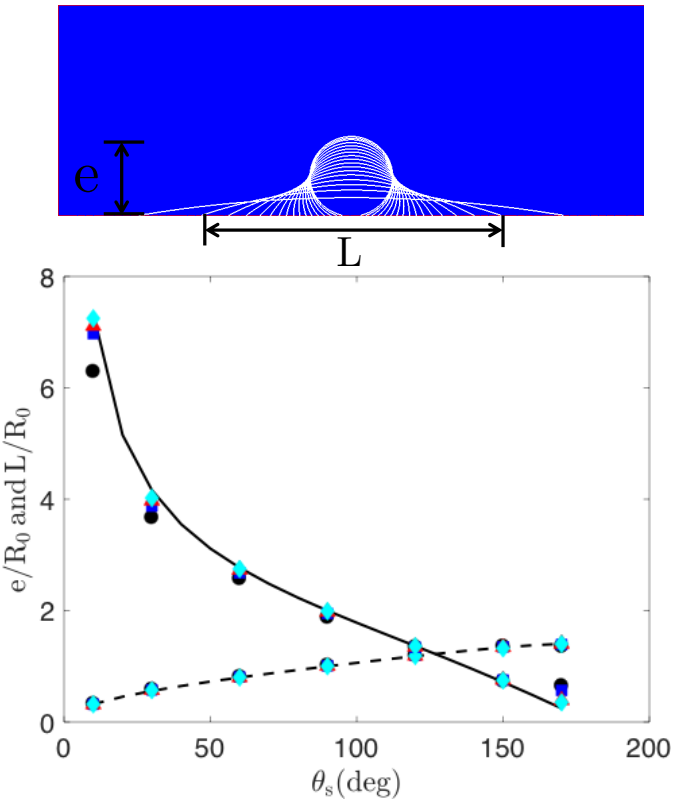

Figure 2.7: Normalized height, e/R_0, and spreading length, L/R_0 of the equilibrium drop versus the contact angle θ_e. Analytical normalized height is shown with a dash line $(--)$, and analytical normalized spreading length is shown with a solid line $(-)$. Computed normalized height and spreading length with mesh refinement, $R_0/\Delta = 6$, 12, 24 and 48, are shown with circles $(\bigcirc)$, square $(\square)$, triangle $(\triangle)$, and diamond $(\Diamond)$ respectively.

circle R_0 and the equilibrium contact angle θ_e:

$$R = R_0\sqrt{\frac{\pi}{2\left(\theta_e - \sin\theta_e\cos\theta_e\right)}},\ L = 2R\sin\theta_e,\ e = R\left(1-\cos\theta_e\right).$$

In the simulation, the drop is initialized as a semicircular drop at a 90° contact angle on the plane. The physical parameters in the simulations are collected in Table 4.5. The surface tension coefficient is deliberately small to decrease drop oscillation around the equilibrium. Simulations are performed using Cartesian coordinates on a regular domain. The plane is built using the immersed boundary,

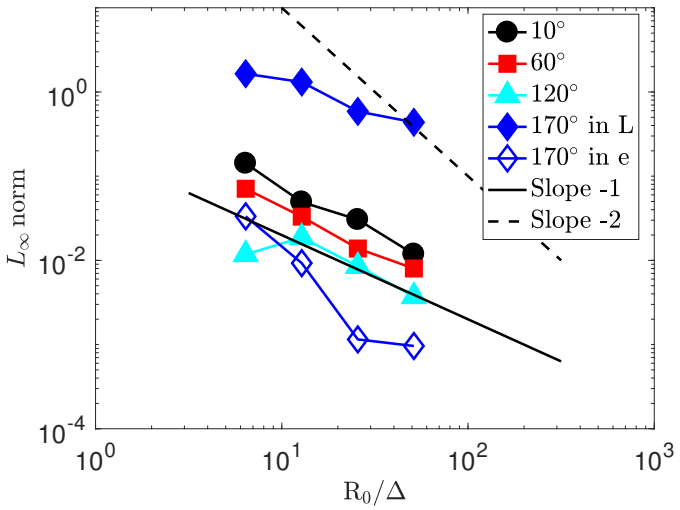

Figure 2.8: L_∞ norm of error in the spreading length or height versus the cell number in radius: error in the spreading length for 10° (−•), 60° (−■), 120° (−▲). 170°(−♦); error in the height for 170°(−◊); first order (−); second order (−−).

intentionally mis-aligned with the numerical mesh. Four drop-radius to cell-size ratios, $R_0/\Delta = 6, 12, 24, 48$, are simulated. The imposed contact angles vary from 10° to 170°. Until equilibrium, the height and spreading length of the drop are collected to be compared with the analytical solutions, as shown in Eq 2.38. We are not comparing the static contact angle at the contact point, because the angle measured at the cell center adjacent to the wall is not the same as the static contact angle at the contact line.

The height e and the spreading length L of the drop are normalized by the drop initial radius R_0. As shown in Figure 2.7, the results of numerical simulations (in symbols) are plotted with the simulated analytical height and spreading length (shown by a dashed line and a solid line, respectively). The simulated results exhibit good agreement with the analytical results. In our previous study [94], the spreading length for 10° converges towards a value that is about 10% below the analytical result. Here, the simulated spreading length converges towards the

analytical result, showing improved accuracy. We perform further comparisons by measuring the infinity norm of error in the spreading length,

$$L_\infty = \max \left| \frac{L_n - L_a}{L_a} \right|, \tag{2.38}$$

where L_n is the numerical spreading length, and L_a is the analytical spreading length. The results are collected in Figure 2.8. The error norm is larger in $\theta_s = 170^\circ$ for the spreading length, because the analytical spreading length is the denominator and is small at that contact angle. Therefore, a better measure of $\theta_s = 170^\circ$ is the height of the drop, also shown in Figure 2.8. For all four cases, the errors in the simulated spreading length decrease with mesh refinement, and the convergence rate is found to fall between the first and second orders.

2.7.3 Conservation: drop impact on a sphere in 3D

Many interesting phenomena arise in the study of a drop impacting a substrate [99], such as splashing, spreading, receding, bouncing, etc. Here, we simulate a 3D drop impact on a sphere at various contact angles, focusing on the dynamic response of the drops to a curved surface at varying static contact angles and the mass conservation property in a non-trivial geometry.

We start with a static test case, the convergence study of a drop on a sphere in 3D, and then investigate drop impact on a sphere in 3D. The physical parameters used in the numerical test are listed in Table 2.1. Note that the initial velocity is zero in the static case, and the drop has an initial velocity u_0 in the dynamic case.

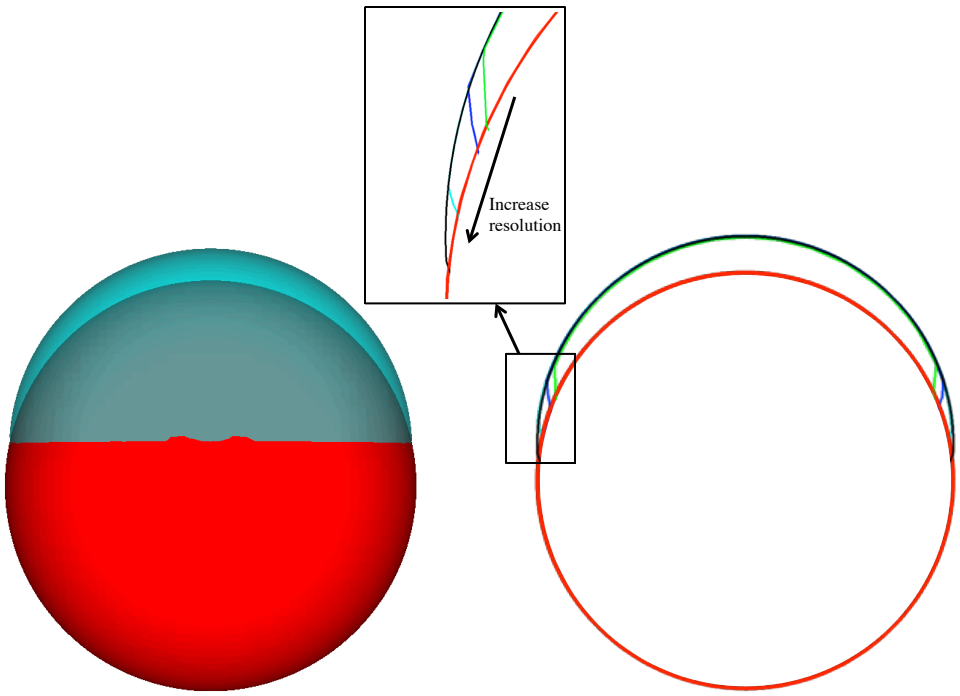

Figure 2.9: Comparison of droplet shapes at equilibrium against the analytical results for $\theta_s = 10°$. The droplet shape at equilibrium in 3D is on the right, the 2D droplet shapes at the cut plane is on the left. Three levels of resolution are plotted, $d_d/\Delta = 12.8$ is in green, $d_d/\Delta = 25.6$ is in dark blue,and $d_d/\Delta = 51.2$ is in light blue. The thick solid black line represents the analytical shape.

In the visualization, the liquid phase is colored in blue, and the solid phase is in red. In Figure 2.9, the left snapshot is a 3D drop on a sphere at equilibrium with $\theta_s = 10°$. We create a 2D plane by cutting though the solid sphere center and the centroid of the liquid phase. The drop shapes at equilibrium are shown on this plane against the analytical result. The sphere diameter to cell-size ratios are $d_d/\Delta = 12.8$, 25.6 and 51.2. As shown in the figure, the numerical shapes approach the analytical shape with mesh refinement.

We then simulate a 3D drop impact on a sphere. Initially, the drop has diameter

Diameter ratio	d_d/d_s	1
Density ratio	ρ_l/ρ_g	1000
Viscosity ratio	ρ_l/ρ_g	100
Reynolds number	$\rho_l u_0 d_d/\mu_l$	50
Weber number	$\rho_l u_0^2 d_d/\sigma$	2.5

Table 2.1: Parameters for drop on a sphere of diameter d_s in 3D.

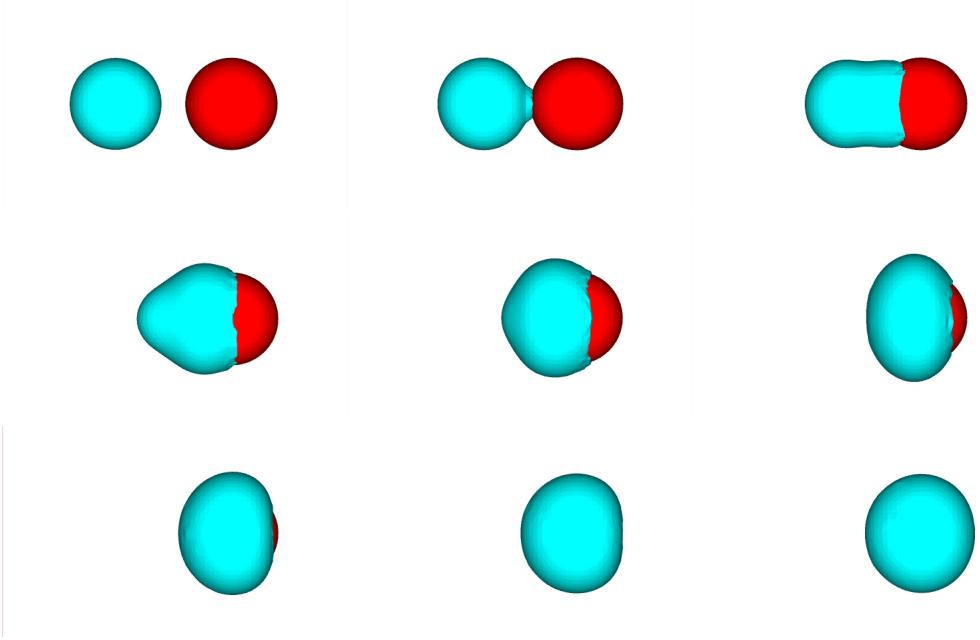

Figure 2.10: A drop impact on a hydrophilic sphere in 3D, $\theta_s = 10°$. The interval between two successive pictures is $\Delta t u_0/d_s = 0.25$ (from left to right and from top to bottom).

d_d and velocity u_0. There are 20 cells across the diameter of the sphere. Figure 2.10 shows snapshots of impact dynamics on a super-hydrophilic sphere ($\theta_s = 10°$). The sphere is fully wetted by the liquid phase. Figure 2.11 shows snapshots of impact dynamics on a super-hydrophobic sphere ($\theta_s = 150°$). The drop eventually bounces away from the sphere. The total mass error, ΔM, normalized by initial total mass, M_0, is shown in Figure 2.12 as a function of non-dimensional time, tu_0/d_d, for $\theta_s = 10°$, $30°$, $60°$, $90°$, $120°$, $150°$, respectively. The maximum mass error is less than 0.3% for all drop impact simulations.

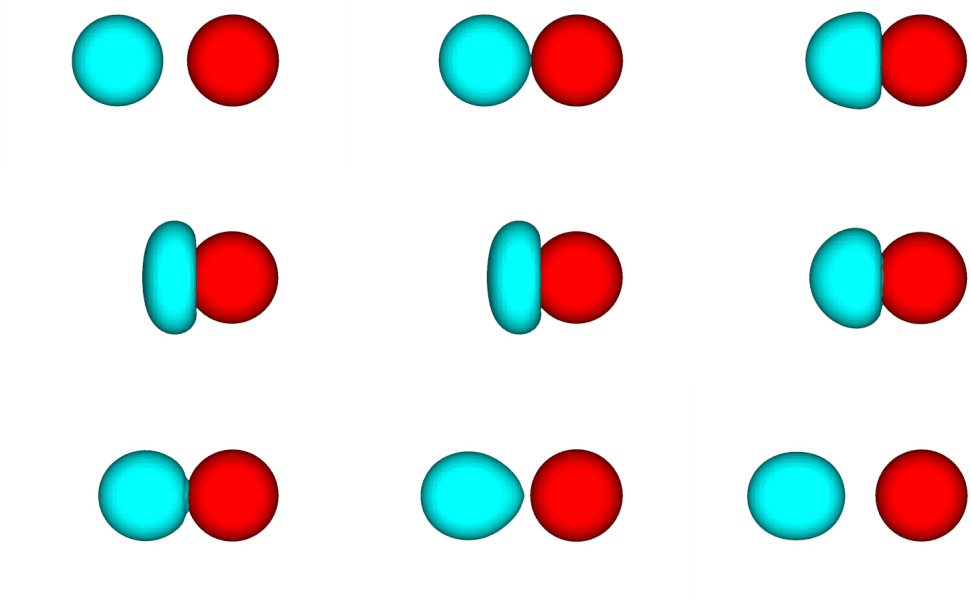

Figure 2.11: A drop impact on a hydrophobic sphere in 3D, $\theta_s = 150°$. The interval between two successive pictures is $\Delta t u_0/d_s = 0.25$ (from left to right and from top to bottom).

2.7.4 3D drop spreading on a sphere

We introduce a test case to verify our findings reported in the previous two subsections. The initial condition is shown in Figure 2.13. The radius of the drop is the same as the radius of the sphere. The center of the spherical drop is $0.98R$ away from the surface of the sphere. The physical parameters are: liquid density $\rho_L = 1000\,\mathrm{kg/m^3}$, liquid viscosity, $\mu_L = 0.001\,\mathrm{Pa \cdot s}$, surface tension coefficient $\sigma = 0.072\,\mathrm{Nm^{-1}}$, the static contact angle is $\theta = 60°$, the drop diameter is $D = 1\,\mathrm{mm}$, and the calculated Ohnesorge number is $\mathrm{Oh} = \frac{\mu}{\sqrt{\rho\sigma \mathrm{D}}} = 0.012$.

We measure the drop height throughout the spreading process. As shown in Figure 2.14, four resolutions are taken for the test, $R/\Delta x = 6$, 12, 24, 48. The spreading curves almost collapse in the inertial spreading regime. The oscillation

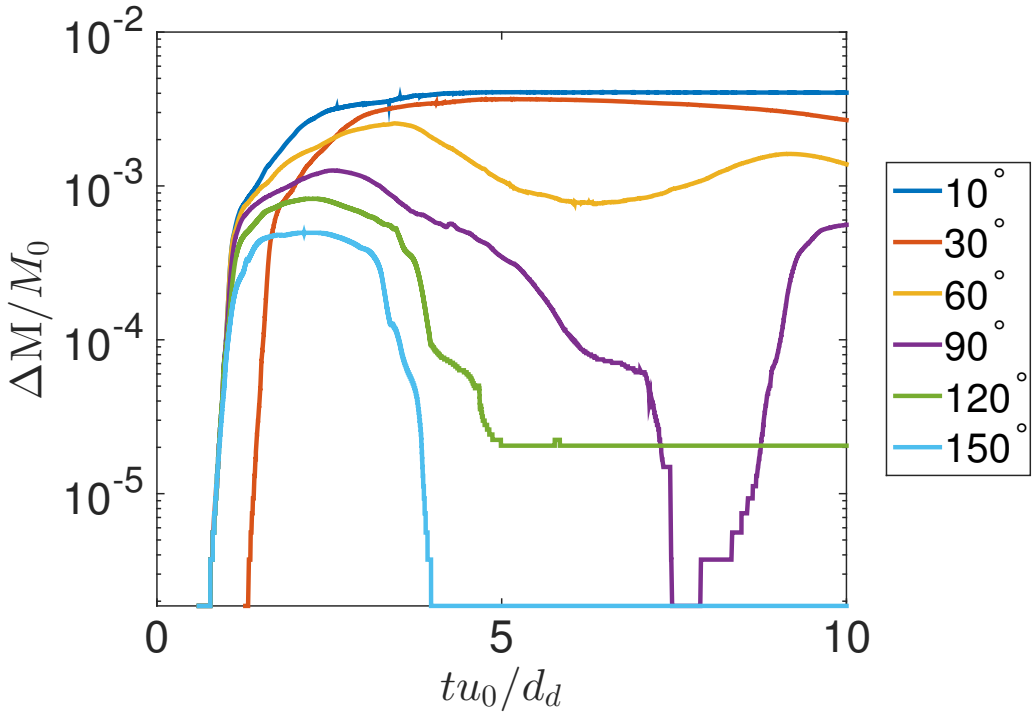

Figure 2.12: Mass error versus non-dimensional time for $\theta_s = 10°$, $30°$, $60°$, $90°$, $120°$, and $150°$.

amplitude is smaller on a finer mesh because more viscous dissipation is captured by the grid. The final heights seem to collapse. We choose three time spots, one in the inertial spreading regime, one close to the peak of the first oscillation, and the last one close to the equilibrium state. The liquid-gas interfaces are shown in Figure 2.15 at a range of resolutions, exhibiting good agreement with one another.

2.8 Conclusion

In this chapter, a numerical framework has been presented to simulate large-scale two-phase flows in complex geometries. The computational approach uses a conservative level-set method to capture the liquid-gas interface, a conservative immersed

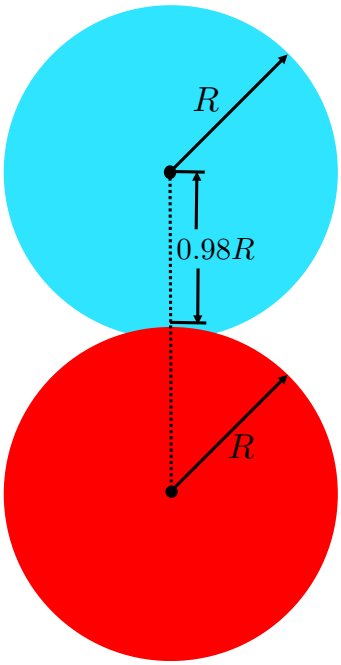

Figure 2.13: Initial condition for a drop spreading on a sphere.

boundary method to model the solid phase, and a curvature boundary method to model the static contact angle. This approach is verified to be accurate, conservative, and robust in simulating inertia dominated liquid-gas flows with moving contact lines.

2.9 Appendix

We compare the accuracy of the force method with the second modification method using the test case in Section 2.7.2. Our solution procedure for the force method has been illustrated in Section 2.6. We could easily adapt the algorithm for the force method to realize the second modification method. The solution procedure is graphically shown in Figure 2.16: pre-estimation of the liquid-gas interface normal is deleted, the extended variable is changed to $\cos(\phi_e)$, and the sub-grid surface

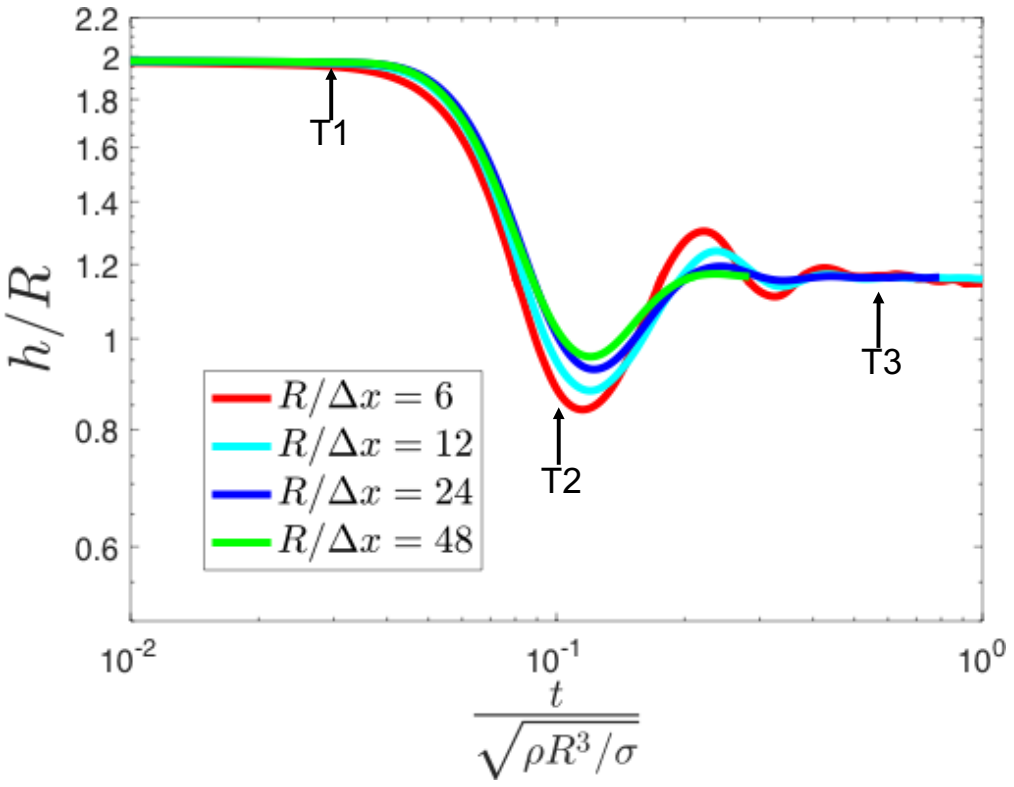

Figure 2.14: Evolution of drop height during spreading on a sphere in 3D.

tension force model is deleted. The mesh resolution is $R_0/\Delta = 24$. The other parameters are remain the same as the parameters in Section 2.7.2. A comparison of the computed spreading length from the force method with the counterpart from the second modification method is shown in Figure 2.17; the analytical spreading length is also drawn here for reference. Both methods are accurate in the spreading length. The difference is more obvious in Figure 2.18, which shows the L_∞ norm of error in the spreading length for both methods. For most contact angles, the force method is more accurate, except for the 170° case. As explained in Section 2.7.2, the errors in the height is better for accuracy measurement for the 170° case, so we then draw the L_∞ norm of errors in the height with solid markers. As predicted, the norm of the error in the drop height is smaller for the force method.

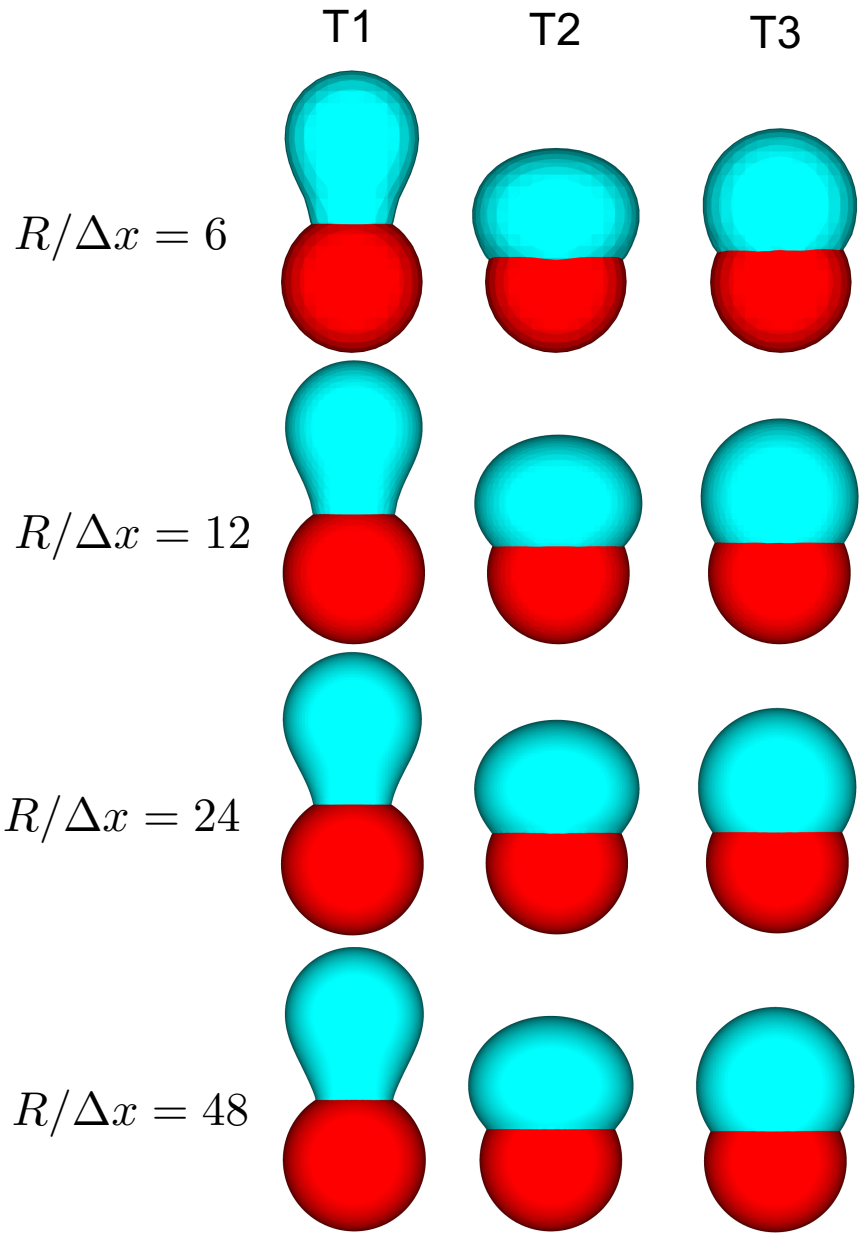

Figure 2.15: Drop shapes during spreading.

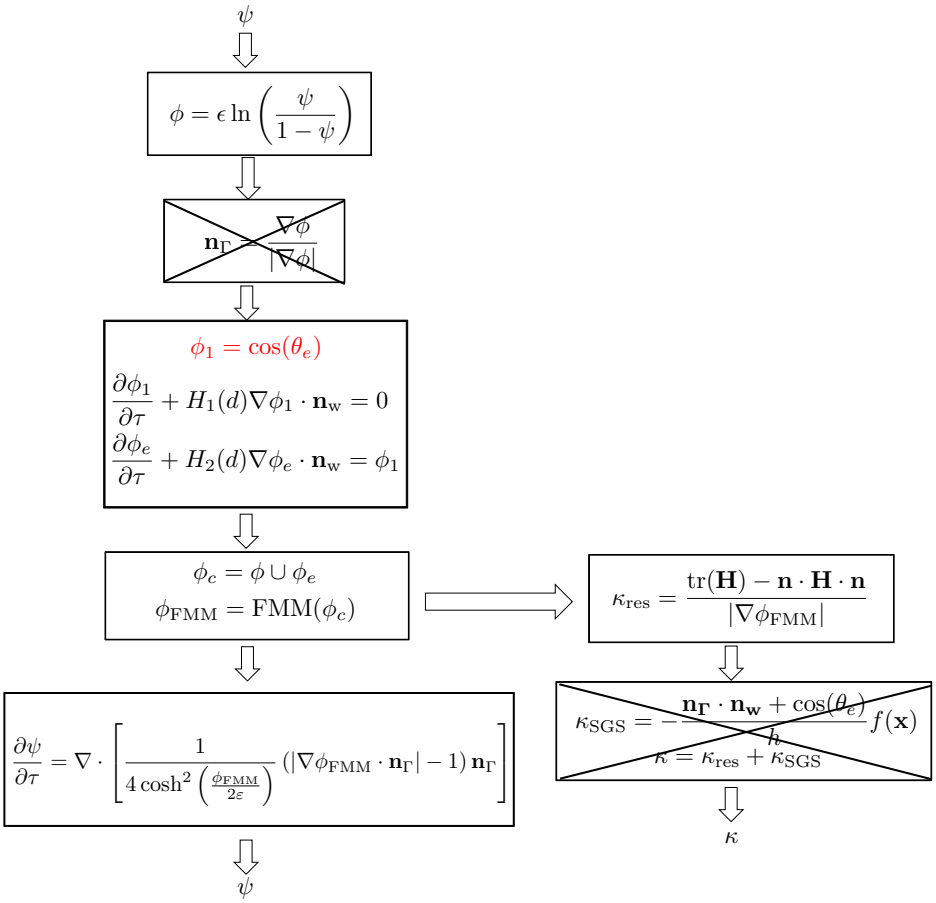

Figure 2.16: Flow chart of the solution procedure for the second modification method. Compared with the force method, the deleted steps are crossed out, the changed steps are colored in red.

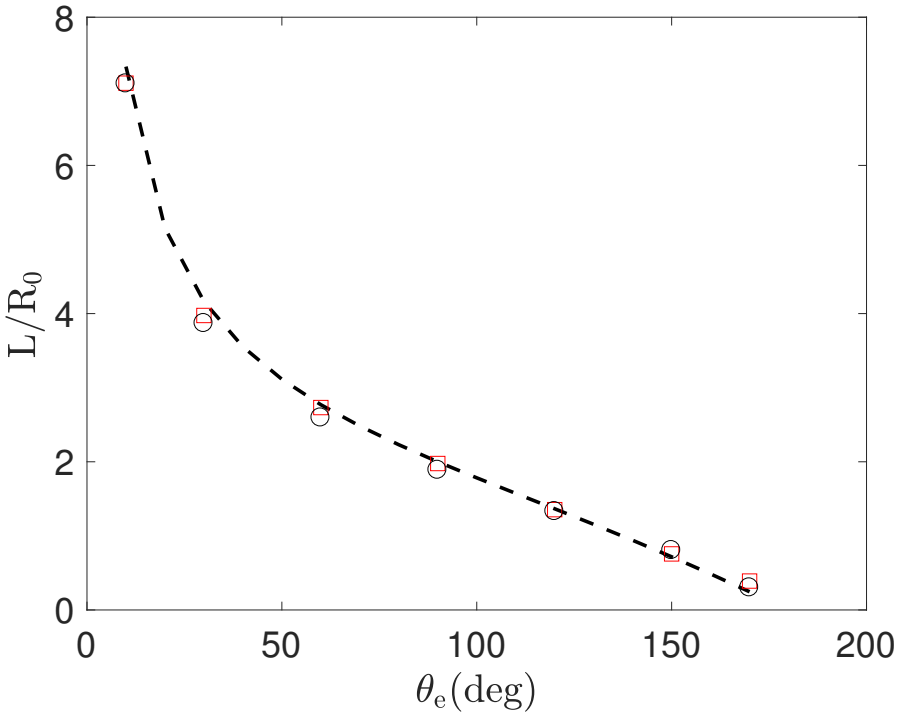

Figure 2.17: Normalized spreading length L/R_0 of the equilibrium drop versus the contact angle θ_e. The analytical normalized spreading length is shown with a dashed line $(--)$, the computed spreading length using the force method is shown by squares $(\square)$, the computed spreading length using the second modification method is shown by circles $(\bigcirc)$.

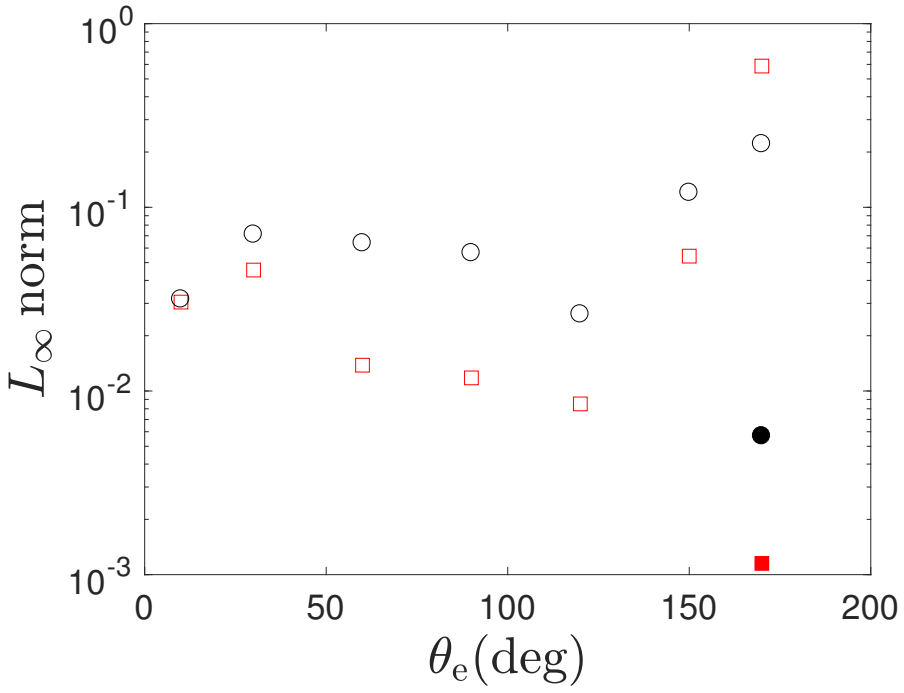

Figure 2.18: L_∞ norm of errors in spreading length or height versus the equilibrium contact angle. Force method, spreading length is shown by in squares (□). Force method, spreading height is shown by filled square (■). Second modification method, spreading length is shown by circles(◯). Second modification method, spreading height is shown by filled circles(●)

CHAPTER 3

MOVING CONTACT LINE MODEL

3.1 Introduction

Two-phase flows with moving contact lines are highly relevant to many natural phenomena and industrial applications such as internal combustion engines [99], micro-fluidic devices [23], fuel cells [38], etc. Detailed understanding and accurate modeling of contact line dynamics are required to optimize the performance of these engineering devices.

Performing accurate simulation of two-phase flows with moving contact lines is challenging because these flows are inherently multi-physics and multi-scale [8, 81, 85]. For instance, multiple physics, such as surface roughness [64, 5], surfactants [65, 87], or electrostatic effects [44], are difficult to resolve accurately in a single numerical framework. Moreover, the viscous stress diverges at the contact line while using the no-slip boundary condition, resulting in mesh-dependent simulations of flows dominated by the viscous force [3, 50].

We simplify our study by focusing on smooth surfaces and by ignoring surfactants and electrostatic forces. In context of the finite-volume approach [94], the weak form of the Navier-Stokes equations is solved, which avoids having to explicitly impose the slip boundary condition at the wall. Nevertheless, accurate simulations of contact line dynamics remain a challenging because of the complex flow physics that interact in the near-wall region. Figure 3.1 provides a schematic of the multi-scale flow near the moving contact line, which is divided into four representative regions based on the dominant local processes. In Region 1, the

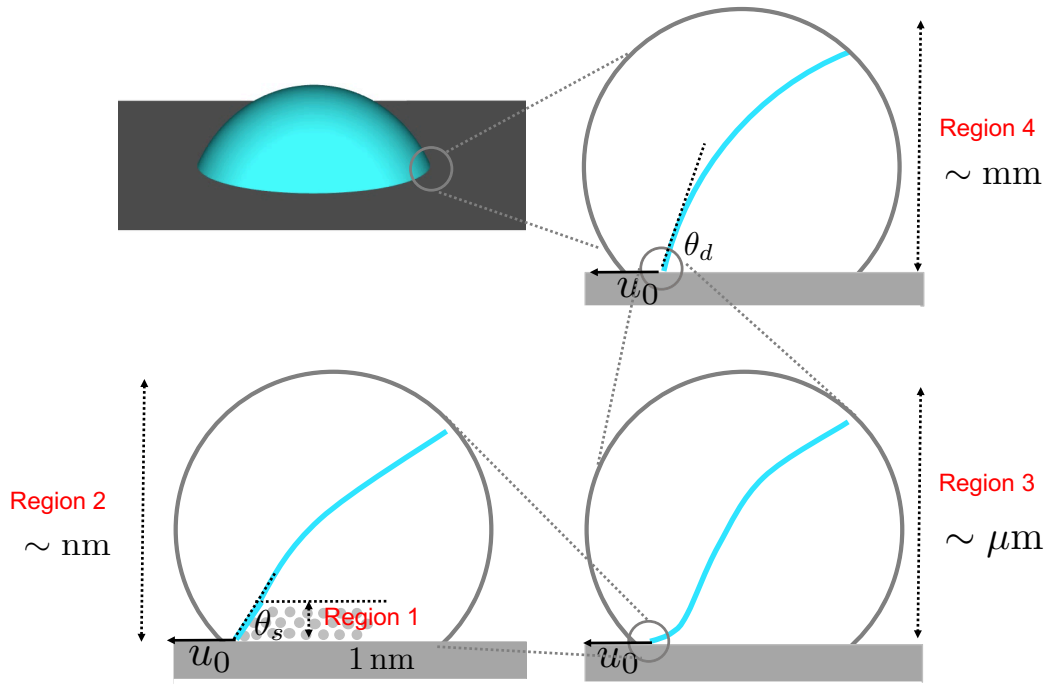

Figure 3.1: Schematic diagram of a partially-wetting drop spreading on a flat surface. This figure is adapted from Chen et al. [15].

flow is dominated by intermolecular forces [37]. The characteristic length scale of Region 1 is about $a = 1\,\text{nm}$. The flow in Region 2 is dominated by the Van der Waals force [37]. Because of this force, the surface tension coefficient varies as a function of the distance to the wall, resulting in concave bending of the two-phase interface [15] in this region. Region 2 extends over several nanometers [37]. Region 3 is dominated by the balance of viscous and surface tension forces, and the corresponding length scale is the visco-capillary length $l_\mu = \mu_l^2/(\sigma\rho_l)$ [8], where μ_l is the liquid dynamic viscosity, σ is the surface tension coefficient, and ρ_l is the liquid density. Finally, Region 4 is dominated by the balance of liquid inertia, gravitational, and surface tension forces, and its characteristic scale is the inertia-capillary length [8], $l_c = \sqrt{\sigma/(\rho_l g)}$. For a water drop, the visco-capillary length is about $0.01\,\mu\text{m}$, and the capillary length is about 2.7 mm. For a viscous fluid,

the visco-capillary length is much larger, therefore we estimate it to be around $1\,\mu$m. The huge scale-separation between the visco-capillary length and inertia-capillary length indicates that a 3D simulation that resolves the visco-capillary length would be enormously expensive. As a result, we aim to build a dynamic contact line model that accounts for the scales under the capillary length, namely Regions 1-3, to save the computational cost and to enable efficient simulations of two-phase flows with moving contact lines.

Currently, there exists primarily two types of modeling strategies: the Cox-Voinov dynamic model [20, 92] based on hydrodynamics; and the contact-line friction model [74, 16, 67] based on the Molecular Kinetic Theory (MKT) [100, 7]. Both of these models aim to relate the dynamic contact angle θ_d to the static contact angle θ_s by considering the balance between surface tension and another dominant process. The Cox-Voinov dynamic model considers hydrodynamics at a small contact angle in the context of the lubrication approximation, i.e., it balances surface tension with the viscous process. The contact-line friction model [7, 35] ignores bulk flow but focuses on the molecular force. These two models seem to be coexist and have been separately used in a number of numerical studies [3, 50, 83, 58, 32, 34, 84, 57, 82, 24]. Snoeijer and Andreotti [81], however, suggested to use MKT as a slip model for the molecular-scale boundary condition, in addition to rather than an alternative to the Cox-Voinov hydrodynamic model. These two modeling strategies did not consider inertia effect from the get-go, however, the influence of liquid inertia is not negligible even in some low speed flows [81]. To alleviate this issue, several recent theoretical [21], experimental [52, 6, 96, 73, 97] and numerical [58, 82] studies focused on characterizing inertial effect on contact line dynamics.

In this chapter, we propose a novel approach to analyze and model two-phase flows with moving contact lines. Starting from the volume-integrated form of the Navier-Stokes equations for two-phase flows with moving contact lines, we identify two unclosed terms at the wall in Section 3.2: a Sub-Grid Scale (SGS) surface tension force and an SGS viscous force. In Section 3.3, we perform simulations of drop spreading to demonstrate that the SGS surface tension force can be closed using the uncompensated Young's force method [94]. This method also leads to mesh-independent simulation results in inertia-capillary flows. In Section 3.4, we propose a simple flow model to estimate the SGS viscous force at the contact line. The new approach is also analytically compared with the Cox-Voinov model and the contact-line friction model. In Section 3.5, we show that using both SGS models leads to better mesh-independence of the predictions. Finally, 3D drop spreading on a horizontal plane and drops sliding down an inclined plane are studied using the proposed approach.

3.2 Volume-filtered Navier-Stokes equations around the contact line

Consider a flow problem in which coexist a liquid domain $\mathbb{L}$, a gas domain $\mathbb{G}$, and a solid region $\mathbb{S}$. The interface between fluid and solid (hereinafter referred to as the wall) is defined by $\mathcal{W} = (\mathbb{L} \cup \mathbb{G}) \cap \mathbb{S}$, and the interface between liquid and gas is $\mathcal{I} = \mathbb{L} \cap \mathbb{G}$. The triple-contact line is then given by $C = \mathcal{W} \cap \mathcal{I}$.

Consider a fixed fluid control volume Ω that is adjacent to the wall, but not overlapping with the solid region. We define the boundary of this control volume as $\partial\Omega$. We split $\partial\Omega$ into a portion that coincides with the wall, $\partial\Omega_{\mathcal{W}} = \partial\Omega \cap \mathcal{W}$,

and a portion that does not coincide with the wall, $\partial\Omega \backslash \partial\Omega_{\mathcal{W}}$. We are especially interested in the situation where $C \cap \Omega_{\mathcal{W}} \neq \emptyset$, i.e., some of the triple-contact line is present in the control volume.

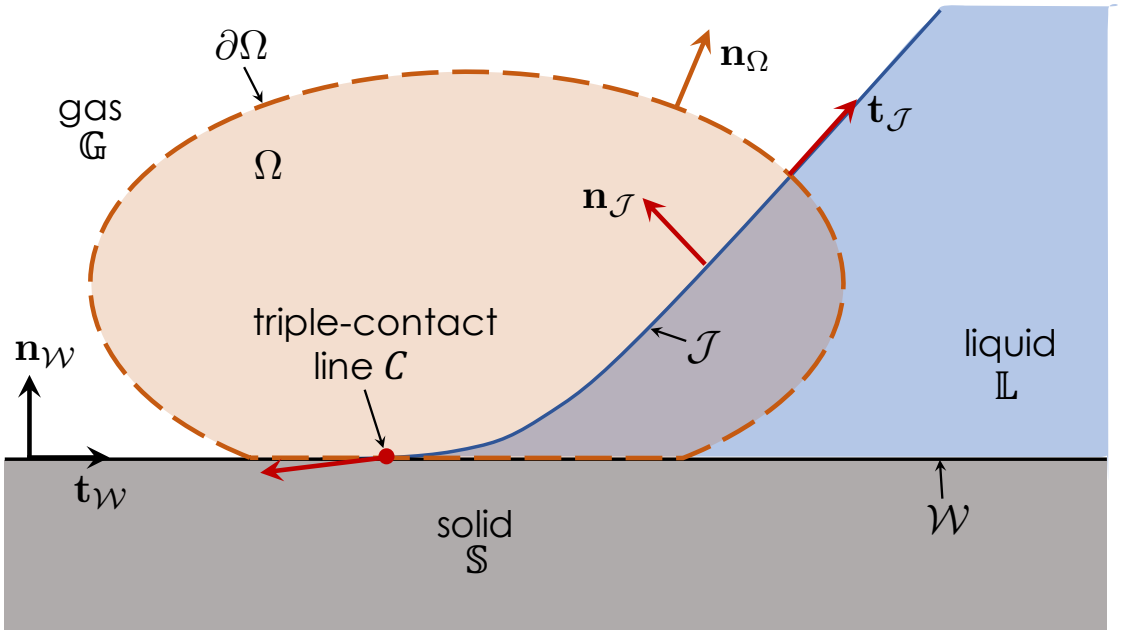

Figure 3.2: Schematics of a control volume around the triple-contact line. $\mathbf{t}_\mathcal{W}$ is the wall tangential vector, and $\mathbf{n}_\mathcal{W}$ is the wall normal vector.

For maximum relevance to finite volume-based two-phase flow solvers, we are interested in the integral form of the momentum conservation equation expressed over Ω, given by[1]

$$\frac{\partial}{\partial t}\int_\Omega \rho\mathbf{u}dV + \int_{\partial\Omega}(\rho\mathbf{u}\otimes\mathbf{u})\cdot\mathbf{n}_\Omega\, dS = \int_\Omega \rho\mathbf{g}dV + \int_{\partial\Omega}\boldsymbol{\tau}\cdot\mathbf{n}_\Omega\, dS + \int_{\mathcal{I}\cap\partial\Omega}\sigma\mathbf{t}_\mathcal{I}dl. \quad (3.1)$$

In this expression, $\mathbf{n}_\Omega$ is the outward-oriented normal vector of $\partial\Omega$, the gravitational acceleration is $\mathbf{g}$, the fluid density is ρ, its velocity is $\mathbf{u}$, and the stress tensor is $\boldsymbol{\tau} = -p\mathbf{I} + \mu\left(\nabla\mathbf{u} + \nabla\mathbf{u}^\mathsf{T}\right) - \frac{2}{3}\mu\nabla\cdot\mathbf{u}\mathbf{I}$, where $\mathbf{I}$ indicates the identity tensor, μ is

[1]For simplicity, integrals over a line, surface, and volume will respectively use dl, dS, and dV as differential variable.

the fluid dynamic viscosity coefficient, and p is the fluid pressure. The last term on the right-hand side of Eq. 3.1 accounts for the effect of surface tension: σ is the surface tension coefficient, and the liquid-gas interface tangential vector is defined at the control volume surface by $\mathbf{t}_{\mathcal{I}} = (\mathbf{n}_{\mathcal{I}} \times \mathbf{n}_{\Omega}) \times \mathbf{n}_{\mathcal{I}}$.

An overbar is introduced to indicate Ω-averaged quantities: for a variable ϕ, we have $\overline{\phi} = \frac{1}{|\Omega|} \int_{\Omega} \phi dV$, where the vertical brackets indicate the Lebesgue measure of the set. In addition, appropriate numerical fluxes need to be introduced to approximate the surface terms in Eq. 3.1. For an exact point-wise surface flux $\mathcal{F}$, we decompose it as $\mathcal{F} = \mathcal{F}_{\text{res}} + \mathcal{F}_{\text{SGS}}$, where the "res" subscript indicates the *resolved* numerical flux computed from volume-averaged quantities (over Ω and neighboring control volumes), and the "SGS" subscript indicates the error coming from unresolved (i.e., *sub-grid scale*) processes. Hereinafter, the assumption is made that Ω is large compared to the near-wall region in which occur the contact line processes described in the introduction. Specifically, we assume that the Ω extends into region 4. Moreover, it is assumed that all the other flow processes unrelated to contact line physics are properly resolved, i.e., are taking place on a scale much larger than Ω. Therefore, we assume that $\mathcal{F}_{\text{res}} \approx \mathcal{F}$ on $\partial\Omega \backslash \partial\Omega_{\mathcal{W}}$. In contrast, we expect that volume-averaged fluid variables will poorly approximate wall fluxes around the triple-contact line, and as such $\mathcal{F}_{\text{SGS}}$ is not negligible on $\partial\Omega_{\mathcal{W}}$ and needs to be modeled. With these observations, Eq. 3.1 is recast as

$$\frac{\partial}{\partial t}\overline{\rho\mathbf{u}} + \frac{1}{|\Omega|}\int_{\partial\Omega\backslash\partial\Omega_{\mathcal{W}}} \left[(\rho\mathbf{u}\otimes\mathbf{u})\cdot\mathbf{n}_{\Omega}\right]_{\text{res}} dS = \overline{\rho}\mathbf{g} + \frac{1}{|\Omega|}\int_{\partial\Omega}\left[\boldsymbol{\tau}\cdot\mathbf{n}_{\Omega}\right]_{\text{res}} dS + \frac{1}{|\Omega|}\int_{\mathcal{I}\cap\partial\Omega}\left[\sigma\mathbf{t}_{\mathcal{I}}\right]_{\text{res}} dl + \underbrace{\frac{1}{|\Omega|}\int_{\partial\Omega_{\mathcal{W}}}\left[\boldsymbol{\tau}\cdot\mathbf{n}_{\Omega}\right]_{\text{SGS}} dS}_{\mathbf{f}_{\tau\,\text{SGS}}} + \underbrace{\frac{1}{|\Omega|}\int_{\mathcal{I}\cap\partial\Omega_{\mathcal{W}}}\left[\sigma\mathbf{t}_{\mathcal{I}}\right]_{\text{SGS}} dl}_{\mathbf{f}_{\sigma\,\text{SGS}}}, \tag{3.2}$$

where $\mathbf{f}_{\sigma\,\text{SGS}}$ is the SGS surface tension force, and $\mathbf{f}_{\tau\,\text{SGS}}$ is the SGS viscous force. While the two SGS wall fluxes need to cancel each other in the wall-normal compo-

nent of Eq. 3.2, both terms remain in the wall-tangent components of the equation.

For the sake of simplicity and without significant loss of generality, it is useful to expand these terms under additional assumptions. For a locally flat wall, a Cartesian coordinate system is first introduced with the x and z coordinates varying along the wall and the y coordinate varying in the wall-normal direction. Correspondingly, we define the wall-tangent velocity components as u and w, and the wall-normal velocity component as v. While we focus on the u component of the velocity below, similar expressions can be obtained for the w component. Finally, a numerical formulation for the resolved fluxes at the wall is introduced:

$$\frac{1}{|\Omega|}\int_{\partial\Omega_{\mathcal{W}}} \left[\mathbf{e_x}\cdot\boldsymbol{\tau}\cdot(-\mathbf{e_y})\right]_{\text{res}}\, dS \approx -\frac{|\partial\Omega_{\mathcal{W}}|}{|\Omega|}\frac{\overline{u}\,\overline{\mu}}{d}, \tag{3.3}$$

$$\frac{1}{|\Omega|}\int_{\mathcal{I}\cap\partial\Omega_{\mathcal{W}}} \left[\sigma\mathbf{e_x}\cdot\mathbf{t}_{\mathcal{I}}\right]_{\text{res}} dl \approx \frac{|\overline{\mathcal{I}}\cap\partial\Omega_{\mathcal{W}}|}{|\Omega|}\sigma\mathbf{e_x}\cdot\mathbf{t}_{\overline{\mathcal{I}}}. \tag{3.4}$$

In Eq. 3.3, d is the distance between the centroid of Ω and the wall, and $\mathbf{e_x}$ and $\mathbf{e_y}$ are the unit vectors of the coordinate system. Note that in Eq. 3.4, the abusive notation $\overline{\mathcal{I}}$ is used to indicate the numerical reconstruction model for $\mathcal{I}$ within the control volume Ω. For example, $\overline{\mathcal{I}}$ might correspond to a planar reconstruction of the interface in the cell as provided by a VOF-PLIC [69] or a level set framework [79].

With these definitions, it is possible to express the SGS terms at the wall as

$$f^x_{\tau\,\text{SGS}} = \mathbf{e_x}\cdot\mathbf{f}_{\tau\,\text{SGS}} = \frac{1}{|\Omega|}\int_{\partial\Omega_{\mathcal{W}}} \left[\mathbf{e_x}\cdot\boldsymbol{\tau}\cdot(-\mathbf{e_y})\right]_{\text{SGS}}\, dS = \frac{1}{|\Omega|}\int_{\partial\Omega_{\mathcal{W}}} \mathbf{e_x}\cdot\boldsymbol{\tau}\cdot(-\mathbf{e_y})\, dS - \frac{|\partial\Omega_{\mathcal{W}}|}{|\Omega|}\frac{2\overline{u}\,\overline{\mu}}{\Delta}, \tag{3.5}$$

$$f^x_{\sigma\,\text{SGS}} = \mathbf{e_x}\cdot\mathbf{f}_{\sigma\,\text{SGS}} = \frac{1}{|\Omega|}\int_{\mathcal{I}\cap\partial\Omega_{\mathcal{W}}} \left[\sigma\mathbf{e_x}\cdot\mathbf{t}_{\mathcal{I}}\right]_{\text{SGS}} dl = \frac{1}{|\Omega|}\int_{\mathcal{I}\cap\partial\Omega_{\mathcal{W}}} \sigma\mathbf{e_x}\cdot\mathbf{t}_{\mathcal{I}}\, dl - \frac{|\overline{\mathcal{I}}\cap\partial\Omega_{\mathcal{W}}|}{|\Omega|}\sigma\mathbf{e_x}\cdot\mathbf{t}_{\overline{\mathcal{I}}}. \tag{3.6}$$

The closures of $\mathbf{f}_{\tau\,\text{SGS}}$ and $\mathbf{f}_{\sigma\,\text{SGS}}$ will be provided in detail in Section 3.3 and Section 3.4, respectively.

The above mathematical description is implemented in our in-house code NGA [29], which employs a conservative level-set method [31] to capture the liquid-gas interface. The pressure discontinuity due to surface tension is treated by the ghost fluid method [36]. The SGS surface tension force, i.e., Eq. 3.5, is implemented as a source term in curvature calculation [57, 94]. The volume-averaged Navier-Stokes equations are solved on a staggered grid with second-order spatial accuracy for both convective and viscous terms, and by the semi-implicit Crank-Nicolson scheme with second-order accuracy for time advancement. This computational strategy has been verified extensively [94, 95] and was found to be accurate, conservative, and robust for simulating 3D large-scale inertia-dominated liquid-gas flows with moving contact lines. The implementation of the SGS viscous force, i.e., Eq. 3.3, will be illustrated in Section 3.4.6, and its validation and verification will be demonstrated in Section 3.5.

3.3 SGS surface tension force model

We first derive a SGS surface-tension force model starting from Eq 3.6. The SGS surface tension force on the wall can be first written as

$$f_{\sigma\,\mathrm{SGS}} = \mathbf{e_x} \cdot \mathbf{f}_{\sigma\,\mathrm{SGS}} = \frac{1}{|\Omega|}\int_{\mathcal{I}\cap\partial\Omega_{\mathcal{W}}} \sigma \mathbf{e_x}\cdot\mathbf{t}_{\mathcal{I}}\, dl - \frac{|\overline{\mathcal{I}}\cap\partial\Omega_{\mathcal{W}}|}{|\Omega|}\sigma\mathbf{e_x}\cdot\mathbf{t}_{\overline{\mathcal{I}}}. \tag{3.7}$$

The surface tension coefficient is assumed to be constant. We define the expected contact angle as $\theta_{\mathcal{I}} = \cos^{-1}\left(\frac{1}{|\mathcal{I}\cap\partial\Omega_{\mathcal{W}}|}\int_{\mathcal{I}\cap\partial\Omega_{\mathcal{W}}} \mathbf{e_x}\cdot\mathbf{t}_{\mathcal{I}}\, dl\right)$, which is assumed to be same as the static contact angle θ_s. The resolved contact angle can be calculated as $\theta_{\overline{\mathcal{I}}} = \cos^{-1}(\mathbf{e_x}\cdot\mathbf{t}_{\overline{\mathcal{I}}})$, which is equal to $\cos^{-1}(\mathbf{e_y}\cdot\mathbf{n}_{\overline{\mathcal{I}}})$. The liquid-gas interface is assumed to be smooth and to be with a small curvature, resulting in $|\mathcal{I}\cap\partial\Omega_{\mathcal{W}}| = |\overline{\mathcal{I}}\cap\partial\Omega_{\mathcal{W}}|$. Eq 3.7 is then simplified to

$$f_{\sigma\,\mathrm{SGS}} = \frac{|\mathcal{I} \cap \partial\Omega_{\mathcal{W}}|}{|\Omega|}\sigma\left(\cos\left(\theta_s\right) - \cos\left(\theta_{\overline{\mathcal{I}}}\right)\right). \tag{3.8}$$

Evaluation of $|\mathcal{I} \cap \partial\Omega_{\mathcal{W}}|$ can be different for various numerical frameworks. However, when the ghost fluid method [36] is employed to calculate the pressure jump, $|\mathcal{I} \cap \partial\Omega_{\mathcal{W}}|$ is estimated as Δ, and $|\Omega|$ is Δ^3, where Δ is the grid size in numerical simulations. This SGS surface force is similar to the uncompensated Young's force [26], because both of them are caused by the difference between the current contact angle and the imposed contact angle. Some contact angle models, such as the curvature boundary method [94, 57] and the continuum surface force (CSF) method [58, 24], are in the same fashion.

An SGS surface-tension force model can be developed and verified even without an SGS viscous force model in inertia-capillary flows, because in such flows the inertial and surface tension forces are dominant, and the viscous force is negligible compared to the inertial force. Numerical simulations with only an SGS surface-tension force model, such as a low-viscous drop spreading on a plane [94] and a drop impacting on a plane [86] or a fiber [95], have been found to be mesh-independent and physically accurate, as the inertia force and surface tension force are mesh-independent.

However, the result might be different in flows that viscosity is not negligible. To demonstrate it, we simulate a high-viscous spontaneous drop spreading, because this flow has not only a inertia-capillary regime, but also a viscosity-capillary regime, as illustrated by the mass-spring-dashpot analogy in Section 3.7.1. From the beginning of the spreading to $t = T_c$, the dynamics is dominated by the balance of inertia and the surface tension force, where $T_c = \sqrt{\rho_l R^3/\sigma}$ is the the capillary time. In this inertia-capillary regime, the corresponding spreading law is $r \sim$

$t^{1/2}$ [96], where r is the radius of the wetting area. After T_c, the viscous force gains relative strength and the drop approaches its equilibrium shape. In this viscosity-capillary regime, the corresponding spreading law is Tanner's law $r \sim t^{1/10}$ [88]. Both spreading laws have been validated in experiments [6, 96] and simulations [50, 94, 24].

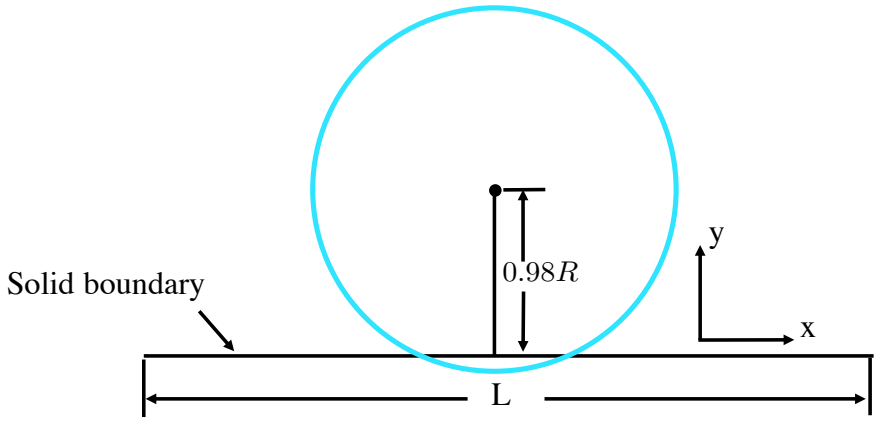

Figure 3.3: Initial condition for simulating spontaneous spreading of a drop.

In this test, a drop is initially placed $0.98R$ away from the wall, as shown in Figure 3.3. The initial distance has negligible impact on the spreading dynamics [50]. $L = 7R$ is the length of the wall, which is chosen to be large enough to ensure that the simulation results are independent of the domain size. The physical parameters for the simulation are provided in Table 4.5. Note that gravity is ignored in this test. The corresponding Ohnesorge number is $\text{Oh} = \mu_l/\sqrt{\rho_l \sigma R} = 0.21$. This numerical set-up will be also used in the analysis and simulations in following sections. The radius of the wetting area r, the total surface tension force in x direction $F_\sigma = 1/2 \oint_{\mathcal{I}} \sigma \mathbf{t}_{\mathcal{I}} \cdot \mathbf{e}_\mathbf{x} dl$, and the total viscous force on the wall $F_\tau = l_z \int_{\mathcal{W}} \frac{\mu u}{d} dx$ are monitored as a function of time t, where l_z is the depth in z direction. Note that F_σ contains the SGS surface tension force, and F_σ is normalized by $F_{\sigma_0} = \sigma R$. F_τ is normalized by $F_{\tau_0} = \mu_l v_s l_z$, where $v_s = \sqrt{\sigma/(\rho_l R)}$ is the capillary wave speed of

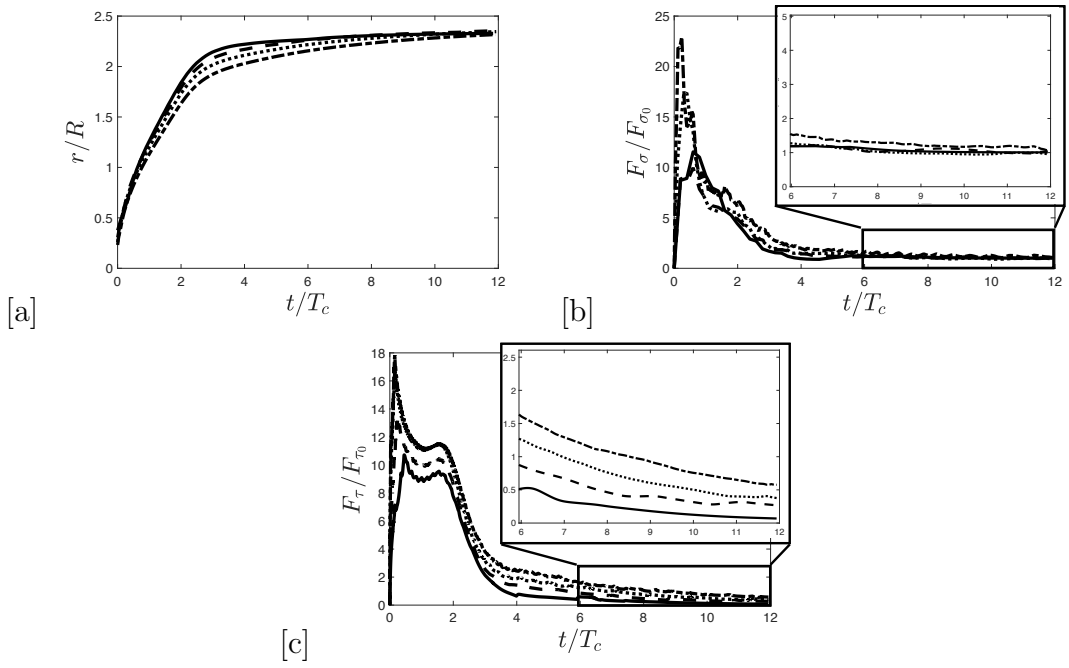

Figure 3.4: Evolution of the wetting radius, total surface tension force, total viscous force, and force ratios. [a] wetting radius, [b] total surface tension force F_σ, [c] total viscous force, F_τ. Results shown are for resolutions $R/\Delta = 9(-)$, $18(--)$, $36(\cdots)$, and $72(-\cdot)$.

the drop. Time t is normalized by the capillary time scale T_c.

The radius of the wetting area, total surface tension force, and total viscous force on the wall are shown in linear-linear scale in Figure 3.4. Four resolutions are considered, namely $R/\Delta = 9$, 18, 36, and 72. As expected, the impact of resolution on the radius of the wetting area is negligible in the inertia-capillary regime, i.e., when $t/T_c < 1$. Differences become significant in the viscosity-capillary regime ($t/T_c > 1$). As shown in Figure 3.4.b, F_σ is nearly mesh-independent by the end of spreading, as the shapes of the drop are nearly identical. F_σ is somewhat oscillatory due to numerical spurious current [1], so a running average was applied. Strong mesh dependence is observed in the total viscous force, as shown in Figure 3.4.c. Two conclusions can be drawn from these results: first, with the SGS surface tension force model, the total surface tension force is mesh-independent, resulting

in mesh-independent simulations in the inertia-capillary spreading regime, which agrees with various previous simulations, such as low viscous drop spreading on a plane [94], and the drop impact on a plane [86] or a fiber [95]. Second, the total viscous force on the wall is mesh-dependent, indicating the requirement for an SGS viscous force model.

3.4 SGS viscous force model

3.4.1 Formulation

In this section, we will first provide a simple flow model to estimate the viscous force on the wall. The resulting model is then compared to the Navier-slip boundary condition, the Cox-Voinov model, and the contact-line friction model. Derivation and implementation of the SGS viscous force model is presented at the end of this section.

As illustrated in Figure 3.5, we consider a wedge flow, in which the liquid-gas interface movies to the left at velocity u_0. Here the liquid-gas interface is assumed to be planar for simplicity. This hypothesis will be discussed in Section 3.4.2. We assume the dynamic viscosity of gas is much lower than the liquid viscosity, therefore the shear force caused by the gas phase is neglected. We solve the Navier-Stokes equations that govern the liquid inside the thin control volume in red as shown in Figure 3.5 in Cartesian coordinates. The flow is assumed to have reached steady state, and the inertial term and the pressure gradient term are negligible. The velocity boundary conditions are $u|_{y=0} = 0$ and $u|_{y=h} = u_0$, where h is the height of the liquid-gas interface. No viscous stress appears on the free interface [26], thus

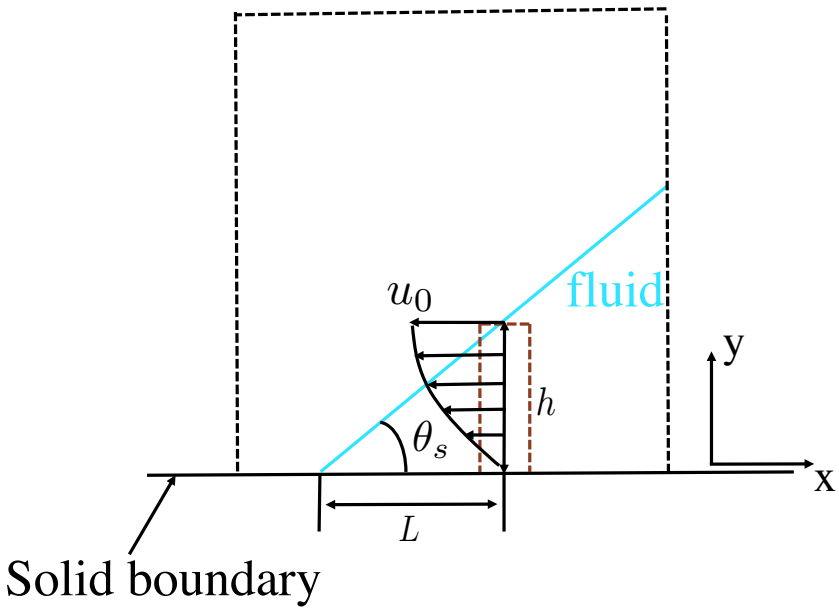

Figure 3.5: Schematics illustrating a computational cell with a contact line. The liquid gas interface is moving to the right. The liquid-gas interface is draw in linear form for the convenience of explanation.

we also have $\partial u/\partial y|_{y=h} = 0$. In this case, the Navier-Stokes equations integrate to $u(y) = u_0(2y/h - y^2/h^2)$ and the viscous stress on the wall is given by

$$\mu_l \frac{du}{dy}\bigg|_{y=0} = 2\mu_l \frac{u_0}{h}. \tag{3.9}$$

The total shear force on the wall in that cell is then integrated in to

$$F_\tau = \int_0^{l_z} \int_{l_s}^{l_m} \frac{2\mu_l u_0}{h(x)} dx dz = \frac{2\mu_l u_0 l_z}{\tan(\theta_s)} \ln\left(\frac{l_m}{l_s}\right), \tag{3.10}$$

where l_z is the depth in z direction; l_m is the macroscopic length, which is at the scale of the size of the control volume, and l_s is a small cutoff length to make the integral finite. When assuming the no-slip condition $l_s = 0$ at the contact point, the viscous force diverges. This is often referred to as the Huh and Scriven's

paradox [41], which indicates that a slip length, i.e., $l_s > 0$, should be introduced into this estimation. Eq 3.10 is the proposed model to estimate the viscous force at the contact line, which is the same as the estimation of the viscous force in studies of drop spreading [55] and free surface flows [80]. Note that Louge and Sahoo [55] and Snoeijer [80] used the height averaged velocity, $\bar{u} = \frac{1}{h}\int_0^h u(y)dy = \frac{2}{3}u_0$, rather than the interface velocity u_0 in their calculation.

3.4.2 Is the linear approximation valid?

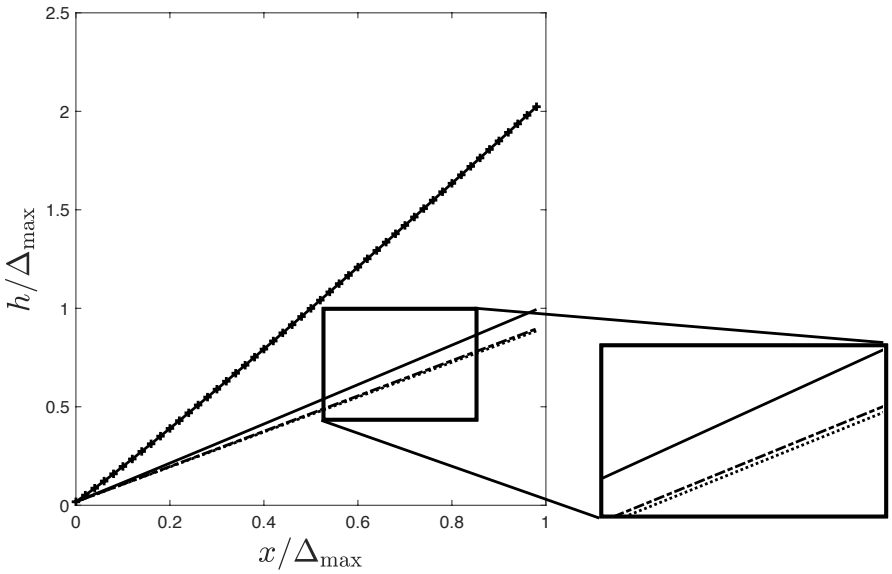

Figure 3.6: Evaluation of linear approximation of the liquid-gas profiles at different capillary numbers. Results shown are for Eq 3.11 with Ca = $10^{-5}(\cdots)$, $10^{-4}(-\cdot)$, $10^{-3}(-)$, and $10^{-2}(-+)$.

Before implementing the viscous force model, the validity and effect of the planar approximation on F_τ need to be confirmed. The planar approximation can be improper if the liquid-gas interface is highly curved. For comparison, we

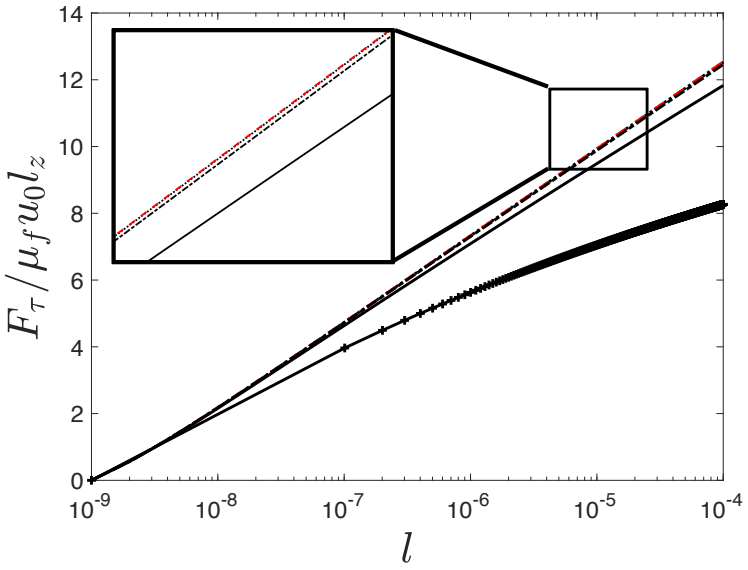

Figure 3.7: Estimated total viscous force for different capillary numbers. Results shown are for Eq 3.11 with Ca $= 10^{-5}(\cdot\cdot\cdot)$, $10^{-4}(-\cdot)$, $10^{-3}(-)$, and $10^{-2}(-+)$ using Eq 3.11 and Eq 3.10$(--)$.

integrate the Cox-Voinov model,

$$h'^3(x) = \theta_s^3 + 9\mathrm{Ca}(\frac{x}{l_s}), \tag{3.11}$$

up to $0.1R$, where R is the drop radius in Section 3.3. The slip length is estimated as $l_s = 1.0\,\mathrm{nm}$ [37]. The liquid-gas interfaces for various capillary numbers are shown in Figure 3.6. The range of the capillary number is calculated from the simulations reported in Section 3.3. The estimated total viscous forces for various capillary numbers using Eq 3.11 are compared with Eq 3.10 in Figure 3.7 as a function of the distance to the cut-off length. Note that we deliberately plot the distance to the cut-off length in a dimensional form, so that we can easily estimate the viscous force using physical parameters in this plot. As expected, the proposed model matches better with the Cox-Voinov model at lower capillary numbers, because the liquid-gas interfaces are expected to be less bent at lower capillary numbers. The total viscous forces estimated by the proposed model are always greater than

those estimated by the Cox-Voinov model, but the differences are not significant as shown in Figure 3.7.

3.4.3 Analysis of the Navier-slip boundary condition

To alleviate the singular viscous stress at the contact lines [41], researchers often introduce a slip length at the boundary [50, 83]. This boundary condition is the so-called Navier-slip boundary condition. Numerical simulations [50, 83] have shown to be less mesh-dependent with a larger slip-length. In this section, we use our simple flow model to analyze the behavior of the the Navier-slip boundary condition. We estimate the total viscous force by integrating the viscous stress at the contact line up to the drop radius R. The viscous force $F_{\tau\,\mathrm{tol}}$ can be found as

$$F_\tau = \int_0^{l_z} \int_\Delta^{\Delta_{max}} \frac{2\mu_l u_0}{h+h_s} dx dz = \frac{2\mu_l u_0 l_z}{\tan\theta_s} \ln\left(\frac{\Delta_{max}+h_s}{\Delta+h_s}\right), \tag{3.12}$$

where Δ is the grid-size, h_s is the numerical slip length.

In Figure 3.8, the estimated viscous forces are plotted as a function of the mesh size which are tested in Section 3.3. Here the viscous forces are normalized by $F_{\tau 0} = \frac{2\mu_l u_0 l_z}{\tan\theta_s} \ln\left(\frac{R}{l_s}\right)$, where we set l_s as the physical slip length $l_s = 1.0\,\mathrm{nm}$ [37], and $F_{\tau 0}$ is the expected viscous force. See in the case with $h_s = 1.0 \times 10^{-4}\,\mathrm{m}$ ($\square$), the total viscous forces have less dependence on Δ comparing to other cases with a smaller slip-length. This less mesh-dependent viscous force can lead to less mesh-dependent simulations, which has been observed in the simulation results given by Legendre and Maglio [50]. However, the total viscous force is greatly underestimated at large slip-lengths, as shown in their ratios with the expected viscous force. In short, the Navier-slip boundary condition could lead to less mesh-dependent simulations with an unrealistically large slip-length, but these simulations are physi-

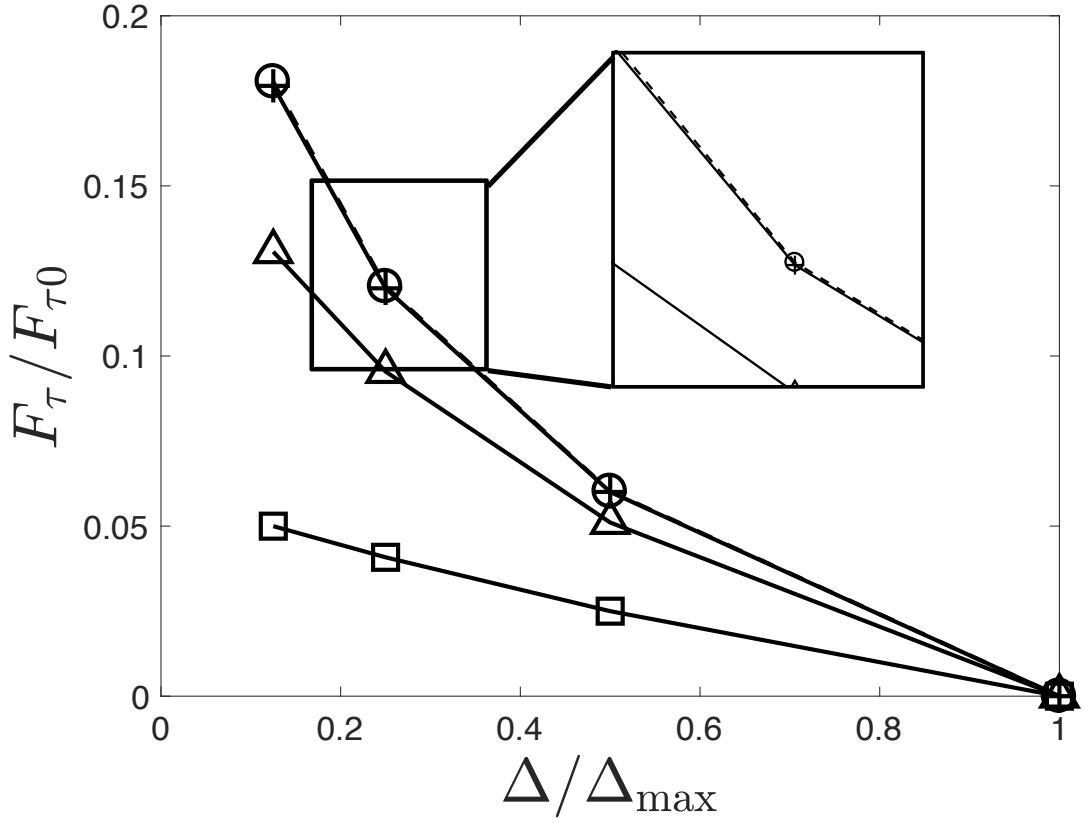

Figure 3.8: Estimated viscous force on the wall using the Navier-slip boundary. Results shown are for different slip length, $h_s = 0\,\mathrm{m}\,(\bigcirc), 2 \times 10^{-7}\,\mathrm{m}\,(+), 1.25 \times 10^{-5}\,\mathrm{m}\,(\triangle), 1.0 \times 10^{-4}\,\mathrm{m}\,(\square)$.

cally inaccurate because the total viscous force is under-estimated.

3.4.4 Analysis of the Cox-Voinov model

In this subsection, we present a comparison between the viscous force model and the Cox-Voinov model. The Cox-Voinov model is a dynamic contact-angle model, which indicates that the implementation of this model in a simulation is closely related to the numerical method to impose the contact angle. Therefore we first briefly introduce a numerical method that is commonly used to impose the contact

angle, then provide the comparison.

Many numerical methods [3, 82, 58, 24] have been proposed to impose the contact angle at the wall. Here we still use the uncompensated Young's force method to be consistent with our previous analysis, but also because the method is conceptually similar to the continuum surface force (CSF) approach that has been widely used in the Volume of Fluid (VOF) method [58, 24]. Both the uncompensated Young's force and the CSF methods implicitly impose the angle exactly at the wall.

To impose the dynamic contact angle, we rewrite the uncompensated Young's force as

$$\mathbf{f}_{\sigma\,\mathrm{SGS}} = \sigma \frac{\cos(\theta_d) - \cos(\theta)}{d} \mathbf{t}_{\mathcal{W}} \delta_{\Gamma}, \tag{3.13}$$

with

$$\cos(\theta_d) = \cos(\theta_s) - \frac{3\mathrm{Ca}\sin(\theta_s)}{\theta_s^2} \ln\left(\frac{l_m}{l_s}\right). \tag{3.14}$$

where δ_{Γ} is the resolved the Dirac distribution, $\mathbf{t}_{\mathcal{W}} = (\mathbf{n}_{\mathcal{W}} \times \mathbf{n}_{\overline{\mathcal{I}}}) \times \mathbf{n}_{\mathcal{W}}$ is the wall tangential vecto. Eq 3.14 is derived by Taylor-expanding the Cox-Voinov model twice by assuming small capillary numbers. Substituting Eq 3.14 into Eq 3.13, we find

$$\mathbf{f}_{\sigma\,\mathrm{SGS}} = \sigma \frac{\cos(\theta_s) - \cos(\theta)}{d} \mathbf{t}_{\mathcal{W}} \delta_{\Gamma} - 3\mathrm{Ca} \frac{\sin(\theta_s)}{\theta_s^2} \ln\left(\frac{l_m}{l_s}\right) \mathbf{t}_{\mathcal{W}} \delta_{\Gamma}, \tag{3.15}$$

in which the first term is the surface tension force, and the second term is a viscous force. Note that these forces are written as the force per unit volume. The magnitude of the viscous force is $3\frac{\mu_l \overline{u}}{d\Delta} \frac{\sin(\theta_s)}{\theta_s^2} \ln\left(\frac{l_m}{l_s}\right)$, where $\overline{u} = \frac{2}{3} u_0$ is the the height averaged velocity. For comparison, we rewrite the viscous force in Eq 3.10 also as the force per unit volume form

$$f_{\tau} = \frac{2\mu_l u_0}{\tan(\theta_s)\Delta^2} \ln\left(\frac{l_m}{l_s}\right). \tag{3.16}$$

In the context of the CSF method in VOF, $d = \Delta$, and by assuming a small contact angle, i.e., $\tan(\theta) \approx \sin(\theta) \approx \theta$, then the magnitude of the viscous force in the Cox-Voinov model is exactly same as the viscous force given by Eq 3.10.
Two other points should be noted:

- We analytically proved for the first time that the Cox-Voinov model contains a mesh-dependent viscous force as shown in Eq 3.15. This viscous force is much greater than the resolved viscous force in the previous simulations [3, 50].
- However, as shown in Eq 3.15, the viscous force should be effective in the wall tangential direction. A mismatch in the effective direction of the SGS viscous force can lead to a smaller effective viscous force on the wall, which possibly explains that the viscous force is under-estimated in the study of sliding drops down an inclined plane [58].

3.4.5 Analysis of the contact-line friction model

The contact-line friction model [74, 35, 13, 16, 67] attributes the contact line friction at the macro-scale (Region 4 in Figure 3.1) to the molecular interactions [100, 7] and ignores the viscous force from the continuum phase. One clear discrepancy is that the Molecular Kinetic theory can not explain the friction coefficient's contact-angle dependency that has been reported in Carlson et al. [13] (see in Figure 3.9). Here we provide an alternative interpretation of the contact angle friction factor β_f by attributing the friction to the enhanced viscous force cause by the contact angle-induced large-scale separation. According to Carlson et al. [13], the viscous dissipation at the contact line can be estimated as the

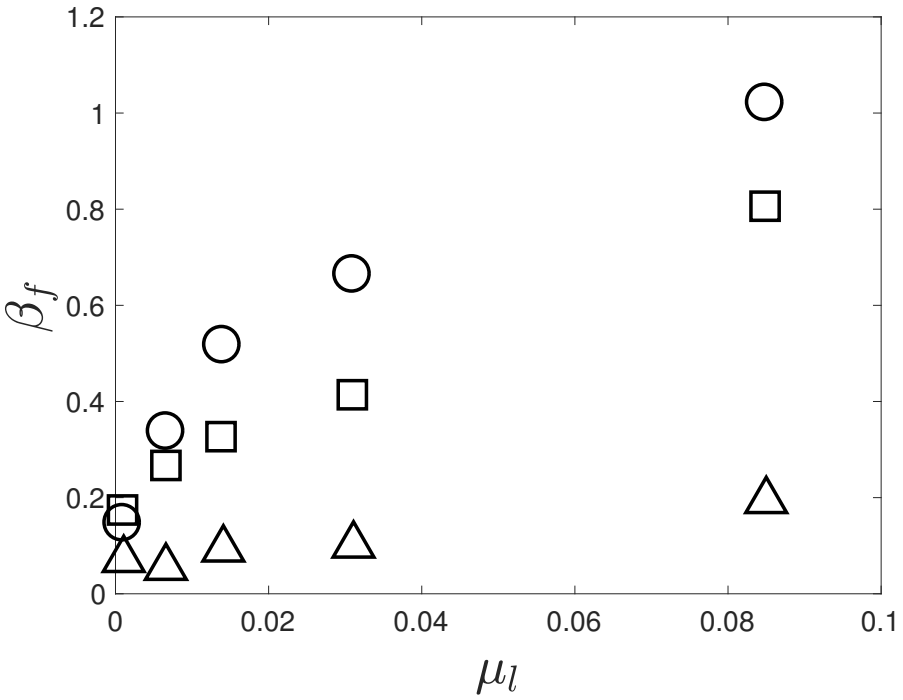

Figure 3.9: Measured contact line friction β_f as a function of the liquid dynamic viscosity μ_l. Results shown are for different static contact angles, $\theta_s = 20°$ (◯), $\theta_s = 60°$ (□), $\theta_s = 109°$ (△). Experimental data is from Carlson et al. [13].

$\beta_f u_0^2 = \frac{2\mu_l u_0^2}{\tan(\theta_s)} \ln\left(\frac{l_m}{l_s}\right)$. Then we have

$$\beta_f = \frac{2\mu_l}{\tan(\theta_s)} \ln\left(\frac{l_m}{l_s}\right). \tag{3.17}$$

The friction factor β_f is proportional to the liquid dynamic viscosity, which agrees with experimental measurements [13], as shown in Figure 3.9. Equation 3.17 confirms that the friction coefficient is higher for smaller contact angles. The friction factor also depends on l_m, indicating that the scale at which the measurement is performed. This property requires accurate experimental measurement. We include a scale-dependent strategy to integrate the molecular kinematic theory in the Appendix.

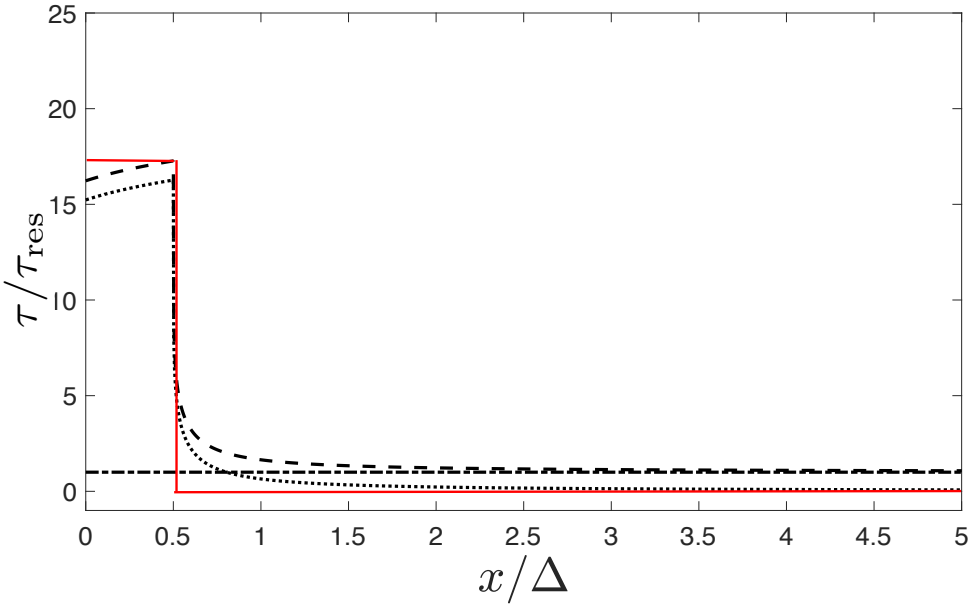

Figure 3.10: Normalized filtered viscous stress, resolved viscous stress, and SGS viscous stress as a function of their distance to the contact point. Results shown are for the filtered viscous tress $\overline{\tau}$ $(--)$, the resolved viscous stress τ_{res} $(\cdot-)$, the SGS viscous stress τ_{SGS} $(\cdots)$, and the implemented SGS viscous stress model $(-)$.

3.4.6 Numerical implementation

In Section 3.4.1, we derived an analytical expression of the viscous stress (or viscous force) around the contact line, but its implementation in context of the weak form of the Navier-Stokes equations has not been covered yet. In this subsection, we compare the expected viscous stress and the resolved viscous stress to identify the SGS viscous stress, and then illustrate its numerical implementation.

For simplicity, all the stresses are written in 2D form. The expected viscous tress is $\tau_{\mathrm{exp}} = \frac{1}{\Delta}\int_{x-0.5\Delta}^{x+0.5\Delta} \tau dx$, where $\tau = \mu_l \frac{\partial u}{\partial y} = 2\mu_l \frac{u_0}{y}$, $y = x\tan(\theta_s)$, and Δ is the size of the control volume. Note that for $x \leqslant 0.5\Delta$, the expected viscous stress is evaluated as $\tau_{\mathrm{exp}} = \frac{1}{\Delta}\int_{h_s}^{x+0.5\Delta} \tau dx$, because the gas viscosity is much lower than the liquid viscosity, then the viscous stress from the gas phase is ignored. The

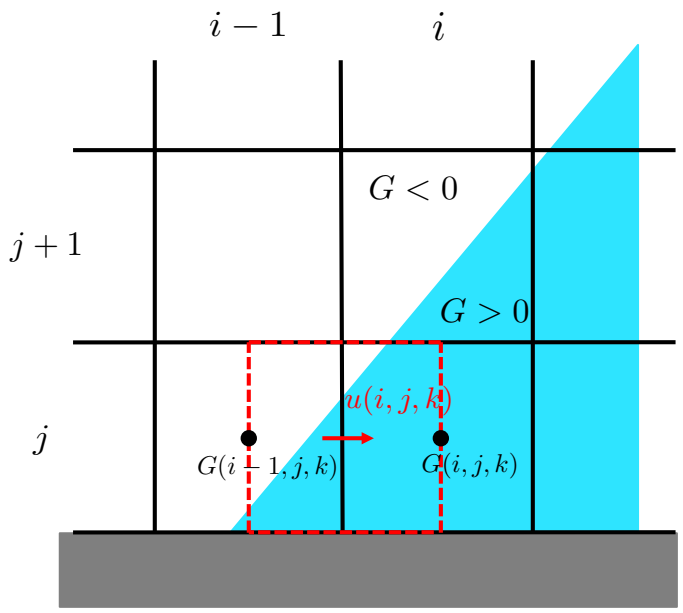

Figure 3.11: A u velocity cell across the interface. G is the classical signed distance level-set function, defined by $G(\mathbf{x}) = \|\mathbf{x} - \mathbf{x}_\Gamma\|$ where $\mathbf{x}_\Gamma$ is the location on the interface Γ that provides the minimum Euclidean distance from location $\mathbf{x}$. $G(\mathbf{x}) > 0$ is in the liquid phase, and $G(\mathbf{x}) < 0$ is in the gas phase.

resolved viscous stress is evaluated using the volume-averaged velocity $\overline{u}$, and the stress is calculated as $\tau_{\text{res}} = \tau(\overline{u}) = \mu_l \frac{\partial \overline{u}}{\partial y} = 2\frac{\mu_l u_0}{y}\left(1 - \frac{\Delta}{3y}\right)$. $\tau(\overline{u})$ and τ are not identical, because the distribution of $u(y)$ is parabolic rather than linear. Then, the SGS viscous stress is calculated, $\tau_{\text{SGS}} = \tau_{\text{exp}} - \tau_{\text{res}}$. In Figure 3.10, the expected viscous stress normalized by the resolved viscous stress is plotted as a function of the distance between the center of the control volume and the contact point, along with the resolved viscous stress and SGS viscous stress. In this calculation, the slip length is chosen to be close to the physical slip length, i.e., $h_s = 1 \times 10^{-9}$ m, and the filter size is chosen to be one tenth of the capillary length, i.e., $\Delta = 1 \times 10^{-4}$ m. For $x > 0.5\Delta$, the SGS viscous stress is close to zero, as the resolved viscous stress is close to the filter viscous stress; for $x < 0.5\Delta$, the SGS viscous stress is nearly the same as the expected viscous stress, as the resolved viscous stress is much smaller

than the filter viscous stress. The volume filter seems to spatially segregate the SGS viscous force into two segments, therefore we propose a modeling strategy in the same fashion: for $x > 0.5\Delta$, $\tau_{\mathrm{SGS}} = 0$; for $x < 0.5\Delta$, $\tau_{\mathrm{SGS}} = \frac{1}{\Delta}\int_{h_s}^{\Delta} \tau dx$. This model is plotted in red solid line in Figure 3.10.

In the numerical implementation, the mesh size is same as the size of the control volume. Then, the SGS viscous stress is integrated, giving rise to the SGS viscous force per unit volume,

$$\mathbf{f}_{\tau\,\mathrm{SGS}} = \frac{2\mu_f \mathbf{u}}{\Delta^2 \tan(\theta_s)} \ln\left(\frac{\Delta}{h_s}\right). \tag{3.18}$$

The volume-averaged Navier-Stokes equations are solved on a staggered mesh: the pressure, the density, and the level-set field are stored at the cell centers; and the velocity fields are stored at the center of the cell faces, as shown in Figure 3.11. As the SGS viscous force is proportional to the local velocity, it is reasonable to treat this force and the velocity field in the same fashion. Therefore, the SGS viscous force is added as a source term to the momentum equations in the velocity cells that are close to the wall and the liquid-gas interface. For example, we add $\frac{2\mu_f u(i,j,k)}{\Delta^2 \tan(\theta_s)} \ln\left(\frac{\Delta}{h_s}\right)$ in a u velocity cell $u(i,j,k)$ if the cell is next to the wall and is also at the interface, i.e., $G(i-1,j,k) \times G(i,j,k) < 0$, where G has been defined in the caption of Figure 3.11. The v and w velocity cells are treated in the same fashion.

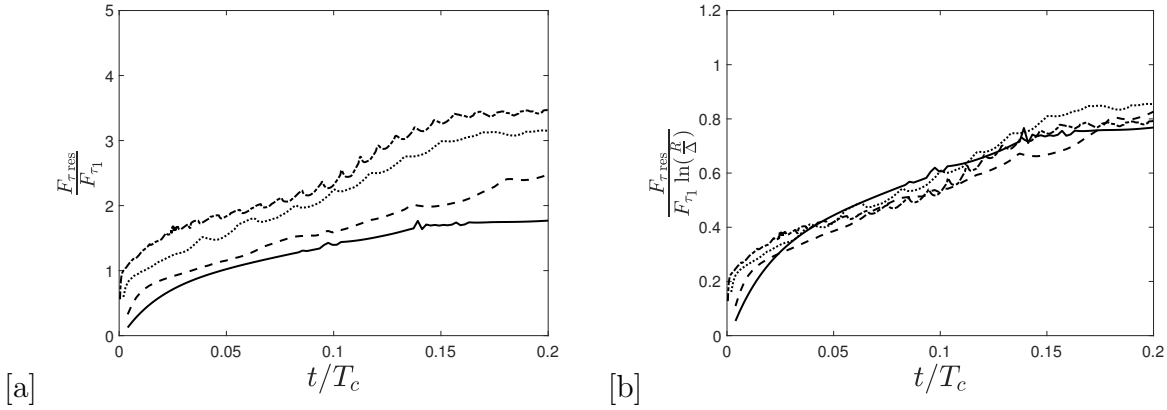

Figure 3.12: A priori test of the resolved viscous force. [a] $F_{\tau\,\mathrm{res}}$ normalized by $F_{\tau 1}$, [b] $F_{\tau\,\mathrm{res}}$ normalized by $F_{\tau 1}\ln(\frac{R}{\Delta})$. Results shown are for resolutions $R/\Delta = 9$ $(-)$, 18 $(--)$, 36 $(\cdots)$, and 72 $(-\cdot)$.

3.5 Verification and validation

3.5.1 A priori test

Before performing simulations, we first conduct a priori analysis of the proposed SGS viscous model. Simulations results are expected to be numerically mesh-independent and physically accurate with the SGS viscous model. These two properties will be assessed separately in Section 5 and the reason will be explained in this sub-section.

According to Eq 3.18, the resolved viscous force can be estimated as

$$F_{\tau\,\mathrm{res}} \sim F_{\tau 1} \ln\left(\frac{R}{\Delta}\right), \tag{3.19}$$

where $F_{\tau 1} = \frac{2\mu_f u\Delta}{\tan(\theta_s)}$. The SGS viscous force can be estimated as

$$F_{\tau\,\mathrm{SGS}} \sim F_{\tau 1} \ln\left(\frac{\Delta}{h_s}\right). \tag{3.20}$$

The estimation of the resolved viscous force can be validated using the measured

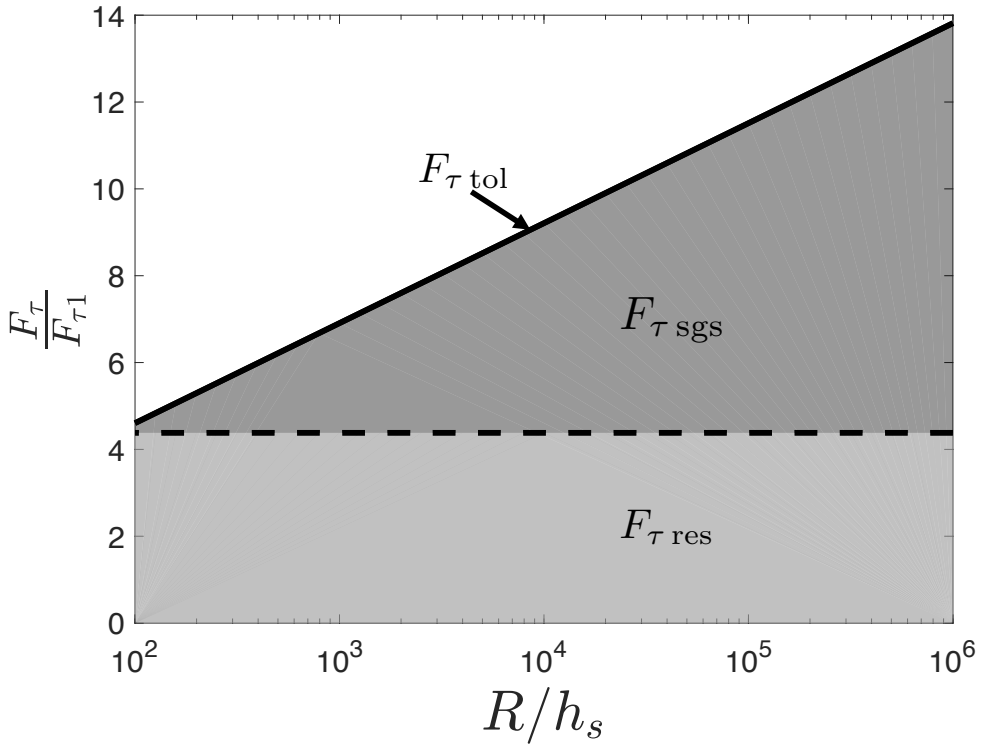

Figure 3.13: Estimation of the normalized resolved, SGS and total viscous forces. Results shown are for the normalized total viscous force $F_{\tau\,\mathrm{tol}}/F_{\tau 1}$ $(-)$. The region between the solid line $(-)$ and the dashed line $(--)$ represents the SGS viscous force $F_{\tau\,\mathrm{SGS}}$. The region under the dashed line $(--)$ represents the corresponding the resolved viscous force $F_{\tau\,\mathrm{res}}$ for $\Delta = \Delta_{\mathrm{min}}$.

viscous force from Section 3.3. As shown in Figure 3.13.b, the resolved viscous forces collapse after being scaled by $\ln(\frac{R}{\Delta})$.

The sum of the SGS viscous force and the resolved viscous force is the total viscous force

$$F_{\tau\,\mathrm{tol}} \sim F_{\tau 1} \ln\left(\frac{R}{h_s}\right), \tag{3.21}$$

whose magnitude is influenced by the choice of h_s but is independent of the mesh-size.

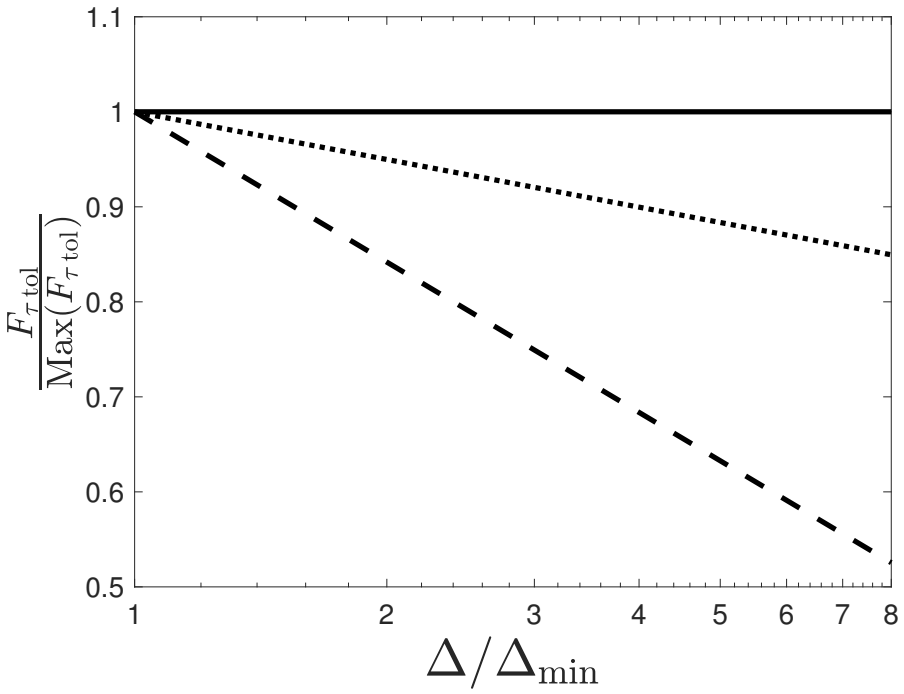

Figure 3.14: Normalized total viscous forces as a function of the mesh-size. Results shown are for $F_{\tau\,\mathrm{tol},\,c}(h_s = 1\times10^{-5}\,\mathrm{m})(--)$, $F_{\tau\,\mathrm{tol},\,c}(h_s = 1\times10^{-9}\,\mathrm{m})(\cdots)$, and the total viscous force with the mesh-dependent SGS viscous force $(-)$.

In the previous studies [3, 83] that used the Cox-Voinov type model, simulation results were less mesh-dependent with smaller cut-off lengths. This observation can be explained by the following analysis. A mesh-independent simulation requires the total viscous force to be mesh-independent. However, this force is not necessary to be physically accurate in the mesh-dependence test. Therefore, the larger cut-off length ($h_s = \Delta_{\mathrm{min}} = 1\times10^{-5}\,\mathrm{m}$) can be used in the mesh-dependence test, and actually it is more appropriate than the smaller cut-off length ($h_s = a = 1\times10^{-9}\,\mathrm{m}$). To demonstrate its advantage, we use a mesh-independent SGS viscous force

$$F_{\tau\,\mathrm{SGS},\,c} = F_{\tau 1}\ln(\frac{\Delta_{\mathrm{min}}}{h_s}), \tag{3.22}$$

for comparison. In the case with $h_s = 1\times10^{-5}\,\mathrm{m}$, the constant SGS viscous force

is chosen as

$$F_{\tau\,\mathrm{SGS},\,c} = F_{\tau 1} \ln(\frac{\Delta_{\min}}{\Delta_{\min}}) = 0. \tag{3.23}$$

In the case with $h_s = 1 \times 10^{-9}\,\mathrm{m}$, the constant SGS viscous force is chosen as

$$F_{\tau\,\mathrm{SGS},\,c} = F_{\tau 1} \ln(\frac{\Delta_{\min}}{a}) = 9.21 F_{\tau 1}. \tag{3.24}$$

These two SGS viscous forces are chosen to be close to our mesh-dependent SGS viscous forces, but are constant with respect to the mesh size. The corresponding total viscous force can be found as

$$F_{\tau\,\mathrm{tol},\,c} = F_{\tau 1} \ln(\frac{\Delta_{\min}}{h_s}) + F_{\tau 1} \ln(\frac{R}{\Delta}), \tag{3.25}$$

which is a function of the mesh size Δ. The total viscous forces, normalized by their corresponding maximum $\mathrm{Max}(F_{\tau\,\mathrm{tol},\,c}) = F_{\tau 1} \ln(\frac{R}{h_s})$, are plotted in Figure 3.14 along with our model. As shown, the total viscous force, evaluated with a constant SGS viscous force model, depends on the mesh-size Δ, and the dependence is easier to observe in the case with a larger cut-off length. To conclude, with a larger cut-off length, the discrepancy of an SGS viscous model is easier to observe in the mesh-dependency test, if the SGS viscous force does not exactly compensate the resolved viscous force to form a mesh-independent total viscous force.

However, simulations may not be physically accurate if the chosen numerical slip length is much larger than the physical slip length. For demonstration, we compare the magnitude of $F_{\tau\,\mathrm{tol}}$, $F_{\tau\,\mathrm{res}}$, and $F_{\tau\,\mathrm{SGS}}$, and plot them as a function of R/h_s in Figure 3.13, where $R = 1\,\mathrm{mm}$ is chosen as a constant. The lower limit of h_s is chosen as the physical slip-length [37], $a \sim 1 \times 10^{-9}\,\mathrm{m}$, and the upper limit of h_s is chosen as the minimum mesh-size $\Delta_{\min} = R/72 \sim 1 \times 10^{-5}\,\mathrm{m}$, which is obtained from Section 3.3. The drop radius R is $1 \times 10^{-3}\,\mathrm{m}$. As shown in Figure 3.13, $F_{\tau\,\mathrm{tol}}(h_s = 1 \times 10^{-5}\,\mathrm{m})$ is about 30% of $F_{\tau\,\mathrm{tol}}(h_s = 1 \times 10^{-9}\,\mathrm{m})$, indicating

the total viscous force is under-estimated with $h_s = 1 \times 10^{-5}\,\mathrm{m}$. Therefore, a viscosity-capillary two-phase flow simulation with an unrealistically large cut-off length should be physically inaccurate.

As a result, we first assess the numerically mesh-independence with a large cut-off length. Then a physical slip length is employed as the cut-off length to assess the physically accuracy.

3.5.2 Verification: does the SGS viscous force model lead to better mesh-independency?

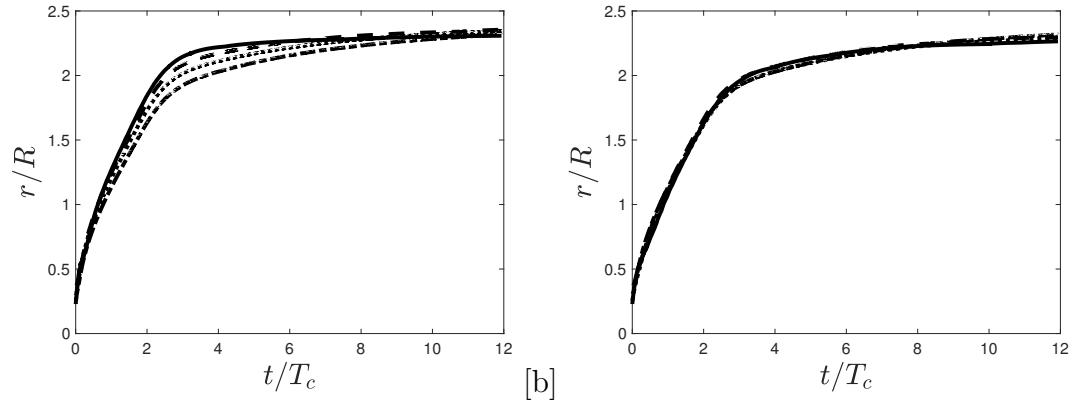

Figure 3.15: Evolution of the wetting radius r as a function of time in linear-linear scale. [a] without the SGS viscous model, [b] with the SGS viscous model. Results shown are for resolutions $R/\Delta = 9(-)$, $18(--)$, $36(\cdots)$, and $72(-\cdot)$.

We first verify the proposed SGS viscous force model in the previous 2D drop spreading problem. As demonstrated in Section 3.3, simulations of drop spreading were mesh-dependent because the resolved viscous-force was mesh-dependent. In this test, we aim to demonstrate that the simulations can be mesh-independent after adding the SGS viscous force model. The numerical setup is the same as in Section 3.3. To converge to the results obtained from the finest mesh, we test with

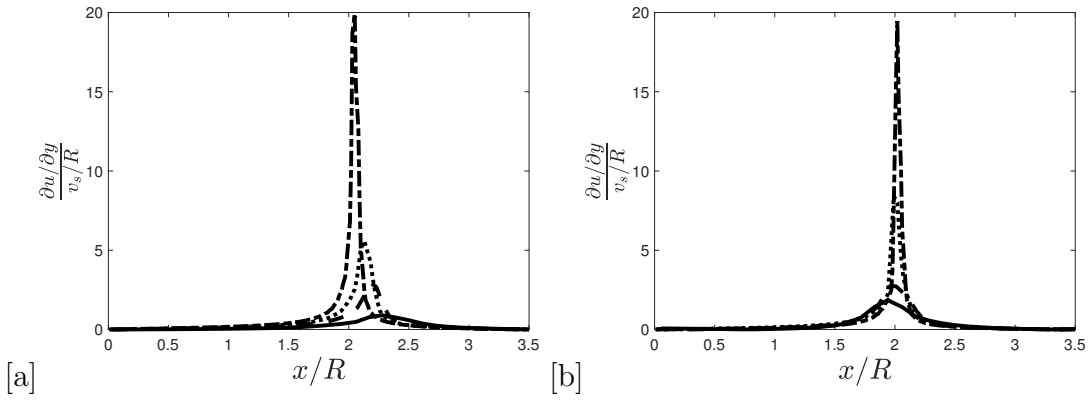

Figure 3.16: Distribution of the shear rate at the wall for 2D drop spreading at $t/T_c = 2$. [a] without the SGS viscous model, [b] with the SGS viscous model. Results shown are for resolutions $R/\Delta = 9(-)$, $18(--)$, $36(\cdots)$, and $72(-\cdot)$.

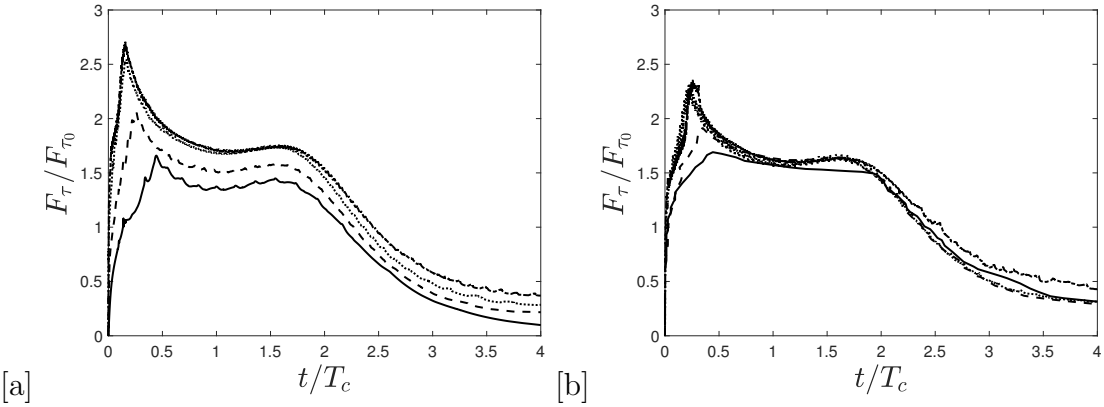

Figure 3.17: Evolution of the total viscous force on the wall for 2D drop spreading. [a] without the SGS viscous model, [b] with the SGS viscous model. Results shown are for resolutions $R/\Delta = 9(-)$, $18(--)$, $36(\cdots)$, and $72(-\cdot)$.

$h_s = \Delta_{\min}$. We evaluate simulation results using the SGS viscous force model by comparing results obtained with and without the SGS viscous force model in Figure 3.15, Figure 3.16, and Figure 3.17. In Figure 3.15, which depicts the evolution of the wetting radius, all the curves collapse to the spreading curve obtained from $\Delta = \Delta_{\min}$, which indicates that the added viscous force slows down the spreading for simulations on coarser meshes. Following previous studies [3, 50, 84], the wall

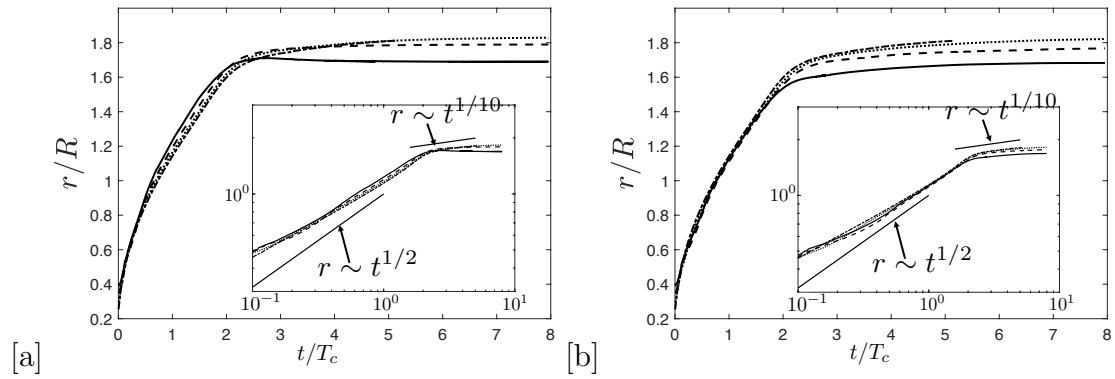

Figure 3.18: Evolution of the wetting radius r as a function of time in linear-linear scale. [a] without the SGS viscous model, [b] with the SGS viscous model. Results shown are for resolutions $R/\Delta = 9(-)$, $18(--)$, $36(\cdots)$, and $72(-\cdot)$.

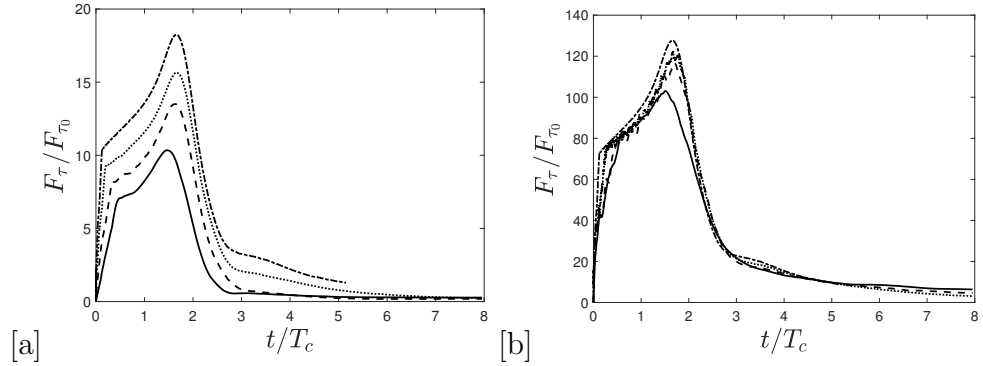

Figure 3.19: Evolution of the total viscous force on the wall for 3D drop spreading case. [a] without the SGS viscous model, [b] with the SGS viscous model. Results shown are for resolutions $R/\Delta = 9(-)$, $18(--)$, $36(\cdots)$, and $72(-\cdot)$.

shear-rate around the contact line is shown in Figure 3.16. As expected, the peaks are better collocated with the SGS viscous force model. The peak of the shear rate is lower on a coarser mesh, because of it is averaged over the control volume, but the total viscous force on the wall is not significantly impacted, as shown in Figure 3.17. In summary, better mesh-independence has been achieved with the SGS viscous force model in the 2D drop spreading problem. Simulation results for the 3D version of this case are also presented in Figure 3.18 and Figure 3.19.

Apart from better mesh-independence, we note that the simulation captures the inertial spreading law, i.e., $r \sim t^{1/2}$, without the SGS viscous force model. The viscous spreading law, i.e., $r \sim t^{1/10}$, is also captured after adding the SGS viscous force modeling.

3.5.3 Validation: drop spreading on a flat plane

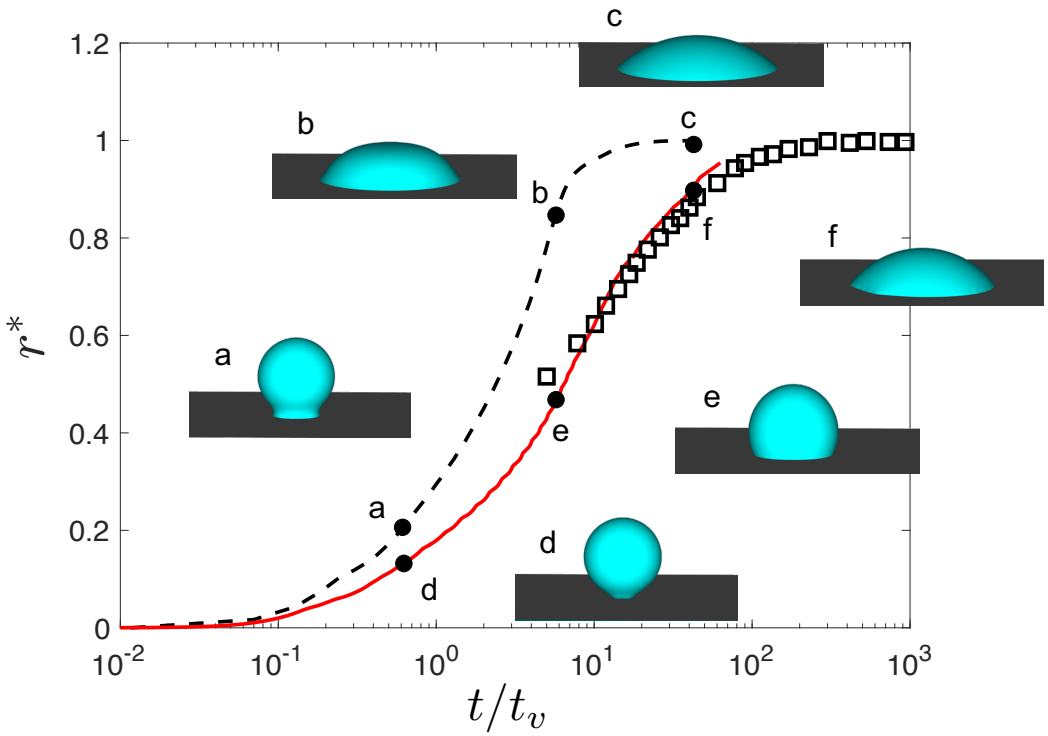

Figure 3.20: Comparison with the experiments. Results shown are for simulations without the SGS viscous model (−−), with SGS viscous model (−), and experiments by Lavi and Marmur [48](□). The drop shapes at different time are draw for direct comparison.

In the previous section, we verified that simulations can be mesh-independent using a large cut-off length. However, those simulation results are expected to be

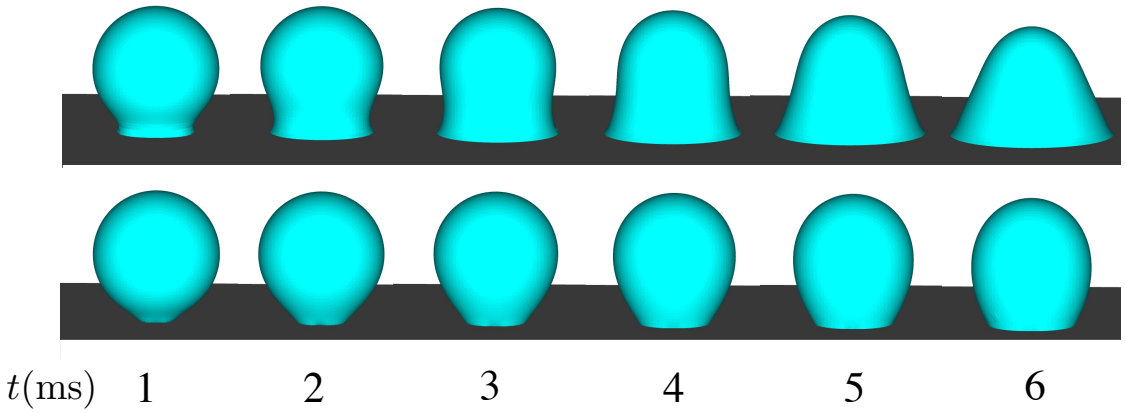

Figure 3.21: Evolution of the drop shape at the beginning of spontaneous spreading. The upper simulations are without the SGS viscous model, the lower images are with the SGS viscous model .

physically inaccurate, because the total viscous force is under-estimated. To test physical accuracy, we set the cut-off length as the physical slip length $a = 1\,\text{nm}$, which is suggested by Gennes et al. [37]. The simulation results are compared with the experimental results of Lavi and Marmur [48]. This test is performed in 3D, and the physical parameters are kept same as in Section 3.3. One resolution is tested, that is, $R/\Delta = 36$. For comparison, we measure the wetting radius over time from simulations with and without the SGS viscous force and compare with the experimental data in Figure 3.20. Following the experiment, we report the non-dimensional wetting radius $r^* = (r-R)/(r_f-R)$, where r_f is the equilibrium radius of the drop, with respect to the non-dimensional time t/t_v, where $t_v = \rho_l R^2/\mu_l$. The spreading duration is under-predicted without the SGS viscous force model, and the simulation with the SGS viscous force model shows good agreement with the experimental measurement of Lavi and Marmur [48]. In Figure 3.21, we show the evolution of the drop shape at the beginning of spontaneous spreading. In the simulation without the SGS viscous force model, the dynamic contact angle

quickly adapts to the imposed contact angle. This adaptation is postponed in the simulation that uses the SGS viscous force model. The drop spreads faster in the simulation without the SGS viscous force model, because the viscous force is underestimated.

3.5.4 Validation: drop sliding down an inclined plane

In order to test the model in a non-axi-symmetrical problem, we perform simulations of drop sliding down an inclined plane and compare results with the experimental data of Le Grand et al. [49].

The simulations are performed in a numerical domain of $3\,\text{mm} \times 6\,\text{mm} \times 3\,\text{mm}$ on an uniform $32 \times 64 \times 32$ mesh. We use x as the plane normal direction, y as the direction of sliding along the plane and z as the lateral direction. To save computational cost, Case 47V10 from Le Grand et al. [49] is chosen for comparison, because simulations can run with a larger time-step due to the lower liquid viscosity of this case. The physical parameters are collected in Table 3.1. The corresponding drop radius to cell-size ratio is 12.0.

Drop radius	a	$1.127\,\text{mm}$
Gas density	ρ_g	$1\,\text{kg/m}^3$
Liquid density	ρ_l	$936\,\text{kg/m}^3$
Gas viscosity	μ_g	$10^{-5}\,\text{kg/(s}\cdot\text{m)}$
Liquid viscosity	μ_l	$0.01\,\text{kg/(s}\cdot\text{m)}$
Surface tension	σ	$0.0201\,\text{N/m}$
Advancing contact angle	θ_a	50°
Receding contact angle	θ_r	45°
Gravity	g	$9.8\,\text{m/s}^2$

Table 3.1: Parameters for simulations of a drop sliding down an inclinded plane.

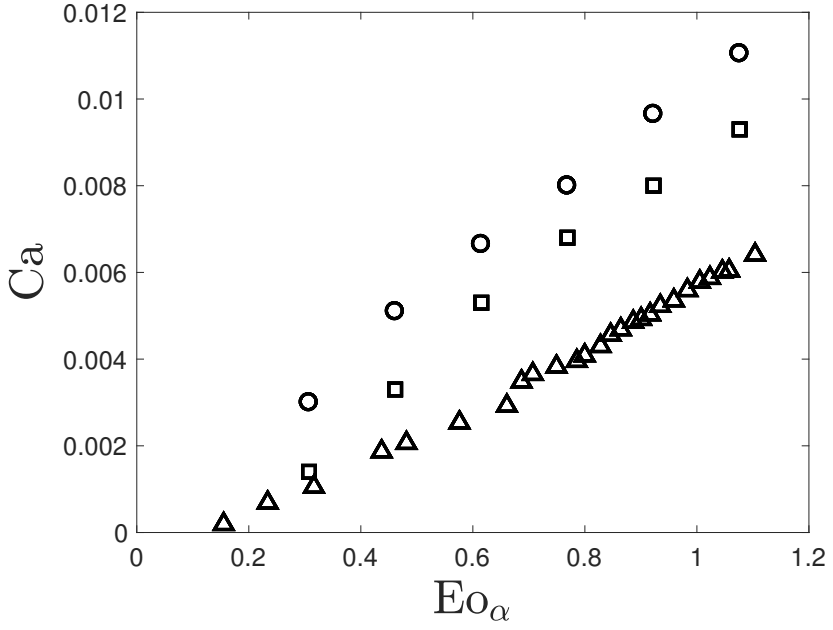

Figure 3.22: Non-dimensional steady velocity of the drops as a function of plane inclination. Results shown are for simulations without contact angle hysteresis (◯), with contact angle hysteresis (□), and experimental results of Le Grand et al. [49](△).

The drop is initialized as a spherical cap of radius $R_0 = a(4/(2 - \cos(\theta_s) + \cos^3(\theta_s)))^{\frac{1}{3}}$ on the plane. We change the plane inclination α as a control parameter to change gravity parallel to the plane. As reported in the experiment, the drop first slides down and then reaches a steady velocity u, due to balance of the gravitational force, the surface tension force, and the viscous drag from the plane. The steady velocity are non-dimensionalized as the capillary number, $\mathrm{Ca} = \mu_l u/\sigma$. $\mathrm{Eo}_\alpha = \mathrm{Eo}\sin(\alpha) = V^{2/3}(\rho g/\sigma)\sin\alpha$ is an effective Eötvös number based on the component of gravity parallel to the plane, where $V = 4\pi a^3/3$ is the volume of the drop.

Two series of simulations are performed: one uses a single contact angle $\theta_s = 48°$; the other includes contact angle hysteresis, namely the advancing contact angle is larger than the receding contact angle. Because we focus on the dynamics

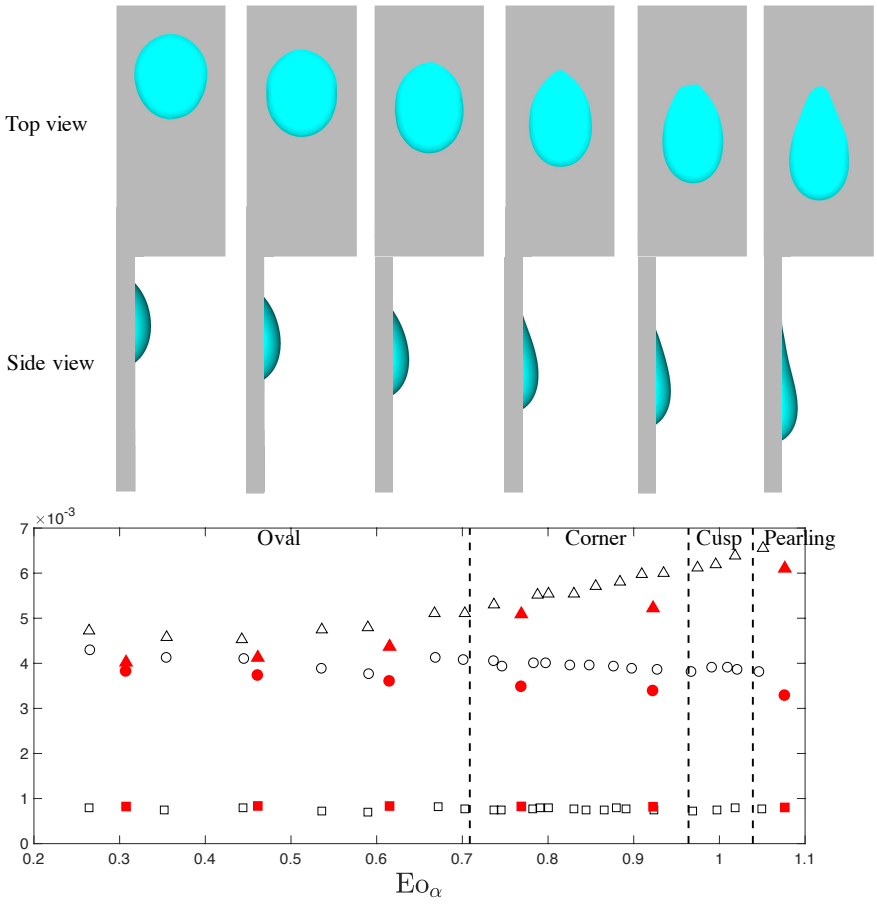

Figure 3.23: Evolution of the drop shape as a function of plane inclination: height (▲), width(■) , and length (●) from simulation; height (□), width (◯), and length(△) from experiment.

of the drop, the drop is assumed to move on the plane. Therefore, the contact angle hysteresis is implemented as

$$\theta = \begin{cases} \theta_a & \text{if } \mathbf{u}_c \cdot \mathbf{n}_\Gamma \geqslant 0, \\ \theta_r & \text{if } \mathbf{u}_c \cdot \mathbf{n}_\Gamma < 0, \end{cases} \tag{3.26}$$

where $\mathbf{u}_c$ is the velocity at the scalar cell center. To study onset motion of a drop on an inclined plane, we suggest the prediction-correction strategy proposed by Maglio and Legendre [58].

As shown in Figure 3.22, the non-dimensional steady velocity of the drops are

compared against the experimental results of Le Grand et al. [49]. The predicted steady velocities are systematically lower in the simulations that include contact angle hysteresis, and are closer to the experimental results. But the simulations including contact angle hysteresis still over-predict the steady velocity. The agreement can be improved by increasing the SGS viscous force, but we opt to avoid testing this idea before figuring out the physical explanation.

The length, width and height of the drop have been measured for many inclinations, and are compared with the experimental data in Figure 3.23, along with top view and side view of the steady drop. The height of the drop is well predicted by our simulations, but both the width and the length are under-predicted. We note that the uncertainty from the experimental measurement can not be ignored in this comparison. The under-estimation of the width and the length of the drop are possibly due to the uncertainty in the reported contact angle of the experiment. Because both of the width and the length of simulated drop are larger if the contact angle in the experiment is actually smaller than the reported value. The under-reported contact angle can also lead to a under-estimated SGS viscous force, which will cause the steady velocity to be over-predicted. One clear discrepancy of the simulation is that the receding contact angle can be smaller than the critical receding angle 20° in the experiment. The cusp and pearling flow pattern in the experiment are related to the critical receding contact angle, which is not the exact same in the simulation. The difference in the critical receding angle can also contribute to difference in the shape of steady drops, then influencing their steady velocities.

We conclude that the current numerical approach is able to reproduce the motion and shape of drop sliding down a plane. However, these results are sensitive

to the SGS viscous force, contact angle hysteresis, and the critical receding contact angle. Future careful validation with the experiment and other simulations [58, 82] that use the Cox-Voinov models are required to elucidate the detailed physics.

3.6 Conclusion

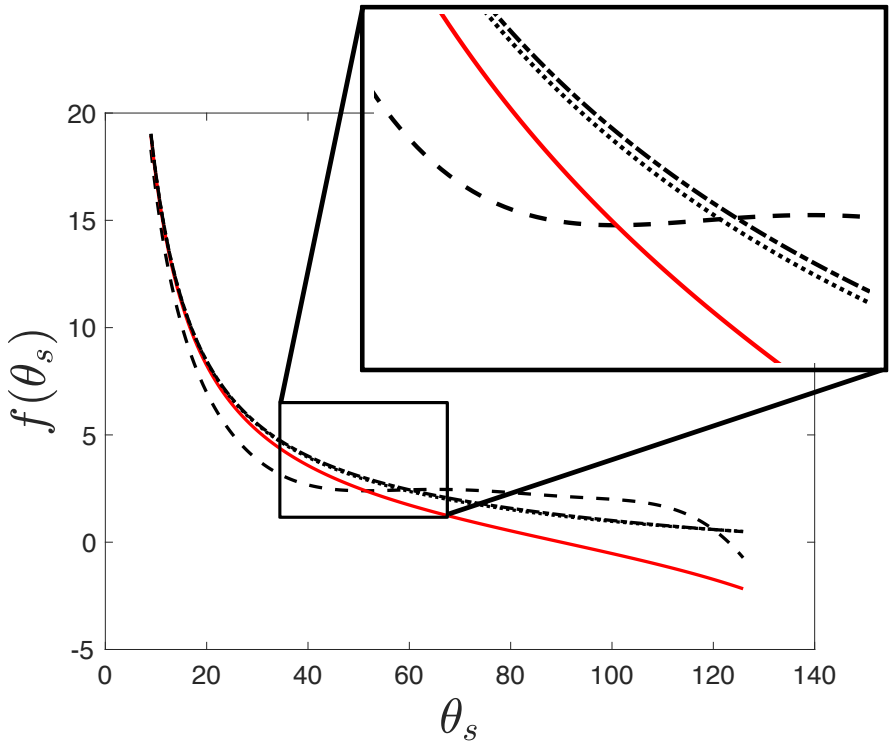

Figure 3.24: Comparison of various viscous force models. Results shown are for the simple flow model Eq 3.10(−), the simple flow model with a correction factor for large contact angles [80](· · ·), the Cox-Voinov theory Eq 3.15(· · ·), and the Stokes flow solution of Zhang and Mohseni(−−).

In this chapter, we provided a simple flow model to estimate the viscous force at the contact line. The strength of the viscous force is affected by the liquid dynamic viscosity, the contact angle, and the length scale where the measurement is performed. The viscous force model was analytically proved to be equivalent to

the viscous part of the Cox-Voinov theory when the contact angle is small. A scale-dependent modeling strategy, see in Section 3.7.2, was proposed to combine the hydrodynamic theory and MKT, which requires more justification in the future.

To simulate two-phase flows with moving contact lines, we first derived a volume-averaged Navier-Stokes equations for two-phase flow with contact lines, and identified two unclosed terms: an SGS surface tension force and an SGS viscous force. The SGS surface tension force can be closed by the uncompensated Young's force model. We demonstrated that the total viscous force on the wall is mesh-dependent without an SGS viscous force model. The SGS viscous force was then closed by a physics-based viscous force model, resulting mesh-independence in the context of spontaneous drop spreading. In problems like drop spreading on a plane and drop sliding down an inclined plane, the simulation results achieved good agreement with their experimental counterpart after applying the SGS viscous force model.

The viscous force model can be improved by multiplying the correction factor from Snoeijer [80], or by integrating the viscous force from a Stokes solution to the moving contact line [104]. All of these models can be presented in the same form $f(\theta)\mu u_0 \ln\left(\frac{l_m}{l_s}\right)$, where $f(\theta)$ is a function related to the contact angle θ. We show them in Figure 3.24 with the Cox-Voinov theory Eq 3.15, and our simple flow model given by Eq 3.10. At small contact angles, these models generally agree with each other; at large contact angles, these models start to diverge, indicating that future studies need to be performed to investigate the viscous force at large contact angles, especially in the hydrophobic regime.

Further studies on drop sliding down an inclined plane, including validation with the experiment and comparison with other simulations [58, 82], are useful for

us to elucidate the detailed physics. As both the SGS surface tension force and the SGS viscous force model are ready for problems with curved surfaces and moving surfaces, they can be easily applied in large-scale simulations of two-phase flows in complex geometries.

3.7 Appendix

3.7.1 Appendix A: Mass-spring-damper system modeling of drop spreading

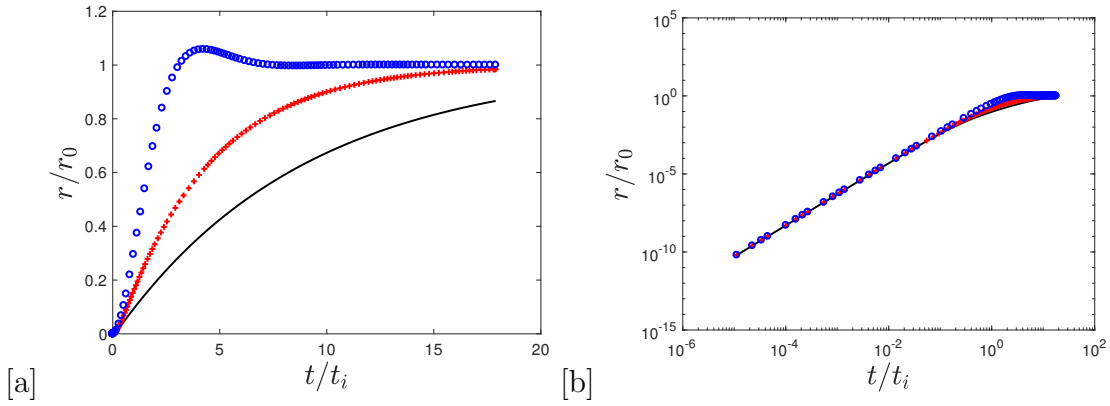

Figure 3.25: Evolution of the wetting radius. [a] Linear-linear plot, [b] Log-log plot. Results shown are for resolutions $\beta = 3$ (◯), 10 (+), and 20 (−).

Spontaneous drop spreading can be modeled using a mass-spring-damper system [59, 55]. Here we provide a simplified version with focus on illustrating that the spreading dynamics is independent of the viscous force in the inertia-capillary regime. The differential equation that describes the evolution of the wetting radius of a spreading drop is given by

$$m\frac{\partial^2 r}{\partial t^2} + \beta\frac{\partial r}{\partial t} + k(r - r_0) = 0, \tag{3.27}$$

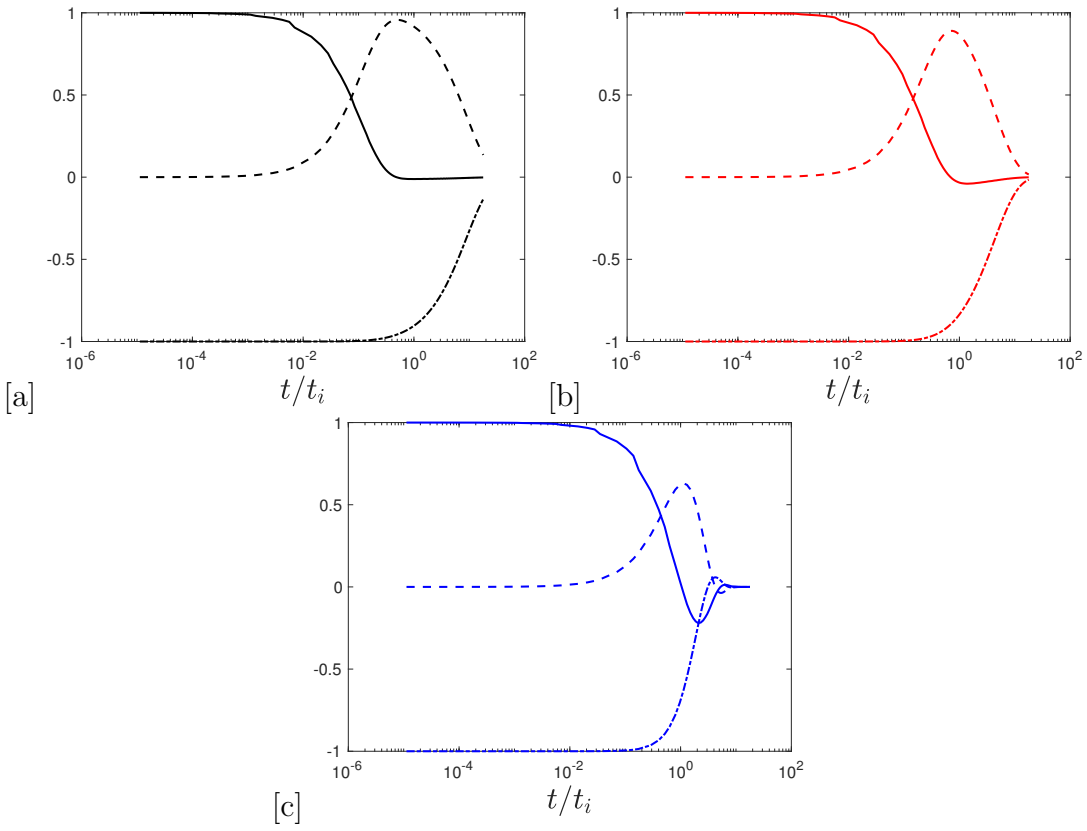

Figure 3.26: Evolution of the normalized forces during drop spreading. [a] $\beta = 20$, [b] $\beta = 10$, [c] $\beta = 3$. Results shown are for normalized inertia force $m\frac{\partial^2 r}{\partial t^2}/(kr_0)$ $(-)$, normalized viscous force $\beta\frac{\partial r}{\partial t}/(kr_0)$ $(--)$, and normalized surface tension force $k(r-r_0)/(kr_0)$ $(-\cdot)$.

where m is the mass, which is proportional to the inertia of the droplet; β is the friction coefficient, which is related to the viscous force during the spreading; k is the spring constant, which is related to the surface tension coefficient; r_0 is the equilibrium position.

During the test, we set $m = 5$, $k = 1$, $r_0 = 10$. To mimic mesh-dependent viscous forces, three friction coefficient are chosen: $\beta = 3$, 10, and 20. The evolution of the wetting radius is shown in a linear-linear plot in Figure 3.25.a and in a log-log plot in Figure 3.25.b. As shown in the log-log plot, the evolution of the wetting radius is clear to be independent of the viscous force at the begin-

ning of the spreading. The evolution of the normalized inertia force $m\frac{\partial^2 r}{\partial t^2}/(kr_0)$, the normalized viscous force $\beta\frac{\partial r}{\partial t}/(kr_0)$, and the normalized surface tension force $k(r-r_0)/(kr_0)$ are shown in Figure 3.26 for each test cases. The inertia force and the surface tension force dominate at the beginning of the spreading. This regime is commonly named as the inertia-capillary regime. Therefore, the evolution of the wetting radius is independent of the viscous force in the inertia-capillary regime, and the evolution of the wetting radius is highly influenced by the viscous force in the viscosity-capillary regime, as shown in Figure 3.25.a.

3.7.2 Appendix B: Multi-scale modeling of moving contact lines

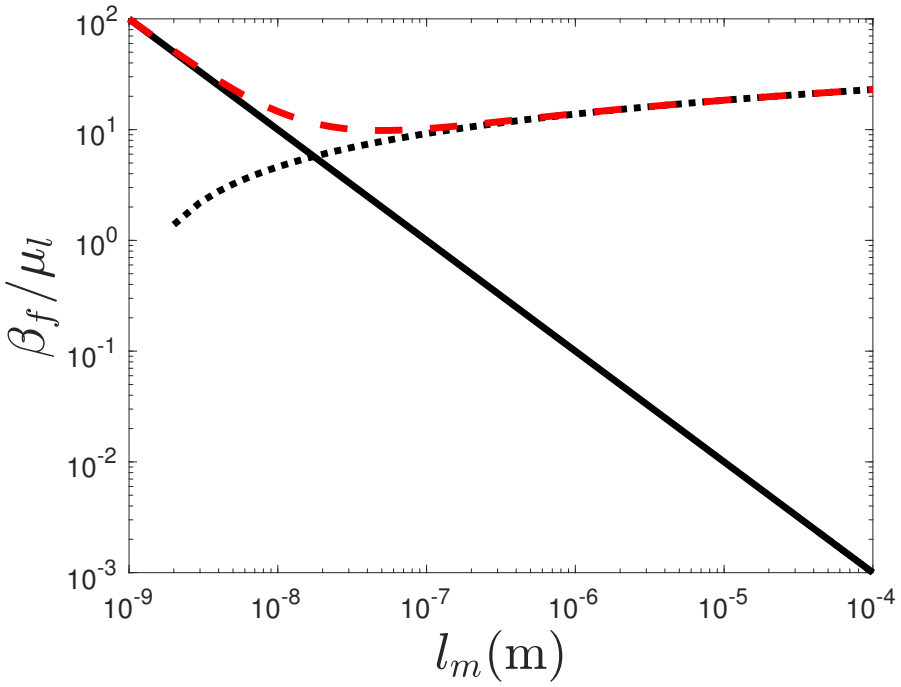

Figure 3.27: Effective friction coefficient as a function of the distance to the contact line. Results shown are for the $\beta_s\frac{l_s}{l_m}(-)$, $\frac{2\mu_l}{\tan(\theta_s)}\ln\left(\frac{l_m}{l_s}\right)(\cdot\cdot\cdot)$, and their sum $\beta_f(--)$

Many previous studies [10, 74] have proposed multi-scale modeling strategies to link the molecular scale and the continuum scale for contact line modeling. However, the scale-dependent property of the moving contact line, as shown in Eq 3.11, is ignored during the integration of the molecular force, resulting in over-estimated molecular force at the continuum scale. Recent Molecular Dynamic (MD) simulations [74, 56] have shown that the molecular force is concentrated about l_s around the contact line, and showed good agreement with the Blake theory [7],

$$\cos(\theta_d) = \cos(\theta_s) - \frac{2k_{\mathrm{B}}T}{\sigma\lambda^2}\sinh^{-1}\left(\frac{u_0}{2k_{\mathrm{w}}\lambda}\right) \tag{3.28}$$

where k_B is the Boltzmann constant, T is the absolute temperature, k_{w} is the equilibrium frequency of the random molecular displacements at the contact line, and λ is the average distance between adsorption sites on the substrate on which the random molecular displacements occur. When the contact line speed is small, the formula can be approximated by

$$\cos(\theta_d) = \cos(\theta_s) - \frac{k_{\mathrm{B}}T}{\sigma k_{\mathrm{w}}\lambda^3}u_0 \tag{3.29}$$

Note that this formula has only been validated at the nano-scale [74, 56]. Extrapolation this formula over-estimates the molecular force. Duvivier et al. [35] extracted the effective friction factor at nano-scale, $\beta_s \sim 100\mu_f$, from various MD simulations. Although the factor 100 varies for different two-phase flows, the order of the magnitude does not change, thus we use it here for estimation.

To add the friction force caused by the molecular interactions that has been

introduced in [7, 35, 74], we re-integrate the viscous force as depicted in Figure 3.5,

$$F_\tau = \int_0^{l_z}\int_0^{l_s} \tau_w dxdz + \int_0^{l_z}\int_{l_s}^{l_m} \tau_w dxdz \tag{3.30}$$

$$= \beta_s \frac{l_s}{l_m} l_z + \frac{2\mu_l u_0 l_z}{\tan(\theta)} \ln\left(\frac{l_m}{l_s}\right). \tag{3.31}$$

Then the macroscopic friction factor is estimated as

$$\beta_f = \beta_s \frac{l_s}{l_m} + \frac{2\mu_l}{\tan(\theta_s)} \ln\left(\frac{l_m}{l_s}\right), \tag{3.32}$$

where the first term comes from the molecular force and the second term comes from the hydrodynamics force. As shown on Figure 3.27, the molecular force dominates contact line motions at several nanometers. At large scales ($l_m > 100\,\text{nm}$), the hydrodynamic force dominates contact line motions, and the friction contribution from the molecular force is negligible. Since we focus on simulating large-scale simulations in this work, the molecular force can be ignored.

CHAPTER 4

DROP FIBER INTERACTION

4.1 Introduction

Two-phase flows with moving contact lines are ubiquitous in many natural and industrial applications. These applications include ink-jet printing, internal combustion engines [99], micro-fluidics applications [23], and two-phase flows in porous media [107], to name a few. In this chapter, we numerically study two-phase flows in a common piece of industrial equipment, namely a coalescer.

Coalescers are filters made from fibrous materials that collect fine droplets dispersed in a continuous phase. In industry, fiber-based coalescers are used to separate two immiscible fluids. For example, coalescers are used to recover liquid water from morning fog in desert areas, and they can be employed to mitigate noxious aerosol emissions from chemical plants. However, if the concentration of liquid within a coalescer becomes too large, the coalescer becomes saturated and the gas stream can re-atomize the coalesced liquid into small droplets. To mitigate saturation and optimize the performance of a liquid-gas coalescer, a detailed understanding of the multiphase flow inside coalescers is necessary. Unfortunately, direct experimental observation is not easy to achieve inside a coalescer, because fibers are not made of transparent materials, and they are irregularly arranged.

To better describe several drops passing by a single fiber, we divide the process into three conceptual stages: capture, accumulation, and detachment. Here, capture occurs when droplets hit a fiber and stay on form larger droplets, and detachment occurs when captured droplets leave a fiber. In this chapter, we nu-

merically study drop impact and detachment processes to provide some insight into the fundamental physics which can be used in future design.

4.2 Drop impact on a fiber

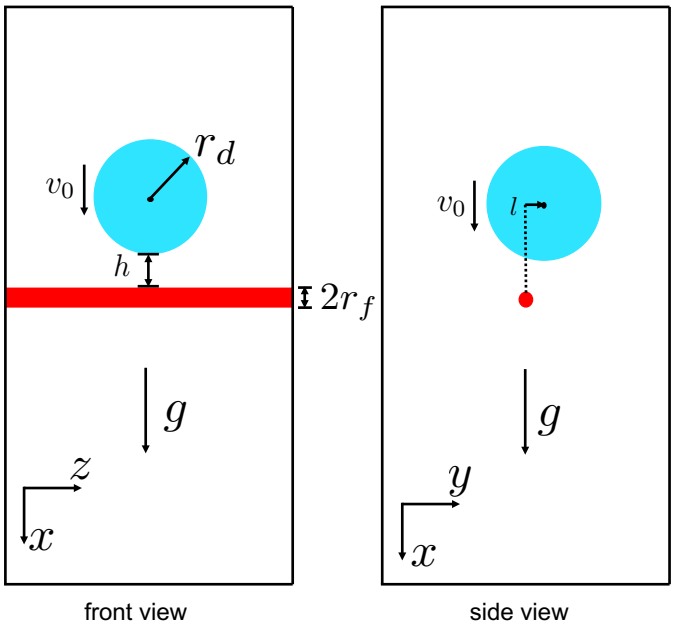

Figure 4.1: Numerical setup for a drop impact on a fiber.

Having detailed knowledge of the outcome of drop impact on a fiber provides critical support for engineers seeking to design and optimize the performance of fibrous material. Many experimental and theoretical studies in this area have been performed. For example, Lorenceau et al. [54] investigated what happens when a silicon oil drop comes to contact with a horizontal fiber and quantified the threshold velocity of capture. Comtet et al. [19] and Dressaire et al. [33] studied the dynamics of a single drop falling on a thin flexible fiber. Recently, Kim and Kim [47] studied drop impact on a fiber with higher impact velocity and provided regime diagrams for predicting impact outcomes. Such numerical studies of drop

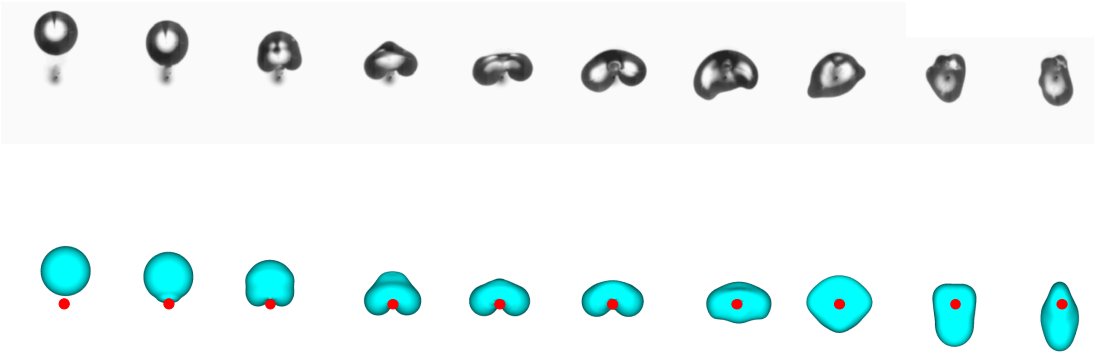

Figure 4.2: Drop impact on a fiber at low velocity, $v_0 = 0.3\,\mathrm{m/s}$, and $r_f = 250\,\mu\mathrm{m}$. The time interval between two successive pictures is $\Delta t = 2\,\mathrm{ms}$.The upper images are experimental results from Kim and Kim [47]. The lower images are from the simulation.

fiber interaction are, however, very rare. Here we provide numerical studies of drop impact on a fiber to provide qualitative and quantitative comparisons with experimental counterparts [47].

4.2.1 Validation

We use the setup shown in Figure 4.1 for all the simulations reported in this section. A cylindrical fiber with radius r_f is aligned in the z-directions, and placed in the middle of the domain in the x and y-direction. A drop with radius r_d is placed slightly above the fiber with a height h. This height h is set below its value in the experiments [47] to save simulation time. A shift of center l is observed in the experiment, which is identified as the source of the unsymmetrical behavior of the drop. However, measurement of the shift is not provided, so we set l at 0 in all the

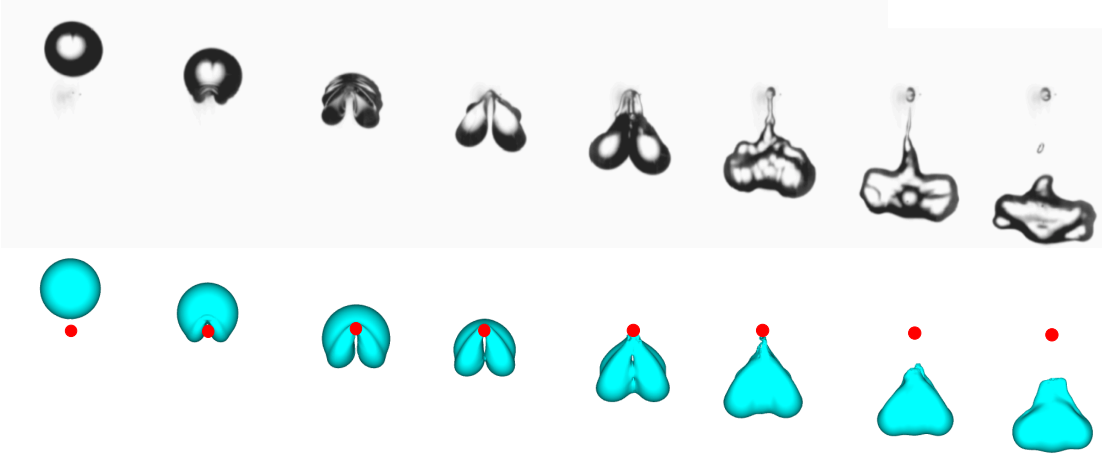

Figure 4.3: Drop impact on a fiber at moderate velocity, $v_0 = 1.3\,\mathrm{m/s}$, and $r_f = 150\,\mu\mathrm{m}$. The time interval between two successive pictures is $\Delta t = 0.5\,\mathrm{ms}$.The upper images are experimental results from Kim and Kim [47]. The lower images are from the simulation.

simulations. The gravitational acceleration points in the direction of the positive x-axis. The initial velocity of the drop is v_0. Our simulations are performed on a uniform $400 \times 200 \times 200$ mesh. The numerical domain is periodic in the y- and z-directions. Note that the domain size in y- and z- directions is at least 12 times the drop radius for all the simulations to ensure domain independence. We resolve the fiber with at least 8 numerical cells. Some simulation parameters remain constant and are summarized in Table 4.5. The grid size is $\Delta x = \Delta y = \Delta z = 40\,\mu\mathrm{m}$. The corresponding drop-radius to cell-size ratio is $r_d/\Delta x = 33.75$.

Following the experimental study [47], we first conduct three simulations of drop impact on fiber with increasing drop velocities. The equilibrium contact angle is set at $\theta_e = 86°$.

In the first case, the initial velocity of the drop is $v_0 = 0.3\,\mathrm{m/s}$, and the fiber radius is $r = 250\,\mu\mathrm{m}$. The corresponding Weber number is calculated as We =

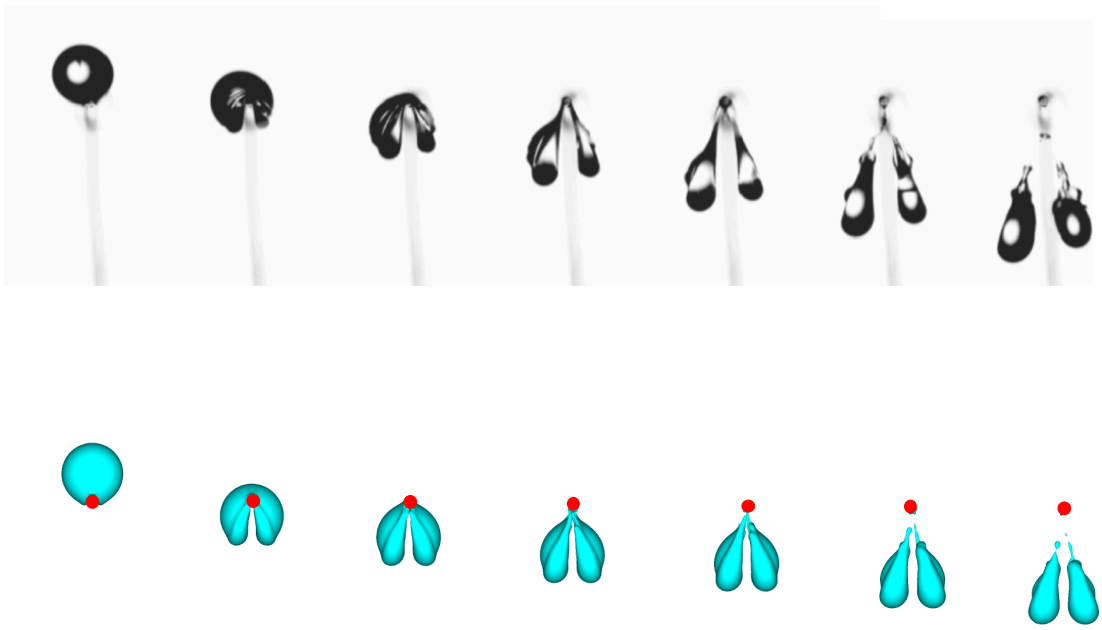

Figure 4.4: Drop impact on a fiber at high velocity, $v_0 = 2.4\,\mathrm{m/s}$, and $r_f = 150\,\mu\mathrm{m}$. The time interval between two successive pictures is $\Delta t = 0.25\,\mathrm{ms}$. The upper images are experimental results from Kim and Kim [47]. The lower images are from the simulation.

Gas density	ρ_g	$1\,\mathrm{kg/m^3}$
Liquid density	ρ_l	$1000\,\mathrm{kg/m^3}$
Gas viscosity	μ_g	$1 \times 10^{-5}\,\mathrm{kg/(s \cdot m)}$
Liquid viscosity	μ_l	$1 \times 10^{-3}\,\mathrm{kg/(s \cdot m)}$
Surface tension coefficient	σ	$0.072\,\mathrm{N/m}$
Gravitational acceleration	g	$9.8\,\mathrm{m/s^2}$
Drop radius	r_d	$1.35\,\mathrm{mm}$

Table 4.1: Parameters for simulations of a water drop impact on a fiber.

$\frac{\rho v^2 r_d}{\sigma} = 3.3$. As shown in Figure 4.2, the drop is first separated and then remerges on the surface of the fiber. In the end, the drop stays on the fiber.

In the second case, the drop is given a slightly higher initial velocity, $v_0 = 1.3\,\mathrm{m/s}$. Following the experimental setup, the corresponding fiber radius is $r =$

250 μm, and the Weber number is 62.5. Shown in Figure 4.3, the drop impacts on the fiber, first separating and then remerging below the fiber. It detaches from the fiber and falls as a single drop.

In the third case, the initial velocity of the drop is $v_0 = 1.3\,\mathrm{m/s}$, and the fiber radius is $r = 250\,\mu$m. The corresponding Weber number is 213. As seen in Figure 4.4, the drop is separated and never remerges. It detaches from the fiber and forms two separate drops.

The snapshots are taken at the same time as the experimental images. Excellent agreement has been achieved in the evolution of the topology for all three cases.

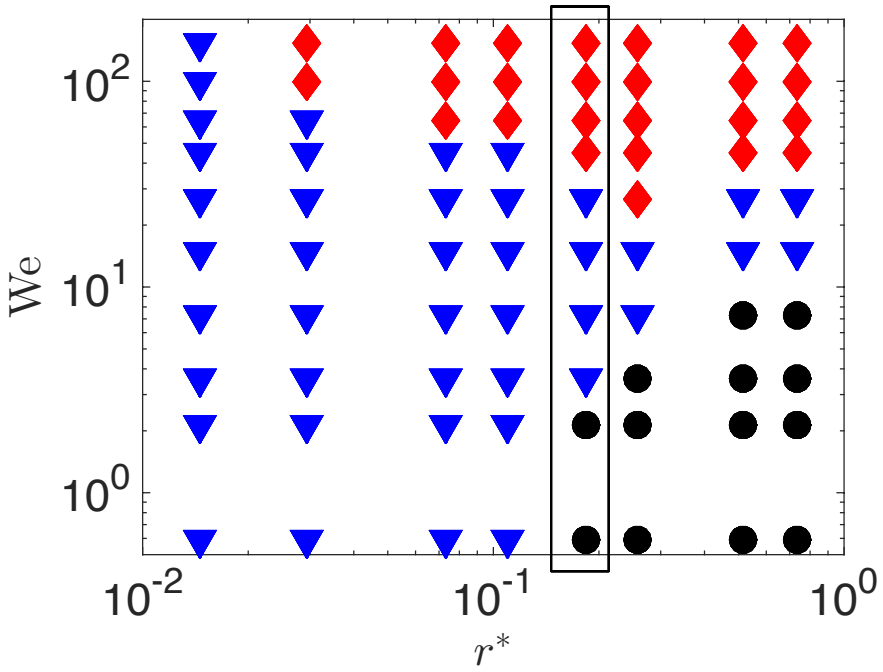

Figure 4.5: Outcomes of drop impact on a fiber with various Weber numbers, We, and fiber to drop-radius ratios, r^*. Splitting is indicated by ♦, single-drop falling is indicated by ▼, capturing is indicated by •. The figure is adapted with permission from Kim and Kim [47] (2016, Fig. 4).

We then perform a series of simulations to narrow down the gap in the Weber

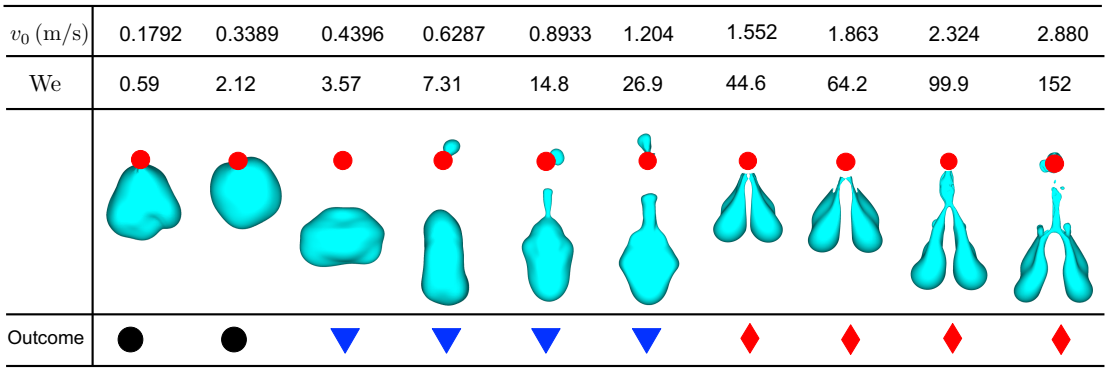

Figure 4.6: Simulated outcomes of drop impact on a fiber with increasing Weber number.

number. These simulations have the same drop-to-fiber diameter ratio and initial velocities as in the experiment. Kim and Kim [47] classified the outcomes of drop impact on a fiber into three categories: capturing (Figure 4.2), single-drop falling (Figure 4.3), and splitting (Figure 4.4). Regime diagrams are also provided to classify drop impact on a fiber with various Weber numbers and fiber-to-drop radius ratios, $r^* = r_f/r_d$. We validate the numerical simulations by directly comparing them with the results on the regime diagrams. Simulations with small r^* are computationally expensive, because of the resolution requirement to resolve the fiber. Therefore, for comparison we choose a moderate fiber-to-drop radius ratio, $r^* = 0.18$, which is circled in Figure 4.5. The equilibrium contact angle is kept at 86°. Simulation results are shown in Figure 4.6 with increasing the initial velocity. The fiber captures the first two drops. The third through the sixth drops fall as a single drop. The last four drops are split by the fiber. Our simulations seem to correctly predict the outcome of drop impact on a fiber.

4.2.2 Fiber wettability effect

Fiber wettability also has a role in the outcome of drop impact on a fiber. To demonstration these effects, we choose a case that has the same Weber number and fiber-to-drop size ratio, but different wettabilities. The fiber radius is given as $r_f = 100\,\mu$m. Drop initial velocity is $v_0 = 1.0\,$m/s. We compare the outcomes between a hydrophilic case, $\theta_e = 58°$, and a hydrophobic case, $\theta_e = 114°$. In Figure 4.7, the snapshots are taken at the same time intervals. The equilibrium contact angle is 65° in the upper images, while the contact angle is 114° in the lower images. Although both of the outcomes are single-drop falling, the drop remerges on the fiber in the hydrophilic case, whereas the drop remerges after it detaches from the fiber in the hydrophilic case.

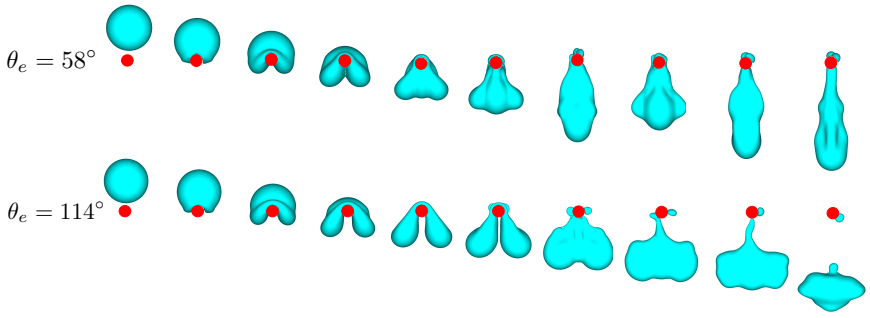

Figure 4.7: Drop impact on a fiber with varying wettabilities. $\theta_e = 58°$ in the upper images. $\theta_e = 114°$ in the lower images. The time interval between two successive pictures is $\Delta t = 0.5\,$ms.

4.3 Drop detachment from a fiber: detachment mechanisms

Another fundamental problem in understanding coalescers is determining how large of a drop can attach to and remain on a fiber. Droplet detachment can be caused by gravity or shear from the cross-flow overcoming the adhesion between the drop and the fiber. In this section, droplet detachment from a cylindrical horizontal fiber is considered, and the impact of gravitational acceleration, contact angle, and cross-flow are studied in isolation. The three mechanisms are named as gravity-driven detachment, surface tension-driven detachment, and cross-flow-driven detachment for the sake of discussion. The proposed numerical approach is first validated for gravity-driven and surface tension-driven cases, since experimental studies have been reported for these two test cases, and then we perform an exploratory study for cross-flow-driven detachment. Note that Sahu et al. [78] performed an experimental study of drop-detachment in cross-flow, and described different types of breakup of drops on a fiber. Our simulations focus on the study of the minimum cross-flow velocity for a drop to detach from a fiber, which falls into the balloon-like break-up regime in Sahu et al. [78].

4.3.1 Critical size of a drop on a hydrophilic horizontal fiber under gravity

Lorenceau et al. [54] studied the critical size of a drop on a hydrophilic horizontal fiber experimentally and analytically. In their experiments, drops were gently added to a copper fiber until detachment. Although many liquid materials were

used in the experiment, it was reported that all contact angles were small. They concluded that the critical size of a drop on a fiber is related to its fluid property, i.e., capillary length, and fiber radius, which can be expressed as

$$R_c = \begin{cases} 1.65\kappa^{-1} & R_f > \kappa^{-1} \\ 1.53 R_f^{1/3} \kappa^{-2/3} & R_f < \kappa^{-1} \end{cases} \tag{4.1}$$

where R_f is the radius of the fiber, R_c is the critical radius of the drop at which detachment occurs, and κ^{-1} is the capillary length of the drop, which is defined as $\kappa^{-1} = \sqrt{\frac{\sigma}{\rho_l g}}$.

Gas density	ρ_g	$1\,\mathrm{kg/m^3}$
Liquid density	ρ_l	$971\,\mathrm{kg/m^3}$
Gas viscosity	μ_g	$1 \times 10^{-5}\,\mathrm{kg/(s \cdot m)}$
Liquid viscosity	μ_l	$1 \times 10^{-3}\,\mathrm{kg/(s \cdot m)}$
Surface tension	σ	$0.0214\,\mathrm{N/m}$
Gravitational acceleration	g	$9.8\,\mathrm{m/s^2}$
Static contact angle	θ_s	10°

Table 4.2: Parameters for simulations of gravity-driven detachment.

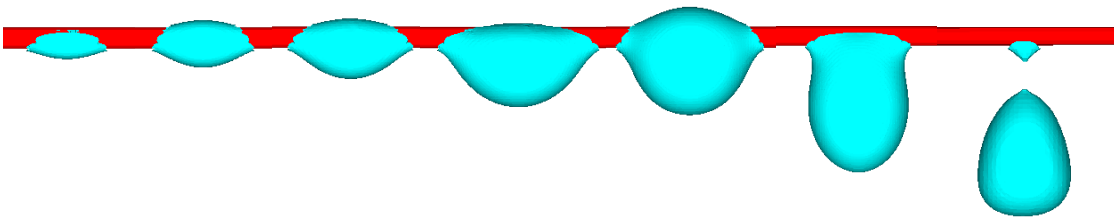

Figure 4.8: Drops of increasing size on a horizontal fiber. Fiber radius is 175 μm. Drop radii from left to right are 400, 500, 600, 800, 900, 1000, and 1100 μm.

In the following section, we perform simulations using the same parameters as reported in the experiment. The parameters are listed in Table 4.2. We place a

stationary drop on a horizontal hydrophilic fiber, and let it deform until it reaches a steady state. Numerical domains are not the same for unequal drop-to-fiber-size ratios, but the number of cells per fiber diameter is kept constant at 8.

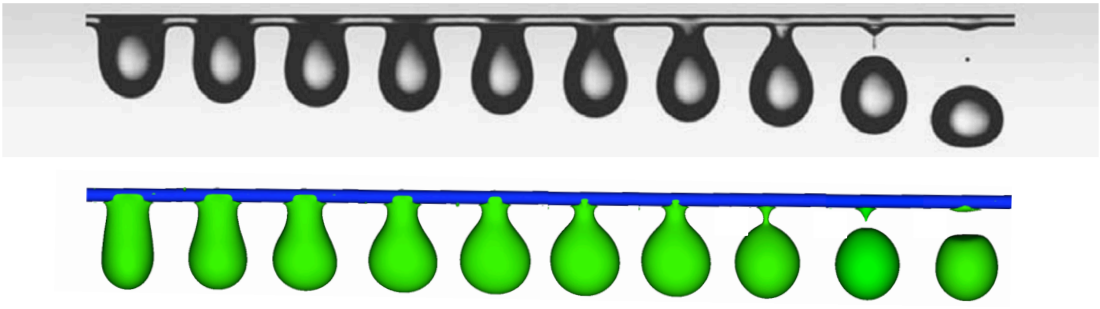

Figure 4.9: Set of pictures showing a drop falling off a fiber of radius $R_f = 350\,\mu$m. The upper images are from Lorenceau et al. [54]. The lower images are from the simulation.

Figure 4.8 shows the end of the simulation for several drop radii on the same fiber of radius $R_f = 175\,\mu$m. The drop radii, from left to right, are 400, 500, 600, 800, 900, 1000, and 1100 μm. In the series of simulations, only the largest drop is found to detach, which agrees with the prediction derived from Eq. 4.1. We now turn our attention to the process by which a drop above the critical radius detaches from the fiber: the process is shown in Figure 4.9. The upper images are from the experiment, and the lower images are from the simulation. The snapshots are taken at the same physical time as the experiment. Qualitatively, the simulation results show good agreement with the experimental pictures.

To facilitate further discussion, it is appropriate to introduce the Eötvös number[25], which is a dimensionless number measuring the importance of body

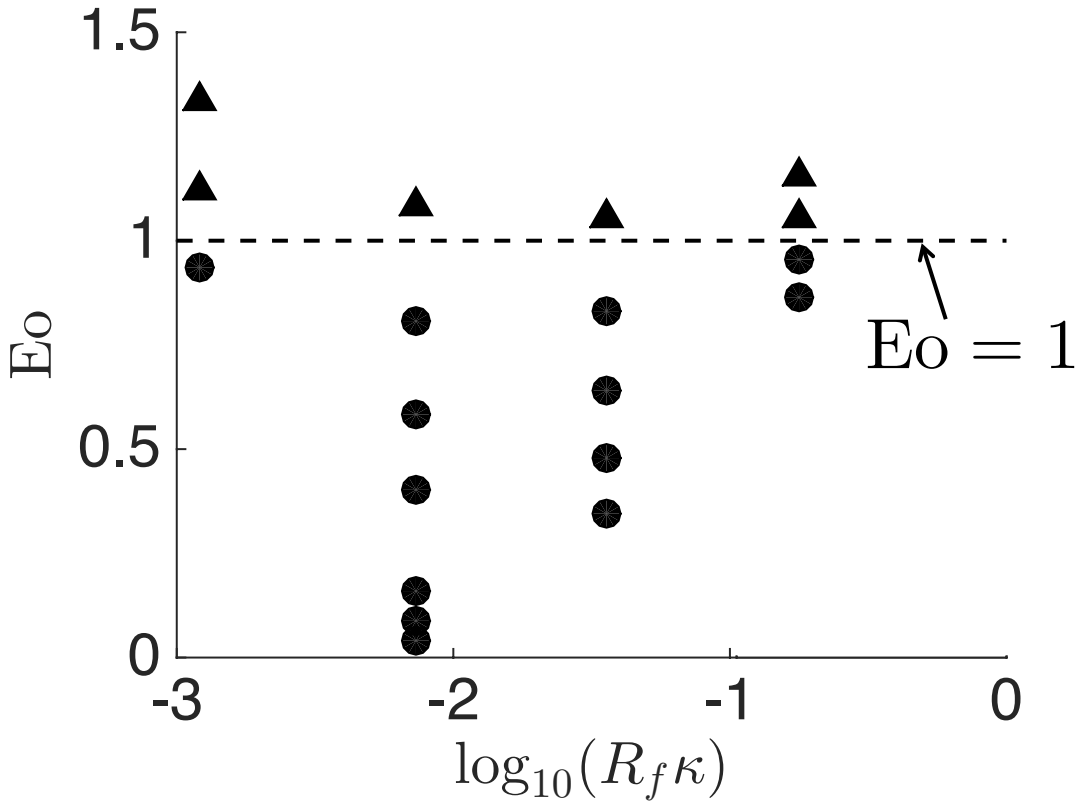

Figure 4.10: Regime map for gravity-driven detachment. Drops that have remained attached are shown as solid circles (•), and detached drops are shown as triangles (▲).

forces compared with surface tension forces. Here the Eötvös number is defined as

$$Eo = \frac{\text{weight}}{\text{surface tension force}} = \frac{\frac{4}{3}\pi R_d^3 \Delta\rho g}{4\sigma\pi R_f}, \tag{4.2}$$

where R_d is the radius of the drop. The surface tension force is estimated as $4\sigma\pi R_f$ in accordance with Lorenceau et al. [54]. An additional series of three simulations, considering fiber radii of 80 μm, 350 μm, and 700 μm, are performed. All the simulation results are presented in Figure 4.10 based on the Eötvös number and normalized fiber radii. The dashed line represents the Eötvös number that is equal to 1. Based on the simulation results, drops detach from the fiber if the corresponding Eötvös number is larger than 1, and drops remain on the fiber if

the corresponding Eötvös number is less than 1, providing a simple criterion for gravity-driven detachment.

4.3.2 Critical size of a drop on a hydrophobic fiber

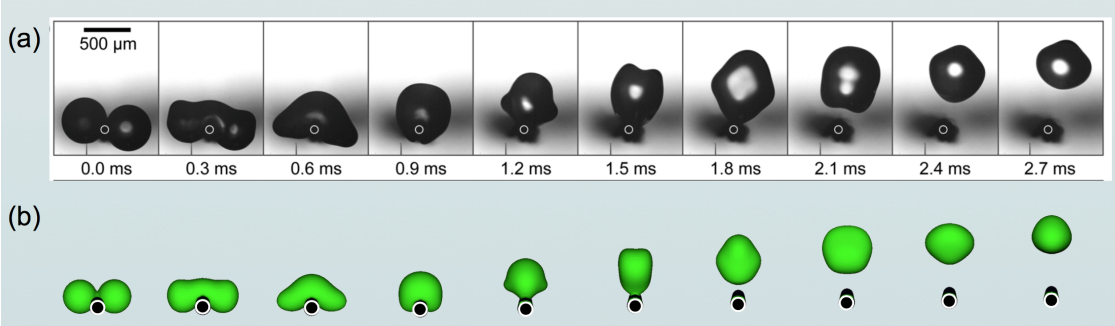

Figure 4.11: Self-propelled droplet removal from hydrophobic fiber. The upper images are from Zhang et al. [103]. The lower images are from simulation.

Zhang et al. [103] reported a self-propelled removal mechanism for droplets on hydrophobic fibers ($90° \leqslant \theta \leqslant 150°$). Above a certain drop-to-fiber-radius ratio, drops self-propel away from the fiber upon coalescence. The released surface energy upon coalescence powers the self-removal process, which operates independently of gravity or cross-flow. A 2D numerical simulation of the self-propelled departure process was performed in their work. Here, we use our numerical approach to simulate the self-propelled removal process on a round fiber in 3D.

The parameters in the simulation are shown in Table 4.3, and are taken from Zhang et al. [103]. The simulation is performed on a $400\times200\times200$ mesh, and there are 5 cells across the diameter of the fiber.

Figure 4.11 shows the 3D evolution of the droplet as it undergoes self-removal.

Drop radius	R_d	$249\,\mu$m
Fiber radius	R_f	$46\,\mu$m
Gas density	ρ_g	$1\,\mathrm{kg/m^3}$
Liquid density	ρ_l	$1000\,\mathrm{kg/m^3}$
Gas viscosity	μ_g	$1 \times 10^{-5}\,\mathrm{kg/(s \cdot m)}$
Liquid viscosity	μ_l	$1 \times 10^{-3}\,\mathrm{kg/(s \cdot m)}$
Surface tension	σ	$0.072\,\mathrm{N/m}$
Static contact angle	θ_s	120°

Table 4.3: Parameters for the simulation of self-propelled drop removal from a hydrophobic fiber.

The upper images are from Zhang's experiment, and the lower images are from our simulation. The images are taken at the same physical time as the experiment. The 3D simulation shows good qualitative agreement with the experiment, and seems able to accurately capture the propagation of capillary waves and the drop removal dynamics.

4.3.3 Critical size of a drop on a hydrophilic fiber subject to cross-flow

As the proposed numerical approach has been validated in gravity-driven and surface tension-driven detachment, it can now be applied to investigate the critical size of a drop on a hydrophilic fiber with cross-flow. The experiment is hard to perform with a uniform inflow condition, a relatively low evaporating rate, or micro-gravity. However, it is easy to perform the numerical test with uniform inflow, without evaporation or gravity.

The numerical test is performed under a constant Reynolds number, density ratio, viscosity ratio, and contact angle. We vary the drop-to-fiber-size ratio,

and the surface tension coefficient, to find the onset of detachment. The non-dimensional parameters are listed in Table 4.4.

Density ratio	ρ_l/ρ_g	65.5
Viscosity ratio	μ_l/μ_g	29.4
Drop Reynolds number	Re_d	200
Static contact angle	θ	10°

Table 4.4: Non-dimensional parameters for simulations of cross-flow detachment

Here the Weber number and the drop Reynolds number are

$$We = \frac{2\rho_g v_g^2 R_d}{\sigma} \text{ and } Re_d = \frac{2\rho_g v_g R_d}{\mu_g}, \tag{4.3}$$

where v_g is the gas cross-flow velocity, R_d is the initial radius of the drop, R_f is the radius of the fiber. We use the drop Reynolds number here because it is useful for determining the drag force on a drop in the following analysis.

As gravity is not considered in this section, the non-dimensional parameters of interest are the Weber number, We, and the radius ratio, R_d/R_f. The drops are smaller than their corresponding capillary lengths. The results are first gathered in a regime map, shown in Figure 4.12. The simulation seeks to determine whether the droplet will detach or stay. Detached drops are denoted in the figure by triangles, and drops that have remained attached are denoted by solid circles. The cross-flow detachment has been studied by Sahu et al. [78] . They found that the critical Weber number for vibrational break-up is approximately 6 over a large range of Ohnesorge numbers, and is close to the boundary between droplet attachment and detachment in Figure 4.12. The criterion, however, is not able to explain the detachment at $We = 5$, $R_d/R_f = 10$, and $We = 5$, $R_d/R_f = 15$. Comparing the cross-flow-driven detachment with the gravity-driven detachment, it is clear that

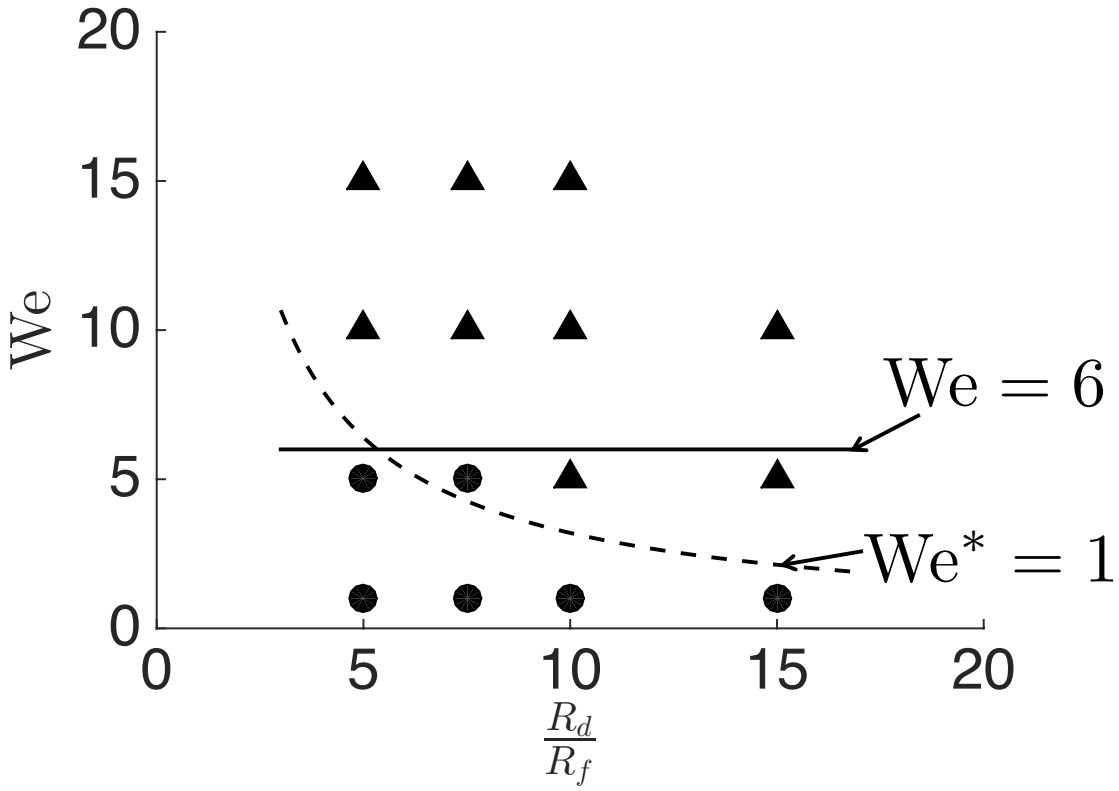

Figure 4.12: Regime map based on We and R_d/R_f. Drops that have remained attached are shown as solid circles (•), and detached drops are shown as triangles (▲).

a similar analysis can be conducted to predict a critical Weber number using a balance between the drag force and the adhesion force caused by surface tension. Here, a new Weber number is defined based on the ratio of the drag force and the surface tension force as

$$We^* = \frac{\text{drag force}}{\text{surface tension force}} = \frac{\frac{1}{2}\rho_g v_g^2 C_d A}{4\pi\sigma R_f}, \tag{4.4}$$

where C_d is the drag coefficient of a sphere, which is related to the drop Reynolds number, and A is the projected area of the droplet. Note that the new Weber number We^* depends on the Weber number We and on the drop Reynolds number Re_d. In Figure 4.12, the dashed line represents $We^* = 1$, which captures well the

boundary between droplet detachment and attachment very well.

4.4 Drop detachment from a fiber: effects of fiber shape and contact angle

Emerging 3D printing technologies make it possible to manufacture fibers with arbitrary cross-sectional shapes. Electrowetting [44] has become a practical approach to changing the surface wettability of fibers by adding an electrostatic field. As such, the fiber shape and wettability can now be controlled, and have the potential to become design parameters. In this section, we numerically examine the influence of fiber shape and wettability on the critical size of a drop on a horizontal fiber.

4.4.1 Numerical setup

Our numerical setup is shown in Figure 4.13. The fiber is aligned in the z- direction, and placed in the middle of the domain in the x- and y- directions. Initially, the drop is at the center of the numerical domain. The gravitational acceleration is in the direction of positive x-axis. Our simulations are performed on a uniform $200 \times 100 \times 100$ mesh. The numerical domain is periodic in the y- and z- directions. For our parametric study, we change the drop radius r_d, the fiber shape and its characteristic size λ_f, and the static contact angle θ_s. The details are given in Section 4.4.2. Note that, to ensure domain independence, the domain size in the y and z directions is at least 12 times the drop radius for all the simulations. We resolve the fiber with at least 4 numerical cells. Some simulation parameters

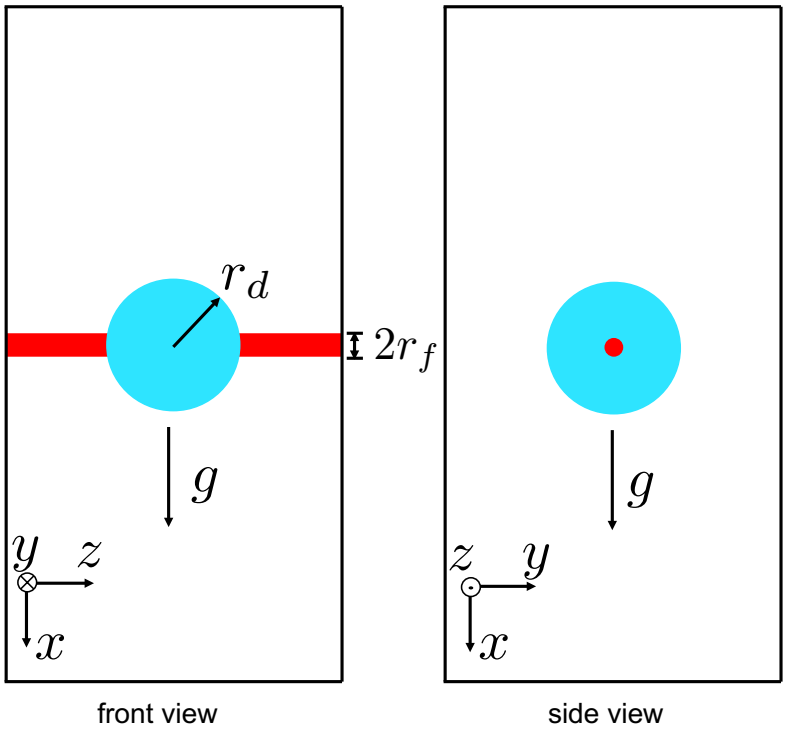

Figure 4.13: Numerical setup considered for the droplet detachment study.

remain constant and are listed in Table 4.5.

Domain size in x direction	L_x	8 mm
Domain size in y direction	L_y	4 mm
Domain size in z direction	L_z	4 mm
Gas density	ρ_g	1 kg/m^3
Liquid density	ρ_l	971 kg/m^3
Gas viscosity	μ_g	1×10^{-5} kg/(s $\cdot$ m)
Liquid viscosity	μ_l	1×10^{-3} kg/(s $\cdot$ m)
Surface tension	σ	0.0214 N/m
Gravitational acceleration	g	9.8 m/s^2

Table 4.5: Parameters for simulations of drop detachment from a fiber.

Three secondary parameters that will be used to explain the drop dynamics are introduced.

(1) The capillary length scale for the liquid is

$$\kappa^{-1} = \sqrt{\sigma/(\rho_l g)} = 1.5\,\text{mm}. \tag{4.5}$$

(2) The capillary time scale of the drop is

$$T_c = \sqrt{\rho_l r_d^3/\sigma}, \tag{4.6}$$

where r_d is the radius of the drop. Since the drop size considered in this study is on the order of 1 mm, we can estimate $T_c \approx 6.7$ ms.

(3) The free-falling time scale of the drop is

$$T_f = \sqrt{r_d/g}. \tag{4.7}$$

Again, for droplets on the order of 1 mm, T_f can be estimated to be on the order of 10 ms.

4.4.2 Validation

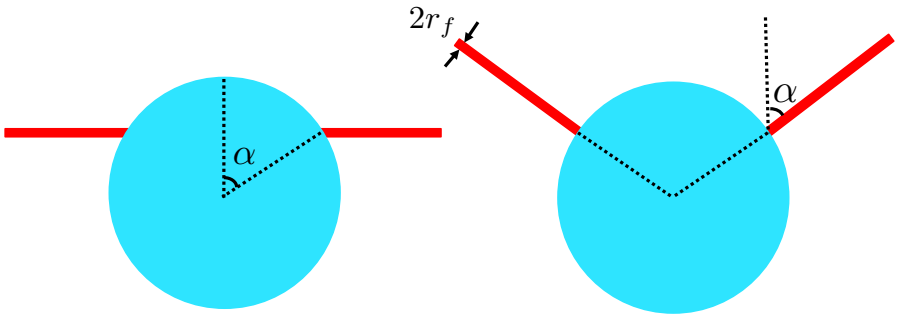

Figure 4.14: The left figure is a schematic of a large drop on a fiber. The right figure shows an equivalent configuration that generates the same amount of force on the drop, adapted from Lorenceau et al. [54].

Lorenceau et al. [54] proposed a model for estimating the adhesion force caused by surface tension acting on a drop on a horizontal cylindrical fiber. As shown in

Figure 4.14, the resulting force from the horizontal fiber is assumed to be equal to the force generated by the same two fibers through the drop center, written as

$$F = 2\sigma L f(\theta_s)\cos(\alpha), \tag{4.8}$$

where σ is the surface tension coefficient, L is the wetting length, taken as the circumference of the circle $L = 2\pi r_f$, $f(\theta_s)$ is a function related to the static contact angle, and α is the angle between the vertical line and a line that links the drop center to the contact point. For a fully wetting drop ($\theta_s \approx 0°$), $f(\theta_s)$ is approximated as 1. Therefore, the maximum adhesion force is calculated as $F_{\max} = 4\pi\sigma r_f$ by taking $\alpha = 0°$.

Recently, we introduced an Eötvös number using this estimation [94], which is the ratio of the weight of the drop to the surface tension force,

$$\mathrm{Eo} = \frac{\text{drop weight}}{\text{maximum adhesion force}} = \frac{\frac{4}{3}\pi r_d^3(\rho_l - \rho_g)g}{4\pi\sigma r_f}. \tag{4.9}$$

We reported that $\mathrm{Eo} = 1$ is a valid criterion with which to estimate the maximum size of a drop on a fiber under gravity, when the the fiber is characteristicly much smaller than the capillary length of the drop, i.e., $r_f \ll \kappa^{-1}$.

Note that Eq. (4.9) is limited to fully wet cylindrical fibers, which is unrealistic in the coalescer industry. In this study, we generalize the modeling of the maximum adhesion force exerted by the fiber on the drop to more general shapes and various static contact angles. We focus on thin fibers, with characteristic size much smaller than the capillary length scale of the flow.

We first examine the maximum size of a drop on a horizontal fiber with an equilateral triangular shape. The numerical tests are performed with various fiber

orientations. Three fiber sizes are considered for investigation, characterized by the triangle side length $\lambda_f = 0.16\,\text{mm}$, $0.35\,\text{mm}$, $0.7\,\text{mm}$. The static contact angle is set at 10°. The drop is initialized as stationary on the horizontal fiber, but then it deforms until it reaches a steady state, as shown in Figure 4.15, where the drop remains attached, or until it detaches, as shown in Figure 4.16. In Figures 4.15 and 4.16, it is clear that the characteristic spreading time, which is related to the capillary time scale T_c, is smaller than the free-falling time T_f, as the drop first spreads on the fiber, and then starts to fall due to gravity. This was expected based on the T_c and T_f estimates derived in Section 4.4.1. The mass conservation errors, ΔM, normalized by initial total mass, M_0, are shown in Figure 4.17 as a function of time for the simulations shown in Figures 4.15 and 4.16. The maximum mass error is less than 0.06% for both cases, showing good mass conservation. Figures 4.18 and 4.19 present results of a grid-independence study with respect to the drop shape for three varies mesh sizes ($r_f/\Delta = 1.0, 2.0, 4.0$). The results with $r_f/\Delta = 2.0$ and 4.0 are virtually overlapping, showing good convergence. The main difference observed between various mesh resolutions is seen in Figure 4.19: a satellite droplet appears upon droplet detachment at the finest mesh resolution but is not captured at lower resolutions. Hence, while the details of the separation and break-up process might still exhibit some mesh-dependence, we believe that whether or not detachment occurs is already fully mesh-independent. Therefore, we use $r_f/\Delta = 2.0$ in the simulations in the following section to save computational costs.

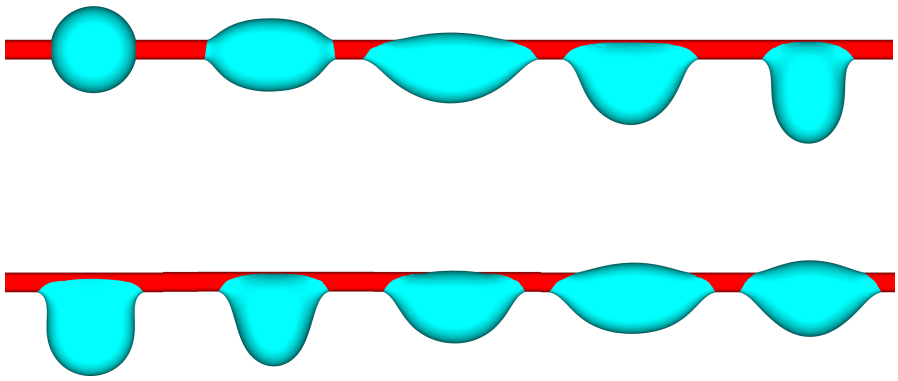

Figure 4.15: Set of pictures showing a drop remaining on an equilateral triangular fiber with side length $\lambda_f = 0.35\,\text{mm}$, point down. The radius of the drop is $r_d = 0.9\,\text{mm}$. The interval between two successive pictures is $\Delta t = 5\,\text{ms}$ (from left to right and from top to bottom).

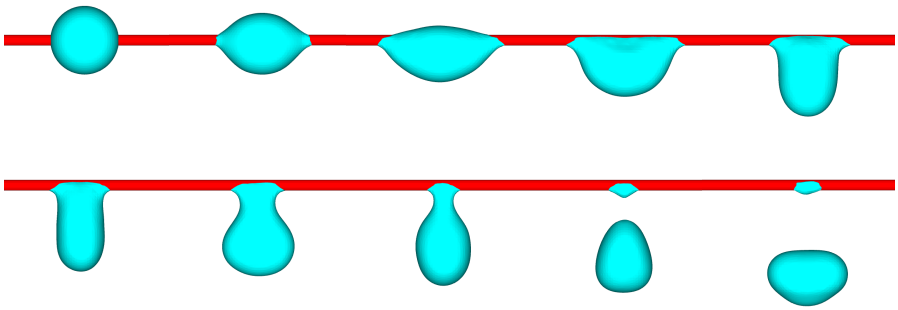

Figure 4.16: Set of pictures showing a drop falling off an equilateral triangular fiber with side length $\lambda_f = 0.35\,\text{mm}$, point down. The radius of the drop is $r_d = 1.1\,\text{mm}$. The interval between two successive pictures is $\Delta t = 5\,\text{ms}$ (from left to right and from top to bottom).

4.4.3 Fiber shape effects

We present all the results from simulations in regime maps in Figures 4.20 to 4.22 . In the abscissa, we plot the ratio of the fiber equivalent radius r_f to the capillary length κ^{-1} in log scale, and the ordinate is the Eötvös number. The drops that remain attached are shown as solid circles, while the detached drops are shown

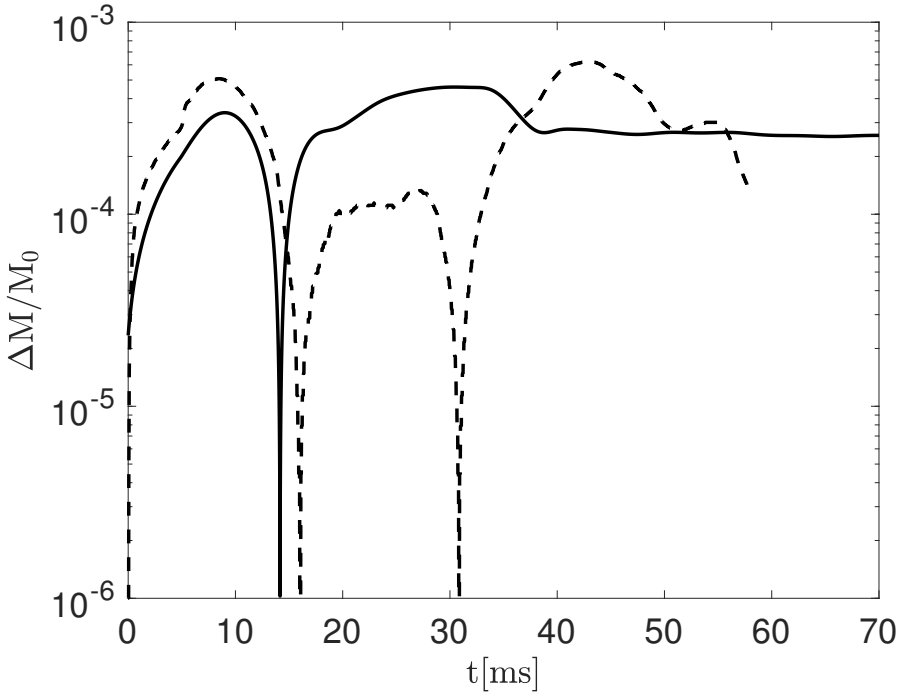

Figure 4.17: Mass errors versus time. The mass error calculated from Figure 4.15 is shown in dash line $(--)$, the mass error calculated from Figure 4.16 is shown in solid line $(-)$.

as triangles. The Eötvös number is approximated via Eq. (4.9), in which the equivalent radius is calculated by considering a circle with the same area as the triangle,

$$L = 2\pi r_f = 2\pi\sqrt{\frac{\frac{3}{4}\lambda_f^2}{\pi}}. \tag{4.10}$$

We note that Eo = 1 in Figures 4.20 to 4.22 does not clearly demarcate the attached and detached drop regimes. Instead of using r_f in Eq. (4.10) to calculate Eo in Eq. (4.9), we employ the circumference of the equilateral triangle $3\lambda_f$ as the wetting length L to compute a modified Eo*,

$$\mathrm{Eo}^* = \frac{\frac{4}{3}\pi r_d^3(\rho_l - \rho_g)g}{6\sigma\lambda_f}. \tag{4.11}$$

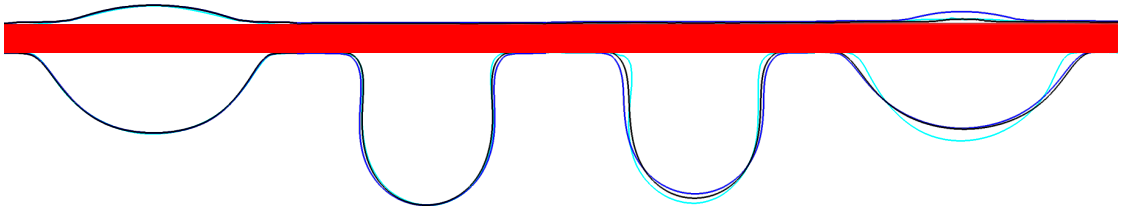

Figure 4.18: Convergence of interface shape at $t = 10$, 20, 30, 40 ms in the simulation of a drop that remains on the fiber (Figure 4.15). The 2D droplet shapes at the cut plane are shown here. Three levels of resolution are plotted: $r_f/\Delta = 1.0$ is in cyan, $r_f/\Delta = 2.0$ is in blue, and $r_f/\Delta = 4.0$ is in black.

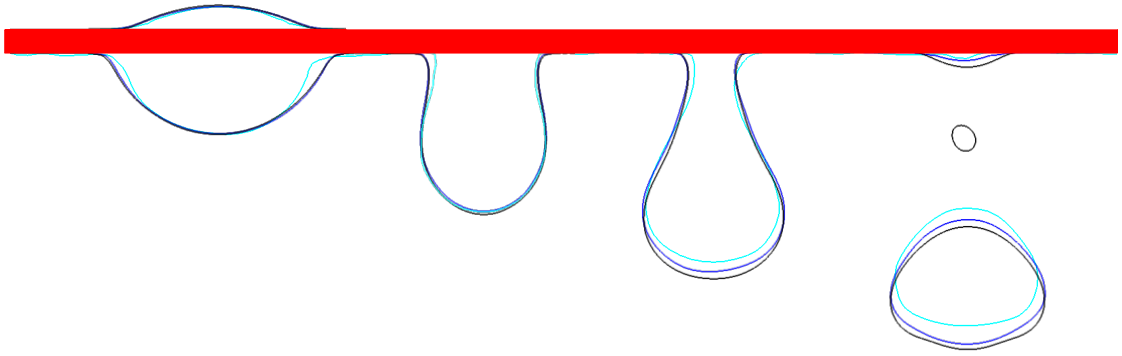

Figure 4.19: Convergence of interface shape at $t = 10$, 20, 30, 40 ms in the simulation of a detached drop (Figure 4.16). The 2D droplet shapes at the cut plane are shown here. Three levels of resolution are plotted: $r_f/\Delta = 1.0$ is in cyan, $r_f/\Delta = 2.0$ is in blue, and $r_f/\Delta = 4.0$ is in black.

The $\mathrm{Eo}^* = 1$ is represented as a dashed line in Figures 4.20 to 4.22.

Comparing Figures 4.20 to 4.22, the orientation effect of the fiber in the regime diagram appears to be negligible. The fiber circumference seems to be a better estimate of the wetting length, as the dashed line demarcates the two different

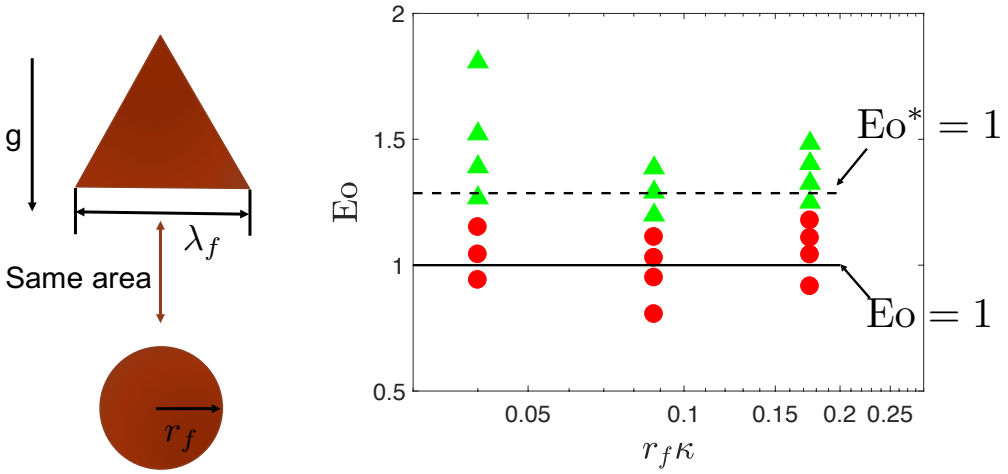

Figure 4.20: Droplet detachment from an equilateral triangular fiber, point up. Drops remaining attached are shown with solid circles (●), and detached drops are shown with triangles (▲).

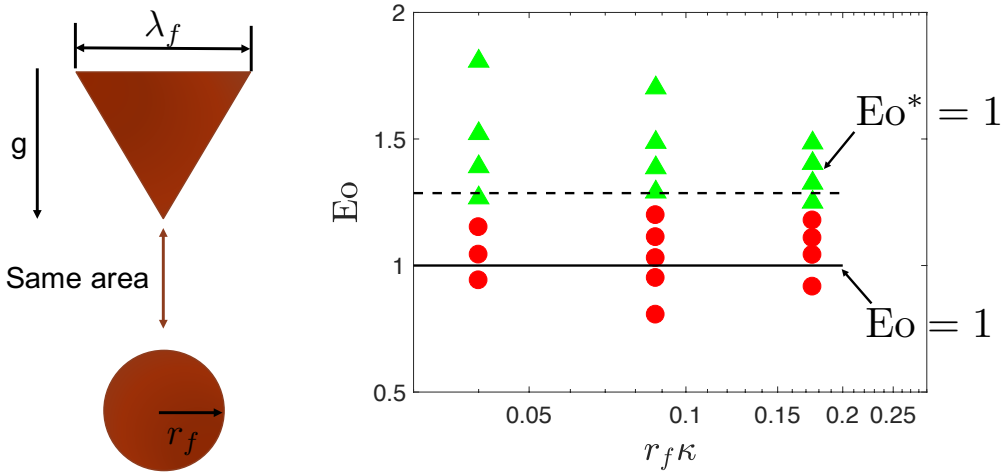

Figure 4.21: Droplet detachment from an equilateral triangular fiber, point down. Drops remaining attached attached are shown as solid circles (●), and detached drops are shown as triangles (▲).

regimes with fewer mis-classificated cases.

We add another set of cases with a pill-shaped fiber, for which the results are shown in Figure 4.23. Eq. (4.11) performs well to demarcate the two different regimes for thinner fibers, but the model overestimates the critical drop size for larger fibers shown in Figure 4.23. This is because the characteristic length of the

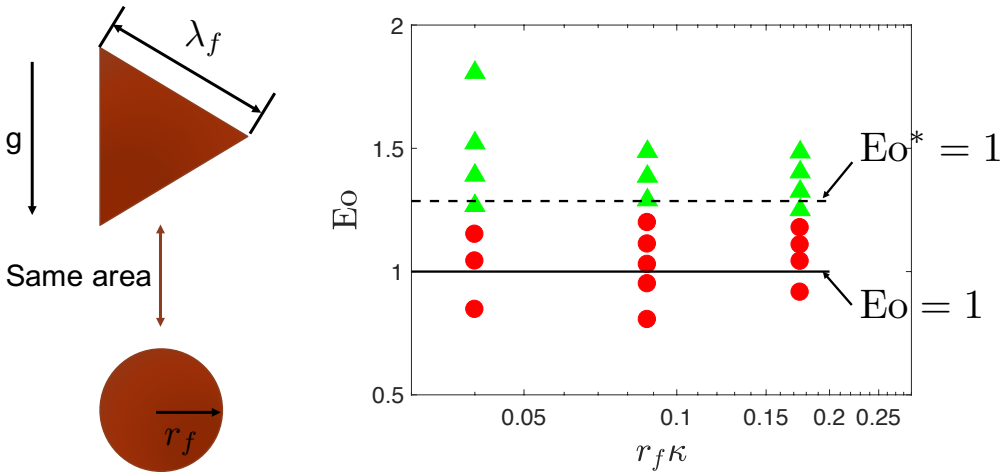

Figure 4.22: Droplet detachment from an equilateral triangular fiber, point right. Drops that have remained attached are shown with solid circles (●), and detached drops are shown with triangles (▲).

fiber is close to the capillary length of the drop, and the thin fiber assumption is no longer valid in this case.

4.4.4 Fiber wettability effects

Although many studies has been performed to investigate the difference in the behavior of a single drop on hydrophobic and hydrophilic fibers [103, 39, 66] with pre-determined static contact angles, very few studies have considered the effect of varying static contact angles in the hydrophilic region. In this sub-section, we focus on the influence of the static contact angle. Since we have already examined the influence of fiber shape, we consider only thin cylindrical fibers here. The radius of the fiber r_f is 0.35 mm. The static contact angle varies from 10° to 80° at increments of 10°.

A model used by Park et al. [70] is first introduced, in which the maximum

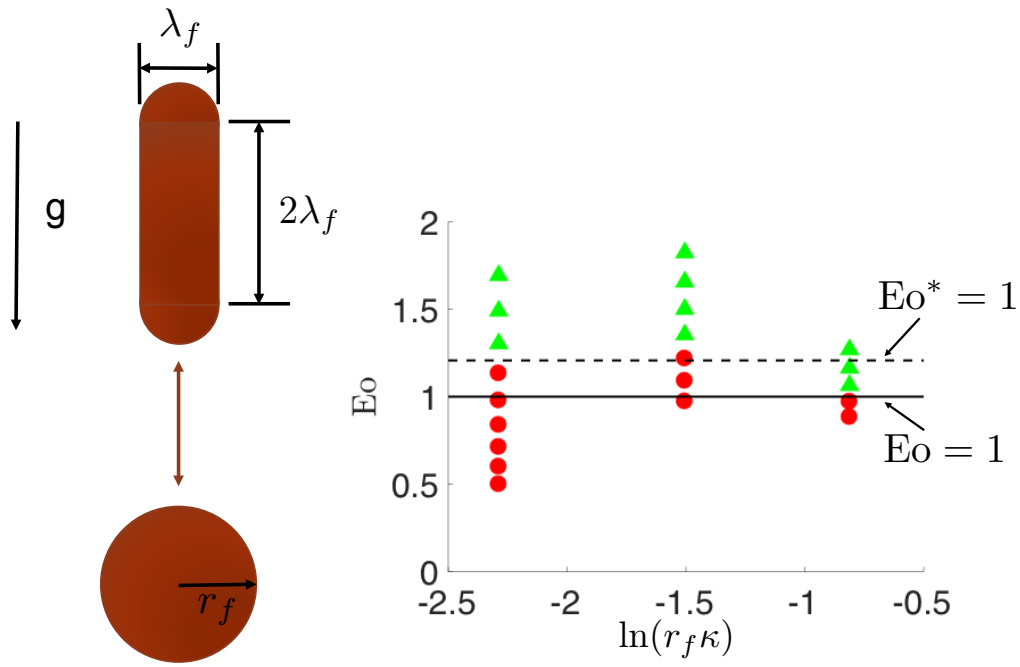

Figure 4.23: Droplet detachment from a fiber with pill shape. Drops remaining attached attached are shown as solid circles (•), and detached drops are shown as triangles (▲).

adhesion force is

$$F = \sigma L(1 + \cos(\theta_s)). \tag{4.12}$$

Then the corresponding Eötvös number in Eq. (4.9) is

$$\mathrm{Eo}^* = \frac{\frac{4}{3}\pi r_d^3(\rho_l - \rho_g)g}{2\pi\sigma r_f(1 + \cos(\theta_s))}. \tag{4.13}$$

For the purpose of making a comparison, we propose a crude model to estimate the maximum adhesion force on a drop on a fiber,

$$F = 2L\sigma\cos(\theta_s), \tag{4.14}$$

where L is the wetting length. Since we consider a circular cylinder, the wetting length is given by $L = 2\pi r_f$ and we will consider it independently of θ_s in this study. As a result, the Eötvös number in Eq. (4.9) is

$$\mathrm{Eo} = \frac{\frac{4}{3}\pi r_d^3(\rho_l - \rho_g)g}{4\sigma\pi r_f\cos(\theta_s)}. \tag{4.15}$$

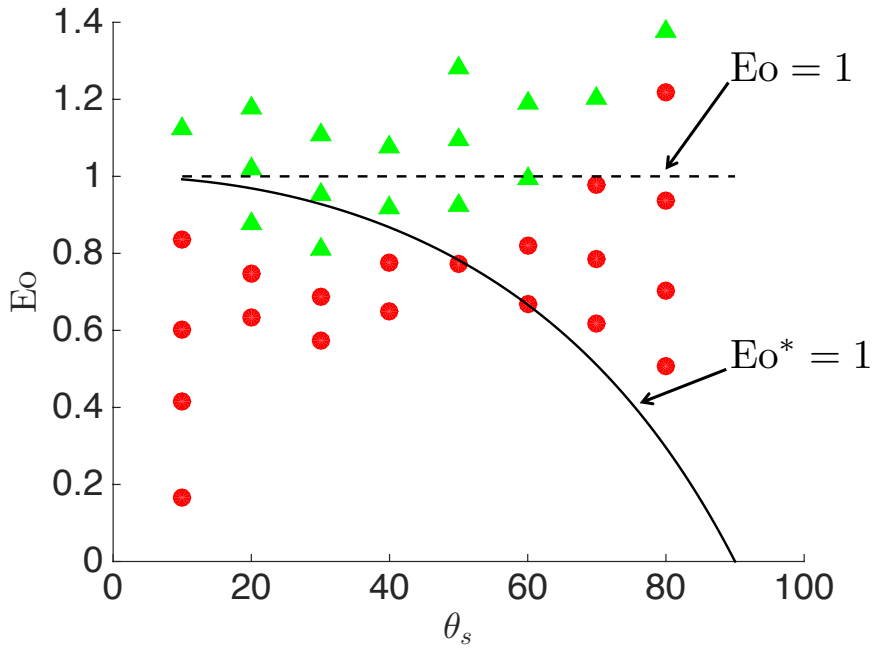

Figure 4.24: Droplet detachment from a horizontal cylindrical fiber with different wettability. Drops remaining attached are shown as solid circles (●), and detached drops are shown as triangles (▲).

The simulation results are collected in Figure 4.24. Drops that remain attached are drawn as solid circles, and detached drops are drawn as triangles. Eq. (4.13) is depicted as a solid line, and Eq. (4.15) is depicted as a dashed line. Eq. (4.15) demarcates the two seperate regimes with fewer mis-classification cases, and is within 20% of the critical Eötvös number obtained from simulations for all static contact angles considered.

The critical Eötvös number is non-monotonic with respect to the static contact angle. Two aspects should be considered in the future to provide a better estimation of the critical Eötvös number. On the one hand, the wetting length L decreases as the static contact angle increases. On the other hand, the contact angle is actually the receding contact angle, which is narrower than the static contact angle, and it exerts greater influence on the critical Eötvös number when the

contact angle is close to 90°.

4.5 Conclusion

In this chapter, numerical studies on drop-fiber interactions, such as drop impact on a fiber and drop detach from a fiber, have been performed.

In the drop-impact-on-a-fiber case, our simulation is able to reproduce all the impact patterns, i.e., capturing, single-drop falling, and splitting. Furthermore, the reproduced regime diagram agrees with the experiments [47]. We also demonstrated that the impact patterns were different for different fiber wettabilities.

Many quantitative studies have been performed in the drop-detachment case. In gravity-driven detachments, we derived an Eötvös number-based criterion. This criterion has been further developed to account for the fiber shape and wettability effects. We then performed an exploratory study in cross-flow-driven detachment. A critical Weber number was found for detachment. These models will be employed in the design and reduced-order modeling of liquid-gas coalescers in the future.

CHAPTER 5

JET PLANE INTERACTION

5.1 Introduction

Jet plane interaction is universal in many industrial processes, such as spray cooling, spray coating, and spray injection inside internal combustion engines. This phenomenon has also been widely studied due to its beauty, variety, and applicability.

Current applications of jet wall interactions involve empirical models that are developed from experimental observations. The application of empirical models implies extensive use of tunable parameters to achieve an accurate match with reality. To avoid using tunable parameters, direct numerical simulations (DNS) seem to be an alternative technique, assisted by increasingly rich computing resources and improved numerical algorithms.

In this chapter, we aim to systematically assess the predictive capability of our numerical framework in simulations of jet plane interaction. To achieve this goal, we first validate the simulations against the experiments. Then, we perform parametric studies on the influence of gravity and surface wettability on the jet-bouncing phenomena.

5.2 Numerical setup

Our numerical setup is illustrated in Figure 5.1. A jet with diameter d_j is injected into a wall with an incident angle of ϕ_i. w is the width , h is the height, and l is

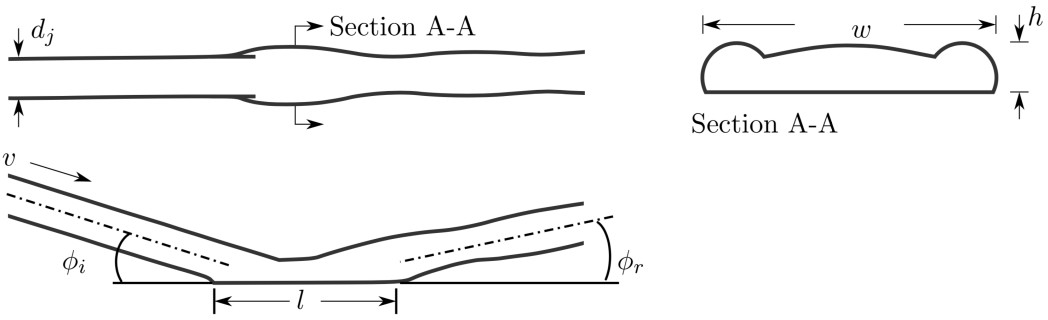

Figure 5.1: Numerical setup considered for simulations of jet plane interaction: profile view, top view, and section view of the landing flow at the point of maximum width w.

the length of the landing area. ϕ_r is the rebound angle. Following the microgravity experiments by performed Kardins et al.,[12] the physical parameters of the liquid and gas phases are collected in Table 5.1.

Gas density	ρ_g	$1\,\mathrm{kg/m^3}$
Liquid density	ρ_l	$971\,\mathrm{kg/m^3}$
Gas viscosity	μ_g	$1 \times 10^{-5}\,\mathrm{kg/(s \cdot m)}$
Liquid viscosity	μ_l	$1 \times 10^{-3}\,\mathrm{kg/(s \cdot m)}$
Surface tension	σ	$0.072\,\mathrm{N/m}$
Static contact angle	θ_s	158°

Table 5.1: Parameters for simulations of jet plane interaction.

In our simulations, the pressure discontinuity caused by surface tension is solved using the ghost fluid method [36]. The solid phase is assumed to be stationary. A conservative immersed boundary method based on the cut-cell method [62] is employed to represent the solid phase, as implemented by Desjardins et al.[30]. The contact line model in this study is based on a curvature boundary condition method [94] proposed originally by Luo et al. [57]. The mathematical description presented above is implemented in the framework of the NGA code [31]. The

Navier-Stokes equations are solved on a staggered grid with second-order spatial accuracy for both convective and viscous terms, and by the semi-implicit Crank-Nicolson scheme with second-order accuracy for time advancement.

The simulation parameters are exactly the same as those incorporated into the experiment. Figure 5.2 shows a grid-independence study with respect to the landing area of the unstable jet shown in Figure 5.3. Three mesh sizes of $d_j/\Delta = 4.8, 9.6$, and 19.2, are simulated, where Δ is the mesh size in the simulations. The results with $d_j/\Delta = 9.6$ and $d_j/\Delta = 19.2$ are virtually overlapped, showing good convergence. Therefore, we use $d_j/\Delta = 9.6$ in the simulations in the following to save computational costs.

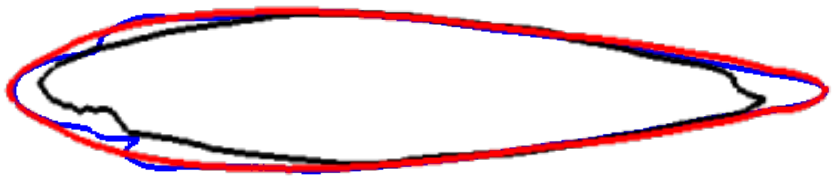

Figure 5.2: Convergence study for the shape of the landing area. The numerical results are obtained on meshes of varying resolutions: $d_j/\Delta = 4.8$ (black), 9.6 (blue), and 19.2 (red).

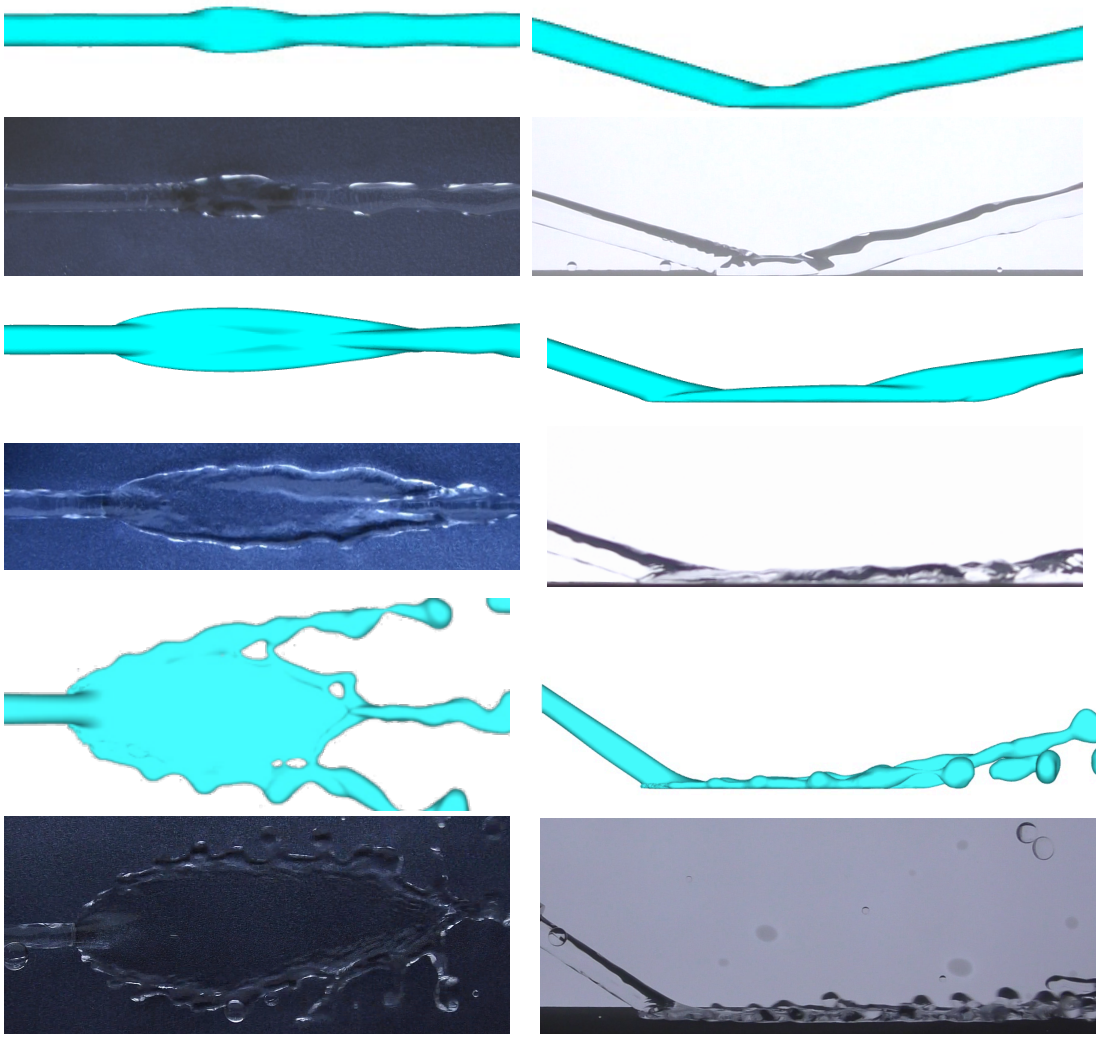

Figure 5.3: Comparison of images from drop tower test and numeric simulation for 6 mm jet. Top: stable, $\phi_i = 15°$, $v = 0.51\,\mathrm{m/s}$, $\mathrm{We}_\perp = 1.45$. Middle: unstable, $\phi_i = 18°$, $v = 1.10\,\mathrm{m/s}$, $\mathrm{We}_\perp = 9.6$. Bottom: splashing, $\phi_i = 34°$, $v = 1.2\,\mathrm{m/s}$, $\mathrm{We}_\perp = 37.5$.

5.3 Validations

A free jet can be characterized by the Reynolds number, $\mathrm{Re} = \rho_l v d_j / \mu_l$. Regarding jet impact on any substrate, the jet-bounce phenomenon depends on the impact

Weber number $\mathrm{We}_\perp = \rho_l (v \sin(\phi_i))^2 d_j / \sigma$, the surface wettability θ_s, and the Eötvös number $\mathrm{Eo} = (\rho_l - \rho_g) g d_j^2 / \sigma$, where g is the gravitational acceleration.

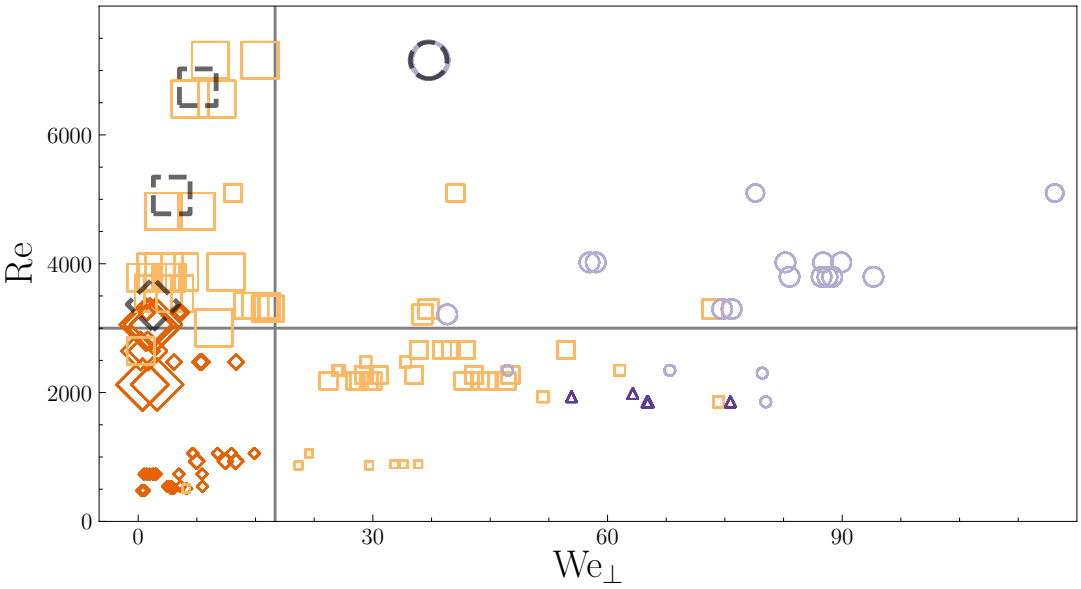

Figure 5.4: Regime map illustrating the observed dependence of flow structures emerging from the oblique impact of jets on a superhydrophobic substrate. Four distinct regimes are identified: stable(◇), unstable(□); splashing(◯); rivulet jet collision(△). Marker size is proportional to the diameter of the jet and dashed bold markers represent simulation runs. The horizontal line at $\mathrm{Re} = 3000$ marks the transition to turbulent flow while the vertical line at $\mathrm{We}_\perp = 17.5$ marks the prediction of instability.

A selection of jet rebounds are shown in Figure 5.3. Simulations of the stable and unstable jets are close to the experimental snapshots. The landing widths match well with those in the experiment for all three cases. In the splashing jet case, however, the spreading length is underestimated, and the satellite drops are not fully captured in the splashing jet. These discrepancies require further investigation. Following Celestini et al.[14], stable rebounds are those where the rebounded jet profile is steady. Oscillations in the secondary jet originate from the rim impact and propagate along the rebounded jet. The secondary jets resulting

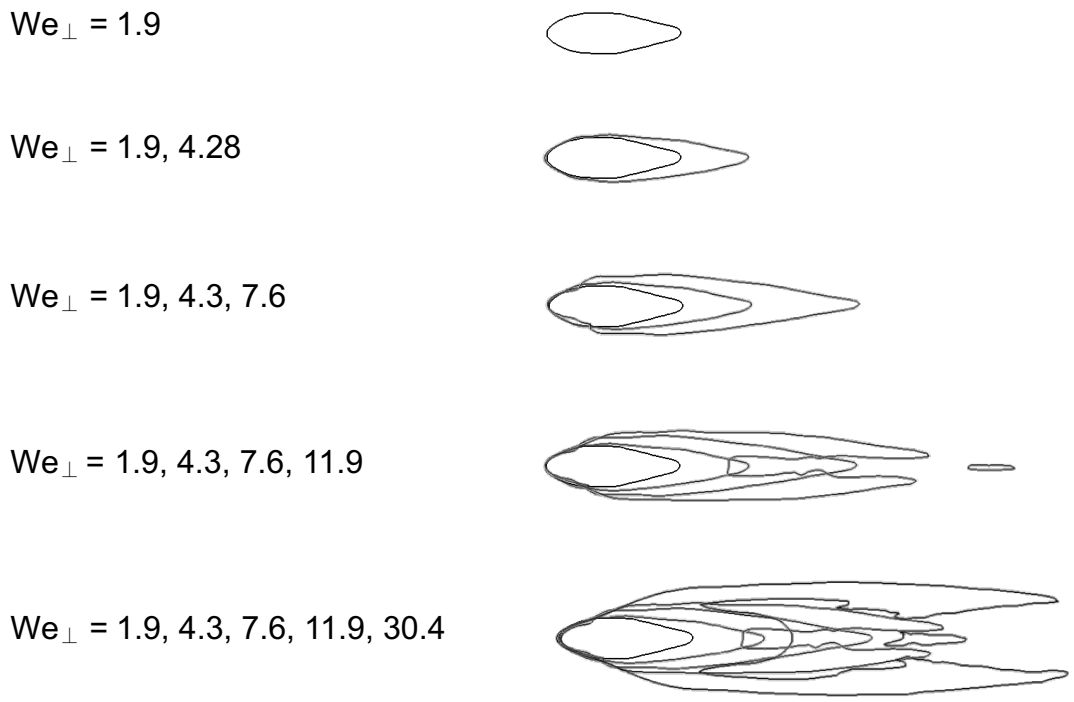

Figure 5.5: Landing area of the jet with increasing Weber number.

from unsteady rebounds are marked by unsteady periodic undulations, oscillations, and premature Rayleigh breakup. The landing flow structure provides additional distinctions on the basis of which to further classify the rebound behavior. In Figure 5.4, the landing structure types shown in Figure 5.3 are presented in regime map form in terms of Reynolds number Re and perpendicular Weber number $\mathrm{We}_\perp$. As observed on the map, stable rebounds occur in the region of the lowest-inertia laminar jets where $\mathrm{Re} \lesssim 3000$ with $\mathrm{We}_\perp \lesssim 20$. The dashed bold markers represent simulation runs, which show excellent agreement with the classification based on experimental data.

The stable jet landing flow is a characterized by a relatively small maximum width w and equally smooth and steady bounding rims. The value of w depends far more on the perpendicular jet velocity than on the tangent jet velocity. For

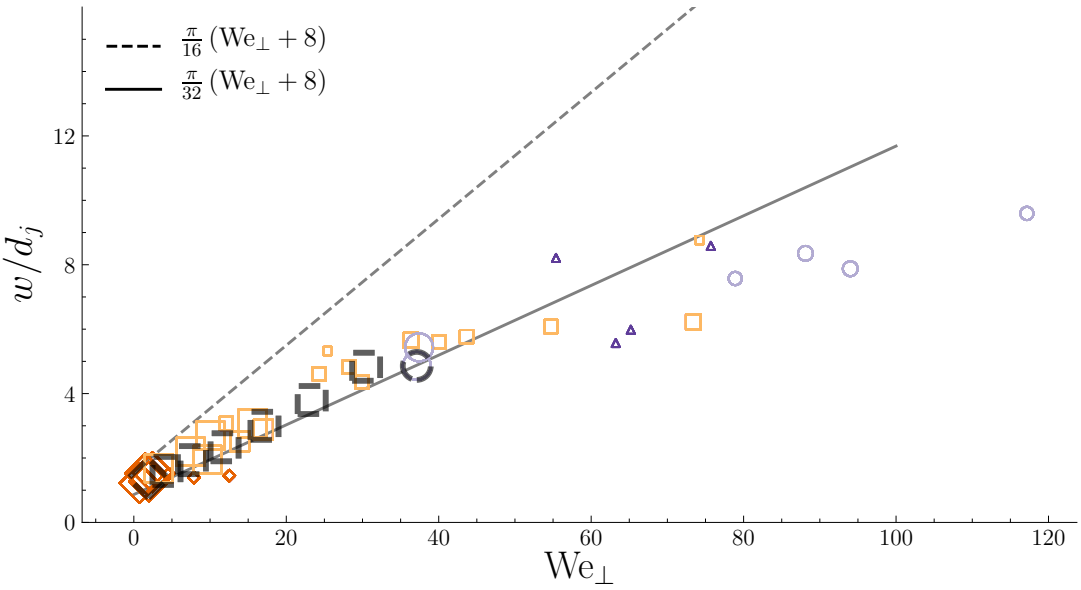

Figure 5.6: Normalized maximum landing width w/d_j vs $\mathrm{We}_\perp$. Four distinct regimes are identified: stable($\diamond$), unstable($\square$); splashing($\bigcirc$); rivulet jet collision($\triangle$). Marker size is proportional to the diameter of the jet and dashed bold markers represent simulation runs. The dashed line represents the prediction based on conservation of energy and the solid line is the same equation with a prefactor of 0.5.

stable rebounds, the landing flow width is less then twice the initial jet diameter. The ratio w/d_j is plotted against $\mathrm{We}_\perp$ in Figure 5.6. Estimating the landing flow can be straightforwardly by considering energy conservation between the energy associated with the normal velocity of the free jet and the zero velocity landed jet. Such an approach has been adopted by [45] and [46]. Kardins et al. [12] predicts

$$\frac{W}{d_j} = \frac{\pi(\mathrm{We}_\perp + 8)}{16}. \tag{5.1}$$

Equation 5.1 is overlaid on Figure 5.6 to display qualitative agreement with both experiments and numerics. Equation 5.1 is also plotted with a prefactor of 0.5. This prefactor reduces the error between the predicted and experimental

widths within the near-linear region at $\mathrm{We}_\perp < 40$. A series of simulations with increasing jet velocity are performed in this section. The incident angle is $\phi_i = 17°$. These jet velocities are 0.5, 0.75, 1.0, 1.25, and 2 m/s. The corresponding impact Weber numbers are listed in Figure 5.5, with their liquid-gas interfaces on the wall. As shown in the figure, the landing width and the landing length increase with respect to the impact Weber number, and the simulated maximum landing width exhibits an excellent agreement with the experimental measurement and the theory.

5.4 Gravity effects

Gravity was not considered in the aforementioned simulations. Almost all the previous experiments are performed either without gravity or with $g = 9.80\,\mathrm{m/s^2}$. Very few experimental studies have considered $0\,\mathrm{m/s^2} < g < 9.80\,\mathrm{m/s^2}$, because gravity is not a tunable parameter on Earth. However, we can easily change the gravitational acceleration in simulations. Therefore, we perform a study of the effects of gravity on the jet-bouncing phenomenon.

We select a case: $v = 0.62\,\mathrm{m/s}$, $\phi_i = 30°$, $d_j = 6\,\mathrm{mm}$. The corresponding impact Weber number is $\mathrm{We}_\perp = \rho_l (v \sin(\phi_i))^2 d_j/\sigma = 8.0$, and the Reynolds number is $\mathrm{Re} = \rho_l v d_j/\mu_l = 3720$. Three gravitational accelerations are chosen, i.e., $g =$ 0.1, 1, and 4.9 $\mathrm{m/s^2}$. The corresponding Eötvös numbers are shown in Figure 5.7, along with a side view of the jets. In the test case with Eo = 0.05, the jet still bounces away from the surface, but it becomes unstable, as can be observed where the jet breaks up into droplets downstream. In the test case with Eo = 0.50, the jet also bounces away from the surface, but it falls back due to gravity. In the test

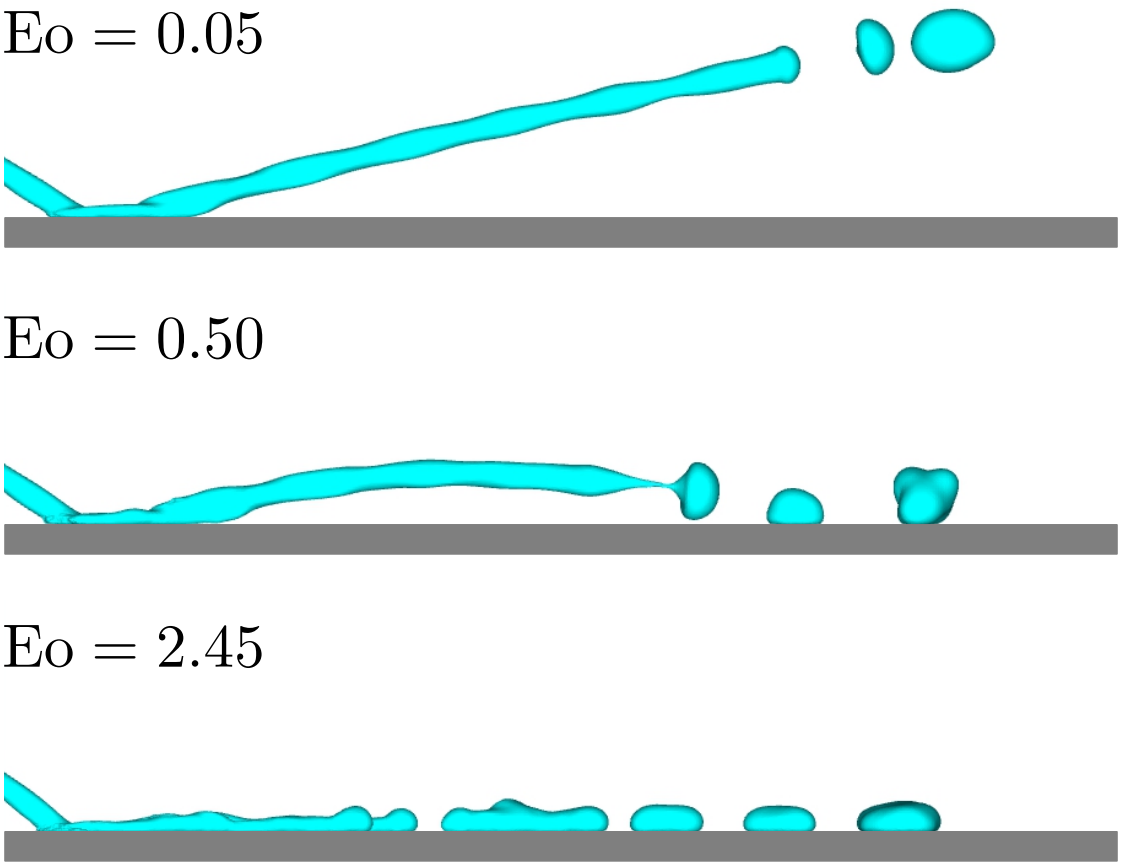

Figure 5.7: Side view of bouncing jets with increasing Eötvös number.

case with Eo = 2.45, the jet never rebounds away form the surface, and it is less stable in the other previous cases with low Eötvös numbers cases. In short, the jet-bounce phenomenon is also controlled by gravitational acceleration. Thus, a microgravity environment is required to perform experiments with bouncing jets.

5.5 Surface wettability effects

Microgravity experiments with various contact angles are not yet available. Fortunately, we can easily change the contact angle in simulation. Therefore, in this

section we perform an exploratory study of wettability effects on the jet-bouncing phenomenon.

We select a case: $v = 0.65\,\mathrm{m/s}$, $\phi_i = 17.6°$, $d_j = 6\,\mathrm{mm}$. The corresponding impact Weber number is $\mathrm{We}_\perp = \rho_l(v\sin(\phi_i))^2 d_j/\sigma = 3.29$, and the Reynolds number is $\mathrm{Re} = \rho_l v d_j/\mu_l = 3900$. Five contact angles are chosen, i.e., $\theta_s = 30°$, $60°$, $90°$, $120°$ and $158°$. The jet profiles are collected in Figure 5.8. The landing width increases as the contact angle narrows. Only in the case with the $\theta_s = 158°$ do we see a jet bouncing away from the surface. The remaining jets land on the surface. A chain structure [11], which is a succession of mutually orthogonal links, can be observed in $\theta_s = 60°$, $90°$, $120°$ and $158°$ cases. And the middle of the chain in the $\theta_s = 60°$ case is not covered by liquid. This interesting chain structure requires future experimental validation and theoretical interpretations. Although we demonstrated in Section 5.2 that the simulations converged with mesh refinement, that test case did not consider jet breakup. The simulations are possibly under-resolved because of the presence of jet break-up, which in the future will require a simulation on a finer mesh. Nevertheless, we conclude that the flow pattern of a bouncing jet is also controlled by surface wettability.

5.6 Conclusion

In this chapter, we have assessed the predictive capability of our code in jet-plane interaction problems. Numerical results were first validated against a microgravity experiment performed by Kardins et al. [12]. We have shown that the simulation was able to predict the flow patterns at various impact Weber numbers and Reynolds numbers. The impact width of the jet was well predicted with good

accuracy by the simulation. We then conducted exploratory studies of gravity and surface wettability effects. We have shown that gravity destabilizes the bouncing jet and the wetting width grows as the contact angle decreases. This study takes a first step towards simulating jet-plane interactions. Because the computational cost of each simulation is still high, future work will focus on extracting reduced-order models.

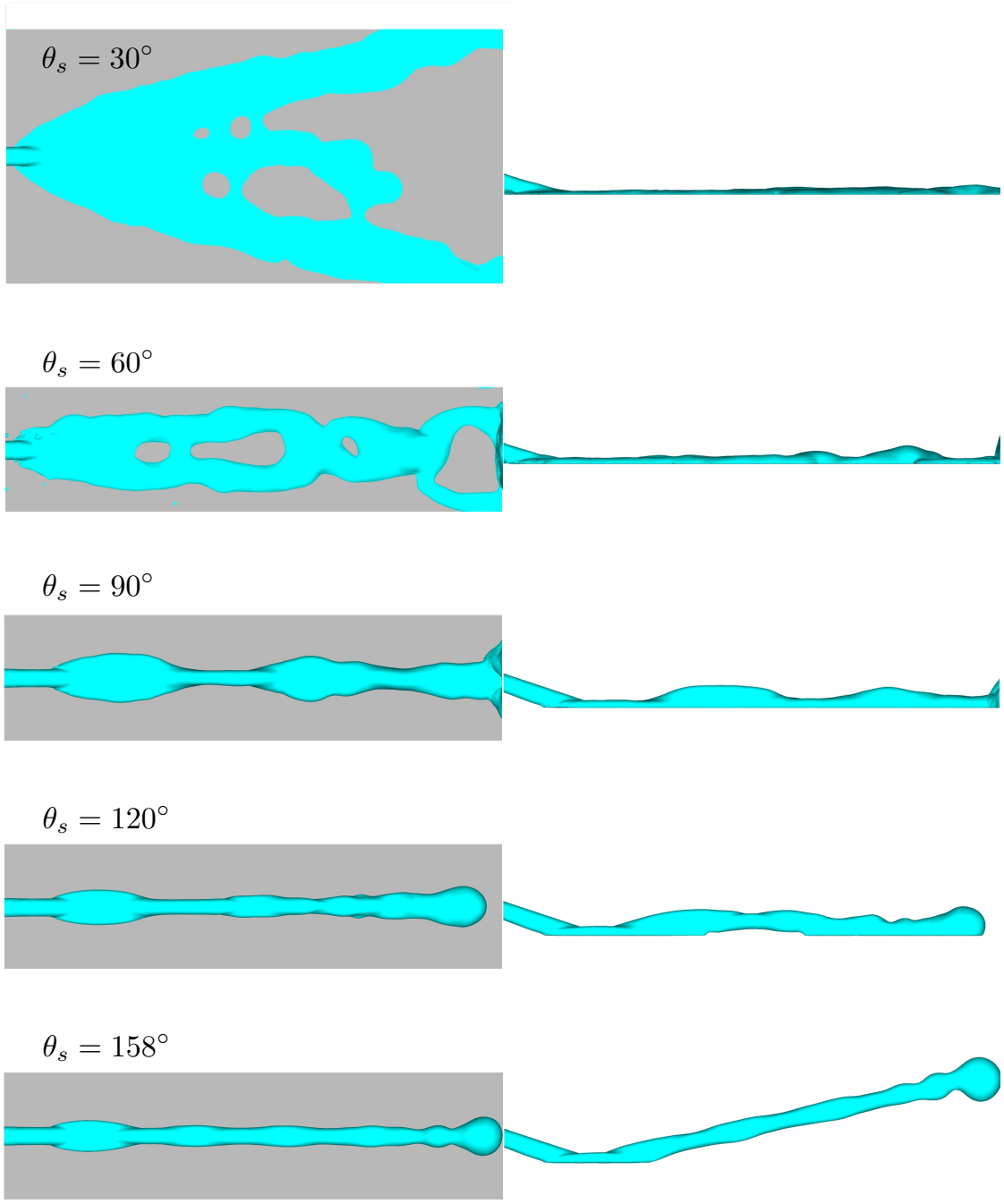

Figure 5.8: Simulations of bouncing jets with various contact angles. Top view is on the left, side view is on the right.

CHAPTER 6

CONCLUSIONS AND PERSPECTIVES

In this dissertation, we have developed a numerical framework for large-scale simulation of two-phase flows with moving contact lines in complex geometries. This framework utilizes a conservative level-set method to capture the liquid-gas interface, a conservative immersed boundary method to represent the solid phase, and the uncompensated Young's force method to impose a contact angle. This framework has been verified to be conservative, accurate, and robust in simulating two-phase flows with moving contact lines.

To simulate viscous-force-dominated two-phase flows with moving contact lines, we first derived a volume-filtered NS equation, and identified two unclosed terms: an SGS surface tension force and an SGS viscous force. The uncompensated Young's force was used to close the SGS surface tension force; a physics-based viscous force model was derived to close the SGS viscous force. The SGS viscous force is the same as the viscous part of the Cox-Voinov theory under small contact-angle conditions.

To assess the predictive capability of the current numerical approach, we performed simulations of drop-fiber interaction and jet-plane interaction, and compared the results with their corresponding experimental results. The simulation results generally agree with the experimental results except for cases with thin films.

Moving forward, careful assessment of the SGS viscous force model should be conducted at first. Such an assessment requires a detailed comparison with experimental data and other numerical approaches that use the Cox-Voinov theory

for dynamic contact-angle modelling.

This study is restricted to hydrodynamics. Other physics, such as surface roughness, electro-static force, surfactants, and evaporation, should be considered in the future.

The majority of extant studies of moving contact lines focus on a single drop interaction with a flat wall. Our numerical approach enables the study of multiple drops or jets interacting with irregular surfaces, which can be investigated in the future.

BIBLIOGRAPHY

[1] T. Abadie, J. Aubin, and D. Legendre. On the combined effects of surface tension force calculation and interface advection on spurious currents within volume of fluid and level set frameworks. *Journal of Computational Physics*, 297(Supplement C):611–636, 2015.

[2] M. O. Abu-Al-Saud, C. Soulaine, A. Riaz, and H. A. Tchelepi. Level-set method for accurate modeling of two-phase immiscible flow with moving contact lines. *ArXiv e-prints*, August 2017.

[3] S. Afkhami, S. Zaleski, and M. Bussmann. A mesh-dependent model for applying dynamic contact angles to vof simulations. *Journal of Computational Physics*, 228(15):5370–5389, 2009.

[4] Tariq D. Aslam. A partial differential equation approach to multidimensional extrapolation. *Journal of Computational Physics*, 193(1):349–355, 2004.

[5] Jos Bico, Uwe Thiele, and David Qur. Wetting of textured surfaces. *Colloids and Surfaces A: Physicochemical and Engineering Aspects*, 206(1):41–46, 2002.

[6] James C. Bird, Shreyas Mandre, and Howard A. Stone. Short-time dynamics of partial wetting. *Phys. Rev. Lett.*, 100:234501, Jun 2008.

[7] T.D Blake and J.M Haynes. Kinetics of liquidliquid displacement. *Journal of Colloid and Interface Science*, 30(3):421–423, 1969.

[8] Daniel Bonn, Jens Eggers, Joseph Indekeu, Jacques Meunier, and Etienne Rolley. Wetting and spreading. *Rev. Mod. Phys.*, 81:739–805, May 2009.

[9] J.U Brackbill, D.B Kothe, and C Zemach. A continuum method for modeling surface tension. *Journal of Computational Physics*, 100(2):335–354, 1992.

[10] F. Brochard-Wyart and P.G. de Gennes. Dynamics of partial wetting. *Advances in Colloid and Interface Science*, 39:1–11, 1992.

[11] JOHN W. M. BUSH and ALEXANDER E. HASHA. On the collision of laminar jets: fluid chains and fishbones. *Journal of Fluid Mechanics*, 511:285?310, 2004.

[12] K Cardin, S Wang, O Desjardins, and MM Weislogel. Rebound of large jets from hydrophobic surfaces in low-gravity. in preparation.

[13] A. Carlson, G. Bellani, and G. Amberg. Contact line dissipation in short-time dynamic wetting. *EPL (Europhysics Letters)*, 97(4):44004, 2012.

[14] F. Celestini, R. Kofman, X. Noblin, and M. Pellegrin. Water jet rebounds on hydrophobic surfaces: a first step to jet micro-fluidics. *Soft Matter*, 6(23):5872, 2010.

[15] Lei Chen, Jiapeng Yu, and Hao Wang. Convex nanobending at a moving contact line: The missing mesoscopic link in dynamic wetting. *ACS Nano*, 8(11):11493–11498, 2014. PMID: 25337962.

[16] Yongpan Cheng, Fan Wang, Jinliang Xu, Dong Liu, and Yi Sui. Numerical investigation of droplet spreading and heat transfer on hot substrates. *International Journal of Heat and Mass Transfer*, 121:402–411, 2018.

[17] Robert Chiodi and Olivier Desjardins. A reformulation of the conservative level set reinitialization equation for accurate and robust simulation of complex multiphase flows. *Journal of Computational Physics*, 229(18):6300–6317, 2016.

[18] David L. Chopp. Computing minimal surfaces via level set curvature flow. *Journal of Computational Physics*, 106(1):77–91, 1993.

[19] Jean Comtet, Bavand Keshavarz, and John W. M. Bush. Drop impact and capture on a thin flexible fiber. *Soft Matter*, 12:149–156, 2016.

[20] R. G. Cox. The dynamics of the spreading of liquids on a solid surface. part 1. viscous flow. *Journal of Fluid Mechanics*, 168:169–194, 1986.

[21] R. G. COX. Inertial and viscous effects on dynamic contact angles. *Journal of Fluid Mechanics*, 357:249–278, 1998.

[22] R. V. Craster and O. K. Matar. Dynamics and stability of thin liquid films. *Rev. Mod. Phys.*, 81:1131–1198, Aug 2009.

[23] Anton A. Darhuber and Sandra M. Troian. Principles of microfluidic actuation by modulation of surface stresses. *Annual Review of Fluid Mechanics*, 37(1):425–455, 2005.

[24] Saurish Das, H. V. Patel, E. Milacic, N. G. Deen, and J. A. M. Kuipers. Droplet spreading and capillary imbibition in a porous medium: A coupled ib-vof method based numerical study. *Physics of Fluids*, 30(1):012112, 2018.

[25] R.E. Davis and Andreas Acrivos. The influence of surfactants on the creeping motion of bubbles. *Chemical Engineering Science*, 21(8):681–685, 1966.

[26] Pierre-Gilles de Gennes, Françoise Brochard-Wyart, and David Quéré. *Capillarity and Gravity*, pages 33–67. Springer New York, New York, NY, 2004.

[27] Pierre-Gilles de Gennes, Francoise Brochard-Wyart, David Qur, Axel Reisinger, and Benjamin Widom. Capillarity and wetting phenomena: Drops, bubbles, pearls, waves. 57:66–67, 01 2004.

[28] Robert D. Deegan, Olgica Bakajin, Todd F. Dupont, Greb Huber, Sidney R. Nagel, and Thomas A. Witten. Capillary flow as the cause of ring stains from dried liquid drops. *Nature*, 389:827 EP –, 10 1997.

[29] Olivier Desjardins, Guillaume Blanquart, Guillaume Balarac, and Heinz Pitsch. High order conservative finite difference scheme for variable density low mach number turbulent flows. *Journal of Computational Physics*, 227(15):7125–7159, 2008.

[30] Olivier Desjardins, Jeremy McCaslin, Mark Owkes, and Peter Brady. Direct numerical and large-eddy simulation of primary atomization in complex geometries. *Atomization and Sprays*, 23(11):1001–1048, 2013.

[31] Olivier Desjardins, Vincent Moureau, and Heinz Pitsch. An accurate conservative level set/ghost fluid method for simulating turbulent atomization. *Journal of Computational Physics*, 227(18):8395–8416, 2008.

[32] Hang Ding and Peter D. M. Spelt. Inertial effects in droplet spreading: a comparison between diffuse-interface and level-set simulations. *Journal of Fluid Mechanics*, 576:287–296, 4 2007.

[33] Emilie Dressaire, Alban Sauret, Francois Boulogne, and Howard A. Stone. Drop impact on a flexible fiber. *Soft Matter*, 12:200–208, 2016.

[34] Jean-Baptiste Dupont and Dominique Legendre. Numerical simulation of static and sliding drop with contact angle hysteresis. *Journal of Computational Physics*, 229(7):2453–2478, 2010.

[35] Damien Duvivier, Terence D. Blake, and Jol De Coninck. Toward a predictive theory of wetting dynamics. *Langmuir*, 29(32):10132–10140, 2013. PMID: 23844877.

[36] Ronald P Fedkiw, Tariq Aslam, Barry Merriman, and Stanley Osher. A non-oscillatory eulerian approach to interfaces in multimaterial flows (the ghost fluid method). *Journal of Computational Physics*, 152(2):457–492, 1999.

[37] P. G. De Gennes, X. Hua, and P. Levinson. Dynamics of wetting: local contact angles. *Journal of Fluid Mechanics*, 212:55–63, 1990.

[38] Wensheng He, Jung S. Yi, and Trung Van Nguyen. Two-phase flow model of the cathode of pem fuel cells using interdigitated flow fields. *AIChE Journal*, 46(10):2053–2064, 2000.

[39] C.J. Hotz, R. Mead-Hunter, T. Becker, A.J.C. King, S. Wurster, G. Kasper, and B.J. Mullins. Detachment of droplets from cylinders in flow using an experimental analogue. *Journal of Fluid Mechanics*, 771:327–340, 2015.

[40] S. Tonia Hsieh and George V. Lauder. Running on water: Three-dimensional force generation by basilisk lizards. *Proceedings of the National Academy of Sciences*, 101(48):16784–16788, 2004.

[41] Chun Huh and L.E Scriven. Hydrodynamic model of steady movement of a solid/liquid/fluid contact line. *Journal of Colloid and Interface Science*, 35(1):85–101, 1971.

[42] Young Soo Joung and Cullen R. Buie. Aerosol generation by raindrop impact on soil. *Nature Communications*, 6:6083, 01 2015.

[43] Jie Ju, Hao Bai, Yongmei Zheng, Tianyi Zhao, Ruochen Fang, and Lei Jiang. A multi-structural and multi-functional integrated fog collection system in cactus. *Nature Communications*, 3:1247 EP –, 12 2012.

[44] Kwan Hyoung Kang. How electrostatic fields change contact angle in electrowetting. *Langmuir*, 18(26):10318–10322, 2002.

[45] Soeren Kaps, Rainer Adelung, Michael Scharnberg, Franz Faupel, Srdjan Milenkovic, and Achim Walter Hassel. Determining superhydrophobic surfaces from an expanded cassie baxter equation describing simple wettability experiments. *arXiv preprint arXiv:1408.5273*, 2014.

[46] Ali Kibar. Experimental and numerical investigations of the impingement of an oblique liquid jet onto a superhydrophobic surface: energy transformation. *Fluid Dynamics Research*, 48(1):015501, dec 2015.

[47] Sung-Gil Kim and Wonjung Kim. Drop impact on a fiber. *Physics of Fluids*, 28(4):042001, 2016.

[48] Becky Lavi and Abraham Marmur. The exponential power law: partial wetting kinetics and dynamic contact angles. *Colloids and Surfaces A: Physicochemical and Engineering Aspects*, 250(1):409–414, 2004.

[49] Nolwenn Le Grand, Adrian Daerr, and Laurent Limat. Shape and motion of drops sliding down an inclined plane. *Journal of Fluid Mechanics*, 541:293–315, 2005.

[50] D. Legendre and M. Maglio. Comparison between numerical models for the simulation of moving contact lines. *Computers and Fluids*, 113(Supplement C):2–13, 2015.

[51] Mathieu Lepilliez, Elena Roxana Popescu, Frederic Gibou, and Sbastien Tanguy. On two-phase flow solvers in irregular domains with contact line. *Journal of Computational Physics*, 321:1217–1251, 2016.

[52] Laurent Limat. Drops sliding down an incline at large contact line velocity: What happens on the road towards rolling? *Journal of Fluid Mechanics*, 738:1–4, 2014.

[53] Hao-Ran Liu and Hang Ding. A diffuse-interface immersed-boundary method for two-dimensional simulation of flows with moving contact lines on curved substrates. *Journal of Computational Physics*, 294:484–502, 2015.

[54] Élise Lorenceau, Christophe Clanet, and David Quéré. Capturing drops with a thin fiber. *Journal of Colloid and Interface Science*, 279(1):192–197, 2004.

[55] Michel Y. Louge and Shilpa Sahoo. Model of inertial spreading and imbibition of a liquid drop on a capillary plate. *AIChE Journal*, 63(12):5474–5481, 2017.

[56] Alex V. Lukyanov and Alexei E. Likhtman. Dynamic contact angle at the nanoscale: A unified view. *ACS Nano*, 10(6):6045–6053, 2016. PMID: 27276341.

[57] J. Luo, X.Y. Hu, and N.A. Adams. Curvature boundary condition for a moving contact line. *Journal of Computational Physics*, 310:329–341, 2016.

[58] Marco Maglio and Dominique Legendre. *Numerical Simulation of Sliding Drops on an Inclined Solid Surface*, pages 47–69. Springer International Publishing, Cham, 2014.

[59] Raj M. Manglik, Milind A. Jog, Sandeep K. Gande, and Vishaul Ravi. Damped harmonic system modeling of post-impact drop-spread dynamics on a hydrophobic surface. *Physics of Fluids*, 25(8):082112, 2013.

[60] Emilie Marchandise, Philippe Geuzaine, Nicolas Chevaugeon, and Jean-Franois Remacle. A stabilized finite element method using a discontinuous level set approach for the computation of bubble dynamics. *Journal of Computational Physics*, 225(1):949–974, 2007.

[61] Jeremy O. McCaslin, Émilien Courtine, and Olivier Desjardins. A fast marching approach to multidimensional extrapolation. *Journal of Computational Physics*, 274:393–412, 2014.

[62] M. Meyer, A. Devesa, S. Hickel, X.Y. Hu, and N.A. Adams. A conservative immersed interface method for large-eddy simulation of incompressible flows. *Journal of Computational Physics*, 229(18):6300–6317, 2010.

[63] Rajat Mittal and Gianluca Iaccarino. Immersed boundary methods. *Annual Review of Fluid Mechanics*, 37(1):239–261, 2005.

[64] Masashi Miwa, Akira Nakajima, Akira Fujishima, Kazuhito Hashimoto, and Toshiya Watanabe. Effects of the surface roughness on sliding angles of water droplets on superhydrophobic surfaces. *Langmuir*, 16(13):5754–5760, 2000.

[65] R. Mohammadi, J. Wassink, and A. Amirfazli. Effect of surfactants on wetting of super-hydrophobic surfaces. *Langmuir*, 20(22):9657–9662, 10 2004.

[66] Benjamin J. Mullins, Ryan Mead-Hunter, Renato N. Pitta, Gerhard Kasper, and Wolfgang Heikamp. Comparative performance of philic and phobic oil-mist filters. *AIChE Journal*, 60(8):2976–2984, 2014.

[67] Satoshi Nita, Minh Do-Quang, Jiayu Wang, Yu-Chung Chen, Yuji Suzuki, Gustav Amberg, and Junichiro Shiomi. Electrostatic cloaking of surface structure for dynamic wetting. *Science Advances*, 3(2), 2017.

[68] Elin Olsson, Gunilla Kreiss, and Sara Zahedi. A conservative level set method for two phase flow {II}. *Journal of Computational Physics*, 225(1):785–807, 2007.

[69] Mark Owkes and Olivier Desjardins. A computational framework for conservative, three-dimensional, unsplit, geometric transport with application to the volume-of-fluid (vof) method. *Journal of Computational Physics*, 270:587–612, 2014.

[70] Kyoo-Chul Park, Shreerang S. Chhatre, Siddarth Srinivasan, Robert E. Cohen, and Gareth H. McKinley. Optimal design of permeable fiber network structures for fog harvesting. *Langmuir*, 29(43):13269–13277, 2013. PMID: 23895249.

[71] Andrew R. Parker and Chris R. Lawrence. Water capture by a desert beetle. *Nature*, 414:33 EP –, 11 2001.

[72] Stphane Popinet. An accurate adaptive solver for surface-tension-driven interfacial flows. *Journal of Computational Physics*, 228(16):5838–5866, 2009.

[73] Baburaj A. Puthenveettil, Vijaya K. Senthilkumar, and E. J. Hopfinger. Motion of drops on inclined surfaces in the inertial regime. *Journal of Fluid Mechanics*, 726:26–61, 2013.

[74] Weiqing Ren and Weinan E. Boundary conditions for the moving contact line problem. *Physics of Fluids*, 19(2):022101, 2007.

[75] Y. RENARDY, S. POPINET, L. DUCHEMIN, M. RENARDY, S. ZALESKI, C. JOSSERAND, M. A. DRUMRIGHT-CLARKE, D. RICHARD, C. CLANET, D. QUR, and et al. Pyramidal and toroidal water drops after impact on a solid surface. *Journal of Fluid Mechanics*, 484:69–83, 2003.

[76] Romain Rioboo, Cameron Tropea, and Marco Marengo. Outcomes from a drop impact on solid surfaces. *Atomization and Sprays*, 11(2), 2001.

[77] G. Della Rocca and G. Blanquart. Level set reinitialization at a contact line. *Journal of Computational Physics*, 265(Supplement C):34–49, 2014.

[78] R. P. Sahu, S. Sinha-Ray, A. L. Yarin, and B. Pourdeyhimi. Blowing drops off a filament. *Soft Matter*, 9:6053–6071, 2013.

[79] J. A. Sethian and Peter Smereka. Level set methods for fluid interfaces. *Annual Review of Fluid Mechanics*, 35(1):341–372, 2003.

[80] Jacco H. Snoeijer. Free-surface flows with large slopes: Beyond lubrication theory. *Physics of Fluids*, 18(2):021701, 2006.

[81] Jacco H. Snoeijer and Bruno Andreotti. Moving contact lines: Scales, regimes, and dynamical transitions. *Annual Review of Fluid Mechanics*, 45(1):269–292, 2013.

[82] Zlatko Solomenko, Peter D.M. Spelt, and Pascal Alix. A level-set method for large-scale simulations of three-dimensional flows with moving contact lines. *Journal of Computational Physics*, 348(Supplement C):151–170, 2017.

[83] Peter D.M. Spelt. A level-set approach for simulations of flows with multiple moving contact lines with hysteresis. *Journal of Computational Physics*, 207(2):389–404, 2005.

[84] Y. Sui and Peter D.M. Spelt. An efficient computational model for macroscale simulations of moving contact lines. *Journal of Computational Physics*, 242:37–52, 2013.

[85] Yi Sui, Hang Ding, and Peter D.M. Spelt. Numerical simulations of flows with moving contact lines. *Annual Review of Fluid Mechanics*, 46(1):97–119, 2014.

[86] Š. Šikalo, H.-D. Wilhelm, I. V. Roisman, S. Jakirlić, and C. Tropea. Dynamic contact angle of spreading droplets: Experiments and simulations. *Physics of Fluids*, 17(6):062103, 2005.

[87] TF Tadros. *Role of Surfactants in Wetting, Spreading and Adhesion*, chapter 11, pages 335–397. Wiley-Blackwell, 2005.

[88] L H Tanner. The spreading of silicone oil drops on horizontal surfaces. *Journal of Physics D: Applied Physics*, 12(9):1473, 1979.

[89] Grtar Tryggvason, Ruben Scardovelli, and Stphane Zaleski. *Direct Numerical Simulations of Gas?Liquid Multiphase Flows*. Cambridge University Press, 2011.

[90] J. N. Tsitsiklis. Efficient algorithms for globally optimal trajectories. *IEEE Transactions on Automatic Control*, 40(9):1528–1538, Sep 1995.

[91] David C. Venerus and David Nieto Simavilla. Tears of wine: new insights on an old phenomenon. *Scientific Reports*, 5:16162 EP –, 11 2015.

[92] O. V. Voinov. Hydrodynamics of wetting. *Fluid Dynamics*, 11(5):714–721, Sep 1976.

[93] S Wang, M Louge, and O Desjardins. Sub-grid scale modeling of moving contact lines for mesh-independent two-phase flow simulations. in preparation.

[94] Sheng Wang and Olivier Desjardins. 3D numerical study of large-scale two-phase flows with contact lines and application to drop detachment from a horizontal fiber. *International Journal of Multiphase Flow*, 101:35–46, 2018.

[95] Sheng Wang and Olivier Desjardins. Numerical study of the critical drop size on a thin horizontal fiber: Effect of fiber shape and contact angle. *Chemical Engineering Science*, 187:127–133, 2018.

[96] Koen G. Winkels, Joost H. Weijs, Antonin Eddi, and Jacco H. Snoeijer. Initial spreading of low-viscosity drops on partially wetting surfaces. *Phys. Rev. E*, 85:055301, May 2012.

[97] Yi Xia and Paul H. Steen. Moving contact-line mobility measured. *Journal of Fluid Mechanics*, 841:767–783, 2018.

[98] Shixin Xu and Weiqing Ren. Reinitialization of the level-set function in 3d simulation of moving contact lines. *Communications in Computational Physics*, 20(5):1163–1182, 2016.

[99] A.L. Yarin. Drop impact dynamics: Splashing, spreading, receding, bouncing. *Annual Review of Fluid Mechanics*, 38(1):159–192, 2006.

[100] G D Yarnold and B J Mason. The angle of contact between water and wax. *Proceedings of the Physical Society. Section B*, 62(2):125, 1949.

[101] Kensuke Yokoi, Damien Vadillo, John Hinch, and Ian Hutchings. Numerical studies of the influence of the dynamic contact angle on a droplet impacting on a dry surface. *Physics of Fluids*, 21(7):072102, 2009.

[102] Yuehua Yuan and T. Randall Lee. *Contact Angle and Wetting Properties*, pages 3–34. Springer Berlin Heidelberg, Berlin, Heidelberg, 2013.

[103] Kungang Zhang, Fangjie Liu, Adam J. Williams, Xiaopeng Qu, James J. Feng, and Chuan-Hua Chen. Self-propelled droplet removal from hydrophobic fiber-based coalescers. *Phys. Rev. Lett.*, 115:074502, Aug 2015.

[104] P. Zhang and K. Mohseni. Theoretical model of a finite force at the moving contact line. *ArXiv e-prints*, November 2017.

[105] Benzhong Zhao, Christopher W. MacMinn, and Ruben Juanes. Wettability control on multiphase flow in patterned microfluidics. *Proceedings of the National Academy of Sciences*, 113(37):10251–10256, 2016.

[106] Yang Zhu, Hao-Ran Liu, Kai Mu, Peng Gao, Hang Ding, and Xi-Yun Lu. Dynamics of drop impact onto a solid sphere: spreading and retraction. *Journal of Fluid Mechanics*, 824, 2017.

[107] Alexander Z. Zinchenko and Robert H. Davis. Motion of deformable drops through porous media. *Annual Review of Fluid Mechanics*, 49(1):null, 2017.